Length Scales of Dynamic Heterogeneities of Low and High Molecular Weight Glass Formers from Multidimensional NMR

Dissertation
zur Erlangung des Grades
“Doktor der Naturwissenschaften”

am Fachbereich Chemie und Pharmazie
der Johannes Gutenberg Universität
in Mainz

Stefan A. Reinsberg
geb. in Leipzig

Mainz 2001

Dekan :
Erster Berichterstatter :
Zweiter Berichterstatter :

Tag der mündlichen Prüfung: 4. Februar 2002

Contents

Introduction

One of the most remarkable features of glasses is their dramatic viscous slow down when temperatures are lowered from the melting point, T_{m}, towards the glass-transition temperature, T_{g}. Contrary to the abrupt change from a liquid to a solid by crystallisation, mobility of glass formers expressed by viscosity or relaxation rates decreases continually over a range of up to fifteen orders of magnitude as temperature is reduced. One puzzling observation is that no dramatic structural changes seem to accompany the dynamics, that varies over a vast range. X-ray as well as neutron-scattering studies indicate no more than subtle changes in the structure from above to below the glass transition. What then is the reason for the dramatic slow down? Dynamics in one region of a sample can differ by orders of magnitude from the dynamics of another region in close spatial proximity. Many glass researchers see a link between understanding this heterogeneity and the reason for the precipitous slow down.

In the 1970s, scientists generally believed that a closed theory was within reach and only a few details remained to be solved. Further experiments revealed surprising and previously hidden complexities, such as the existence of a cross-over region at intermediate viscosities, very fast pico-second processes, or ultra-slow mega-second processes. These new issues proved that the glass transition was far from being fully understood which prompted Nobel laureate Phil Anderson to say in the March 1995 issue of *Science*:

> The deepest and most interesting unresolved problem in solid-state theory is probably the theory of the nature of glass and the glass transition. [. . .] The solution of the more important and puzzling glass problem may also have a substantial intellectual spin off. Whether it will help make better glass is questionable.

Other rankings cite the the glass transition amongst the major physical quests remaining unsolved together with broken charges, application of superconductivity, and measurement philosophy in quantum mechanics.

Interested outsiders often find it difficult to relate to the challenge of solving the glass-transition problems. The holy grail of glass research is a theory that describes macro-

scopic observables based solely on information about microscopic properties. Given the multifarious kinds of glasses having a variety of molecular interactions, scientists have given up hope of finding a single decisive idea which leads to a description of the universal glassy behaviour. Theories describing a particular subset of the reality seem to be a more realistic endeavour in the intermediate run. To validate these kind of theories we need a thorough understanding of microscopic and mesoscopic structures and their relationships. Such an understanding would help in revealing general features and in distinguishing between molecular individualities.

A variety of techniques is available with which one can study phenomena associated with the glass transition. In comparison to other well-established methods such as dielectrics, light scattering, and neutron diffraction, nuclear magnetic resonance (NMR) takes an outstanding role in studying such phenomena. This is due to the fact that NMR allows a broad investigation of quantitative and qualitative features of solids; it is hoped that the study of molecular, and other microscopic properties will unveil the relationship between these properties and the macroscopically observed dynamic properties. A number of specialised NMR techniques cover, often in an overlapping manner, an extremely wide range of time scales. Spin-lattice relaxation-time studies measure times as short as 10^{-9} s, lineshape analysis in the range of ms, and multi-dimensional exchange spectroscopy measurements extend up to correlation times of several seconds. Similarly, a wide range of length scales is covered by such techniques as measurements of dipolar coupling constants (Ångstrøms), spin-diffusion measurements (nm. . . μm), and imaging techniques (mm . . . m).

This thesis presents a study of heterogeneities in structural glass formers by means of multi-dimensional nuclear magnetic resonance (NMR). Chapter 1 provides background information regarding the two pivotal points of this thesis: the properties of glass formers together with theoretical interpretation and the fundamentals of NMR as used for the study of dynamics in solids. The substances investigated in this work, glycerol and *o*-terphenyl are described in Chapter 2. Two salient features of the heterogeneous dynamics above T_{g}, the lifetime and spatial extent of dynamic heterogeneities, are the central focus of the present work. In Chapter 3, computer experiments of different jump models aim to qualitatively reproduce the behaviour of previously observed four-time correlation functions in a polymeric glass former, PVAc. Results from these simulations are used to establish a picture of the geometry of motion in PVAc. The length scale of slow-mobility domains is investigated using an advanced four-dimensional spin-diffusion experiment. The theory and simulation of this experiment are presented in Chapter 4. A method for data analysis is derived and thoroughly tested. Chapter 5 presents the first direct length-scale measurements of two low molecular weight glass formers, viz. glycerol and *o*-terphenyl. The dependence of the length scale on the size of the selected subensemble

and on temperature is discussed. Theories predicting length scales are tested against the measured results.

Chapter 1

Fundamentals

Our surroundings are dominated by disordered solids. This is contrary to the impression one gets from introductory text books of physical chemistry or solid-state physics. Many convenient assumptions true for crystals (e.g. periodicity) do not hold for amorphous solids, a fact which renders research of this state of matter and its associated phenomena rather difficult.

The first part of this chapter will touch upon the phenomenology and theoretical description of the class of amorphous substances that has attracted most interest during the past decades: supercooled liquids and glasses. In the second part, experimental methods used for the investigation of dynamical properties of solids, in particular nuclear magnetic resonance (NMR) will be reviewed.

1.1 Supercooled Liquids and Glasses

If a liquid is cooled to below its melting point, T_{m}, without crystallisation it is said to be supercooled. Upon further cooling the supercooled liquid exhibits a dramatic increase in viscosity (by up to 15 orders of magnitude) until it reaches the glass-transition temperature, T_{g}. Below T_{g} relaxation in the system is said to be frozen in.

While most practical knowledge needed for glass or plastic technologies and applications is now available, research into this phenomenon has still intensified over the past decade. The physical quest of glass transition not only poses an intellectual challenge, but is also of practical importance in a variety of fields: Interesting fragile glass formers are amorphous synthetic polymers. Anomalously fast diffusion of solvents, antioxidants, and plasticiser [Cicerone et al., 1995a], as well as rheological properties [Plazek, 1965] might be explainable using knowledge gained from studies on model glass formers. The controlling of crystallisation is of importance to many applications: the glass industry (a clear optical glass requires the absence of even small crystallites), the pharmaceutical

industry (how long is a drug prepared in the supercooled state stable - does it crystallise during storage?), the production of ceramics and enamels needs a manageable interplay of glass and phase transition, enzyme and tissue preservation (will the biological structure remain intact after the removal of water from a saccharide solution [Fox, 1995]), and food science (prediction of the stability of low-moisture carbohydrate media [Champion et al., 1997]).

1.1.1 Phenomenology - Prominent Features of Supercooled Liquids

Let us now briefly recapitulate some of the remarkable aspects of the phenomenology of the glass transition.

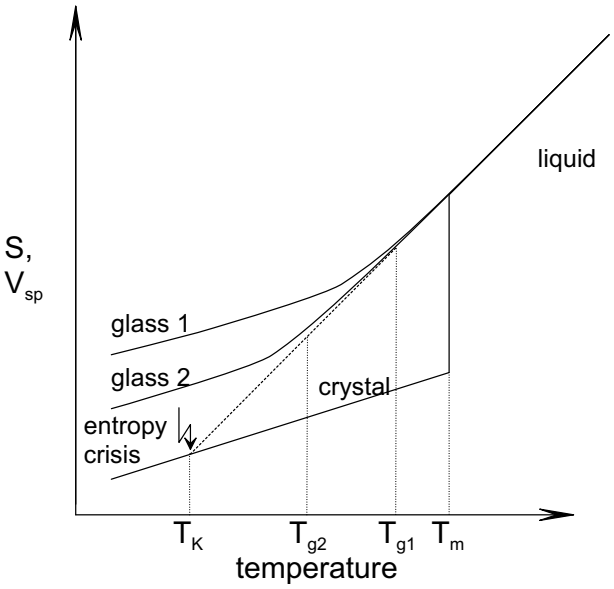

Figure 1.1: Schematic plot of the specific volume (entropy) as a function of temperature for a liquid which can crystallise (sudden drop at T_{m}) or form a glass.

Fig. 1.1 shows how the specific volume (or entropy) depends, in general, on temperature upon cooling towards T_{g} and below. Note that some glass formers will – under certain conditions – crystallise. This first-order phase transition occurs at the melting point, T_{m}, in Fig. 1.1. If the system manages to avoid crystallisation it will eventually perform a glass transition which occurs over a range of several Kelvin. This transition, however, is not a phase transition. Frequently, the entropy crisis is discussed in connection with the thermodynamics of a supercooled liquid approaching T_{g}. If we were to assume we could continuously supercool a liquid (by, e.g., a very low cooling rate), the entropy, S, of the glass former would eventually drop below the entropy of the crystal (note the different slopes of S for the liquid and the crystal). While reaching the point where both entropies coincide (also called Kauzmann temperature, T_{K}) is not in contradiction to any thermodynamic laws, any further decrease in the liquid entropy would violate the third law of thermodynamics (entropy would become 0 above $T = 0$ and eventually become negative!). Hence, the Kauzmann temperature, T_{K}, is a rough though not very strict lower bound for T_{g}.

One way to define the glass-transition temperature, T_{g}, is to evaluate the temperature dependence of the specific heat. It can be directly derived from the entropy (assuming

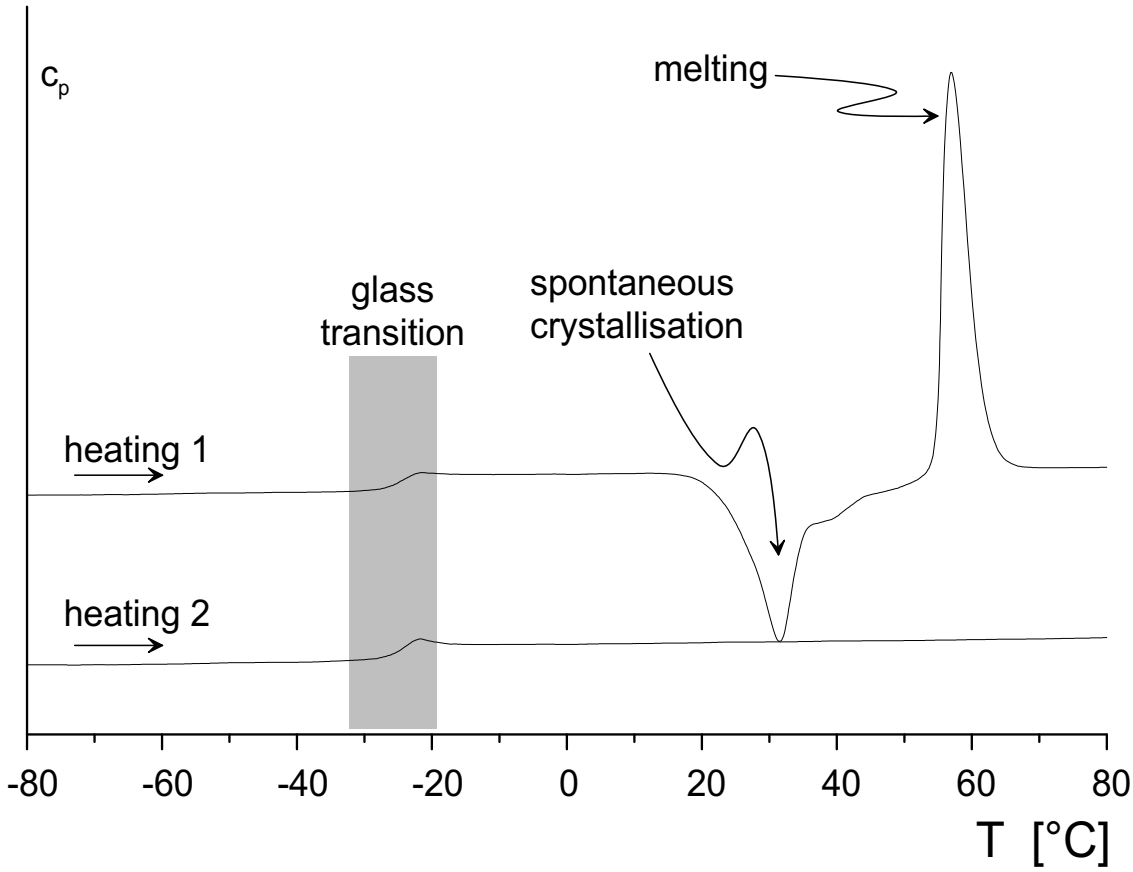

Figure 1.2: Specific heat from two successive DSC measurements on the low molecular weight glass former OTP with identical cooling rates. In the first run (upper curve), spontaneous crystallisation occured below T_{m} but above T_{g}. In a second run, the OTP sample did not crystallise.

negligible mechanical work): $c_{\mathrm{p}} = \partial S/\partial T$. In Fig. 1.2, two successive differential-scanning-calorimetry scans show how the sample first spontaneously crystallised (please note this happened below T_{m}) and, in a second run, avoids this phase transition. The plot in Fig. 1.2 already reveals the difficulty in pinning T_{g} down to one definite temperature. Not only does the glass transition occur over a range of temperatures, but also the position of that range depends on the cooling rate. Despite these difficulties, T_{g} can be extrapolated to infinitely slow cooling and therefore provides a very useful parameter for characterising (mechanic) properties of particularly polymeric samples.

As mentioned above, the viscosity of liquids below their melting point increases dramatically. This is displayed in Fig. 1.3. The viscosity of the likely best known glass former SiO_2 shows a nearly Arrhenius-like temperature dependence. From a terminology introduced by Angell [1984] we call such glass formers *strong*. Glycerol and even more

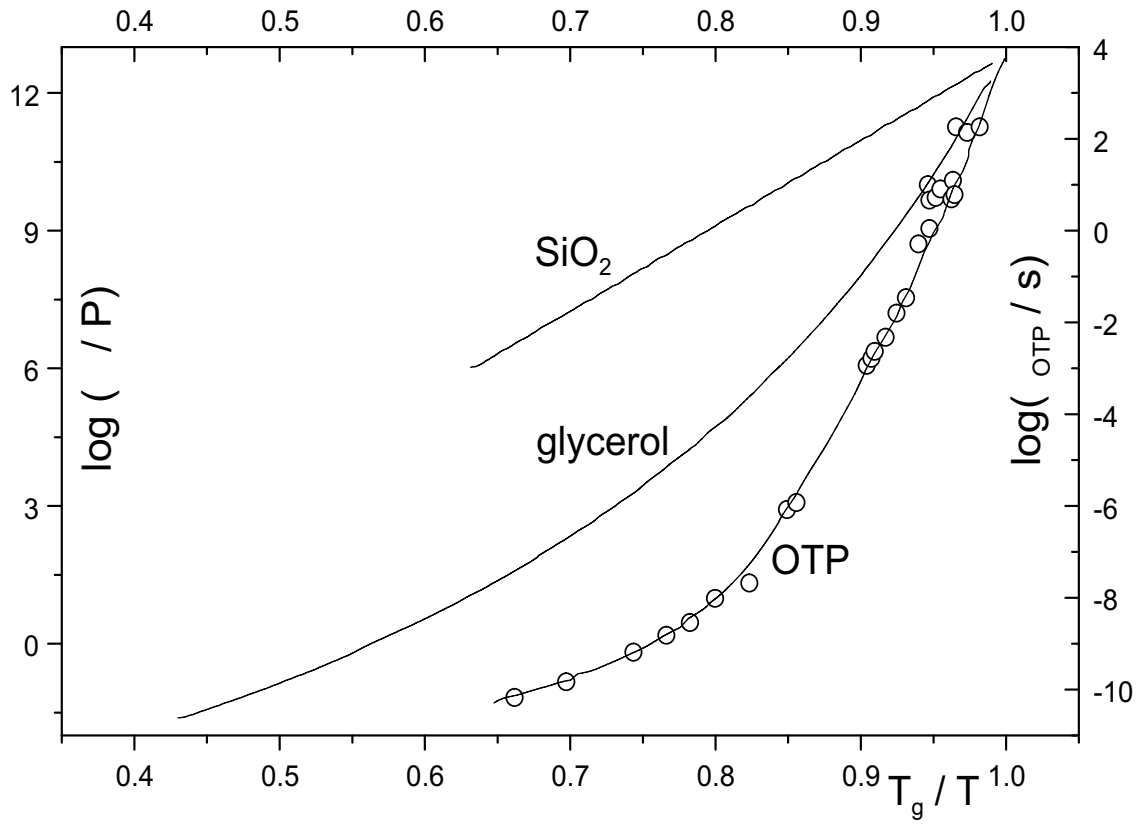

Figure 1.3: Viscosity, η, as a function of reduced inverse temperature for three liquids: SiO_2, glycerol, and *o*-terphenyl. Reorientation times are shown for OTP on the right (open circles). Data from Ediger [1996]

so *o*-terphenyl(OTP) exhibit a strongly non-Arrhenius temperature dependence of their viscosity when approaching T_g. These glasses are called *fragile*. Measures of molecular mobility other than viscosity, e.g. molecular rotation pertaining to the α-relaxation, as displayed for OTP, show an identical dependence on reduced temperature, T_g/T. While the present work exclusively deals with the slowest relaxation process[1], this is by no means the only relaxation mechanism in glasses. β relaxation, often but not exclusively associated with localised motion of the sidechain, exhibits an Arrhenius-like temperature dependence. This process, also termed the β_{slow} process, first discussed by Johari and Goldstein [1970], is not to be confused with a fast β process introduced by Leutheusser [1984] and Bengtzelius et al. [1984] in the framework of mode-coupling theory (MCT).

[1] by definition the α relaxation

Measures of molecular mobility (viscosity, relaxation rates) can be described by the Vogel-Fulcher-Tammann equation (VFT):

$$\ln \frac{\tau}{\tau_0} = \frac{B}{T - T_\infty} \tag{1.1}$$

Another equation regularly used to fit T-dependent molecular mobility (originally viscosity data) is the Williams-Landel-Ferry (WLF) description

$$\lg \frac{\tau}{\tau_0} = -\frac{C_1(T - T_0)}{C_2 + (T - T_0)}. \tag{1.2}$$

In a temperature range above T_g, the parameters of VFT and WLF equations are related to each other by $C_2 = T_0 - T_\infty$ and $C_1 = \frac{B}{C_2} \lg \mathbf{e}$. Fragility, m, can be characterised by a 'steepness index' at $T = T_\mathrm{g}$ [Böhmer et al., 1993]:

$$m(T_\mathrm{g}) = -\frac{\mathrm{d} \lg \eta}{\mathrm{d} \ln T}\bigg|_{T=T_\mathrm{g}} \tag{1.3}$$

The apparent activation energy ($= k_\mathrm{B} \mathrm{d}(\ln \tau)/\mathrm{d}(1/T)$) of fragile liquids such as OTP may reach 500 kJ/mol or more near T_g. Certainly this activation energy can not be associated with the motion of a *single* molecule because energies of that size surpass the strength of chemical bonds in organic compounds. Instead, a number of molecules are thought to *cooperatively* move which, of course, requires higher energies.

A striking feature of supercooled liquids is their nonexponential response to various perturbations. This nonexponential response is phenomenologically described by the Kohlrausch-Williams-Watts (KWW) function:

$$F(t) = \mathbf{e}^{-(t/\tau)^\beta} \tag{1.4}$$

This function was originally used by Kohlrausch in 1854 to fit the electric polarisation decay of Leiden jars. In 1970, this function was rediscovered by Williams and Watts [Campbell et al., 1998]. Note that $\beta = 1$ recovers the single-exponential case of relaxation whereas $\beta < 1$ gives the well known stretched exponentials. Even small changes in β correspond to large differences in the width of distribution of relaxation times.

1.1.2 Heterogeneity vs. Homogeneity

The existence of nonexponential relaxation prompts the question of what microscopic processes underlie this macroscopically observed behaviour. The two extreme scenarios

are a homogeneous picture where microscopic relaxators relax intrinsically nonexponentially, and a heterogeneous picture where exponentially relaxing subunits relax with relaxation rates distributed over a range such that the macroscopic response will appear as stretched exponential.

Numerous investigations have shown the dominance of the heterogeneous behaviour in α relaxation [Li et al., 1989; Schnauss et al., 1990; Schmidt-Rohr and Spiess, 1991; Cicerone and Ediger, 1995; Heuer et al., 1996; Böhmer et al., 1996; Richert, 1997]. Despite the overwhelming evidence for the predominantly heterogeneous character of relaxation, there are views to the contrary: In a nonresonant spectral hole-burning (NSHB) experiment by Schiener et al. [1996] the authors observed in slow dielectric response, for the first time, dynamic heterogeneities, which had previously been shown in NMR. Cugliandolo and Iguain [2000] claimed to have constructed an infinite-range model that reproduced the results of the NSHB experiment but was devoid of both spatial structure and spatial heterogeneity. As is now generally accepted [Chamberlin and Richert, 2001; Diezemann and Böhmer, 2001], the NSHB experiment can not establish spatial heterogeneity but can merely deduce dynamic heterogeneity based on frequency selection. A literature review by Ediger [2000a] discusses more evidence for spatially heterogeneous dynamics.

If one accepts the view of dynamic heterogeneity, then one must also question how long these heterogeneities persist, a concept referred to as their *lifetime*. Already the first NMR experiments by Schmidt-Rohr and Spiess [1991] that were designed to detect heterogeneity as the source for nonexponential relaxation were also able to estimate the lifetime of slow domains. While the system (PVAc at $T = T_{\mathrm{g}} + 20$ K) was non-ergodic on the time scale of the α-relaxation, τ_0, it became ergodic for times longer than $50\tau_0$. Further experiments [Heuer et al., 1995; Böhmer et al., 1996; Schiener et al., 1996; Russell et al., 1998] using such techniques as ^{13}C NMR, ^{2}H NMR, and NSHB corroborated the notion of heterogeneity. One outstanding issue is reconciling the largely differing lifetimes deduced from an optical dynamic hole-burning experiment[2] by Cicerone and

[2]Note that the reduced 4D NMR experiment by Schmidt-Rohr and Spiess [1991] can be viewed as a dynamic filter as well as a hole-burning experiment: the dynamics of a slow subensemble of the sample is

Ediger [1995] compared to results using other techniques (e.g. NMR [Böhmer et al., 1996; Hinze et al., 1998] and dielectric hole burning [Schiener et al., 1996]). One explanation offered by Ediger [2000b] is a strong temperature dependence of the exchange times-α-relaxation times ratios, $\tau_{\text{ex}}/\tau_\alpha$, starting shortly above T_g. That way lifetimes of ca. $1000\tau_\alpha$ (optical hole-burning) at 1 K above T_g and lifetimes on the order of τ_α (NMR) at $T > T_\text{g} + 10$ K can be explained. Discounting the photo-bleaching results solely by virtue of their being a probe-specific artefacts seems not justifiable because studies have proved the close correspondence of probe and molecule rotation [Cicerone and Ediger, 1993]. Further studies by Wang and Ediger [2000] have shown similarly long lifetimes in polystyrene with two different probes.

Dynamic hole burning is only one approach for the selection of subensembles. In a recent experiment, Russell et al. [1998] noticed a change over time in the resonance frequency of a cantilever holding an atomic microscope tip above the surface of a PVAc film. This was interpreted as a fluctuation of the dielectric properties of a nanoregion in the sample. The persistence of the thus detected heterogeneities was about twice τ_α at 1 K above T_g. Also related to the measurements of dynamics on a microscopic level are attempts to measure single-molecule properties such as performed by Ha et al. [1999] and Bartko and Dickson [1999].

In summary, an arsenal of experimental techniques exists that can prove heterogeneous dynamics in supercooled liquids. However, no technique has yet been able to provide uncontested heterogeneity-lifetime data representative of a number of glass-forming liquids and valid over a wide range of temperatures. Since the lifetime of heterogeneities is of critical importance for our understanding of heterogeneous dynamics, it is worth developing a better understanding of the results from existing experimental techniques. In this light, Chapter 3 is devoted to computer simulations of rate-exchange NMR experiments.

selectively observed.

1.1.3 Length Scale of Dynamic Heterogeneities

While the *lifetime* of heterogeneities is an important aspect, the *spatial extent* of regions with a more or less constant jump rates within is likewise a question whose answer is of importance to theories describing the glass transition. For decades, theories of the glass transition have invoked various diverging length scales to explain the apparently diverging time scales for relaxation at low temperatures. No *static* length scales have been identified [Leheny et al., 1996]. A *dynamic* length scale, however, is central to many theories. This dynamic length scale is often associated with cooperatively rearranging regions (CRR's), first postulated by Adam and Gibbs [1965].

Fig. 1.4 shows a sketch of spatially heterogeneous regions. They consist of a number of molecules exhibiting similar relaxation properties. As the lifetime of the heterogeneity is finite, one imagines these regions might build, vanish, or translate in a random fashion. The length ξ_{het} indicated in the figure is what we call the heterogeneity length scale.

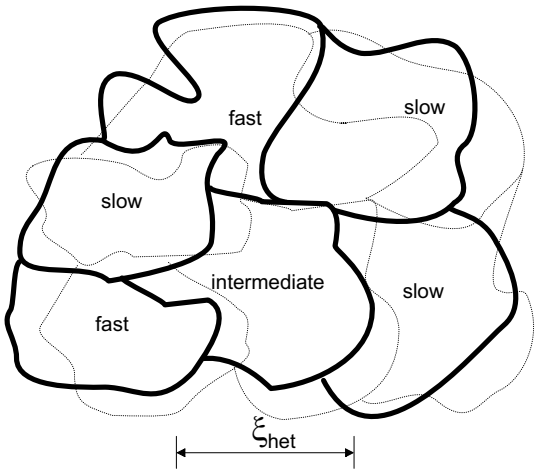

Figure 1.4: Sketch[3] of spatial distribution of dynamic heterogeneities and their evolution over time (dashed lines).

A remarkable amount of experimental work has been devoted to measuring this length scale. So far, most techniques measure the length scale indirectly by invoking assumptions or by introducing external perturbations. They shall be briefly summarised below. In a study by Cicerone et al. [1995b] six probe molecules of different size were used to measure time-resolved optical spectroscopy in *o*-terphenyl. An increased probe size resulted in a decrease in the relaxation-time dispersion parameter, β. The extrapolation of this trend to $\beta = 1$ yielded 2.5 nm for the length scale at which OTP becomes homogeneous at T_{g}. Results from this study were used to rule out a number of proposed models of cooperativity. The ex-

[3]Please note that this is only a *sketch*: Some theories propose a more detailed picture, e.g. 'islands of mobility' in a matrix of solids. This issue is discussed in more detail in Section 5.3

istence of 'rigid clusters'[4] is questionable because rotation relaxation behaviour of probe molecules shows that they are not entrained in these cluster. 'Locally liquid-like domains' are incompatible with differing relaxation times and dispersion parameters observed for the different probes.

Another method that utilises an external perturbation to monitor cooperativity is the confinement of a glass former in pores. Kremer et al. [1999] used broad-band dielectric spectroscopy to investigate several low molecular weight glass formers (e.g. salol, glycerol, ethylene glycol) confined to pores of zeolites and nanoporous glasses. The variation in size and topology of the confining geometry allows the onset of bulk-like dynamics in a trapped supercooled liquid to be monitored. Criticism of this method is directed at the conceivably strong perturbation by surface interaction (this is why, for example, surface treatment by coating has to be applied for porous soda glasses). The effect of an interfacial layer has to be accounted for in order to arrive at a cooperativity length scale of 0.7 nm. In a different study Barut et al. [1998] investigated dielectrics of confined liquids in two (pores) and three (droplets) dimensions. This study, too, corroborates the existence of an interfacial layer and the onset, independent of the dimension, of cooperativity under increased confinement size.

A different form of confinement was chosen by Keddie et al. [1994] who measured glass-transition temperatures for polystyrene films of various thicknesses. The decrease of T_{g} with reduced film thickness was not due to polymer-chain confinement as supported by the weak dependence of the T_{g} decrease on molecular weight. Rather, invoking a liquid-like surface layer whose thickness diverges when approaching T_{g} allowed estimates of the cooperativity length scale.

Rizos and Ngai [1999] investigated molecular reorientation-relaxation dynamics of Acrolor (a mixture of polychlorinated biphenyls) using photon correlation spectroscopy and dielectric relaxation. By varying the addition of low and high molecular weight polyisoprene and polybutadiene they were able to control the radius of gyration, R_{g}, of the polymer chain. The change of the distribution parameter β with temperature, $\mathrm{d}\beta/\mathrm{d}T$, showed a marked decrease at $R_{\mathrm{g}} = 15$ Å which is Rizo's and Ngai's estimate of the length scale of cooperativity.

[4] A size estimate of Fujara et al. [1992] suggest 5.6 nm at T_{g}.

One is, obviously, inclined to hope for insights into spatial heterogeneity from scattering techniques such as inelastic neutron scattering or low-frequency Raman spectroscopy. Indeed, a so-called boson peak is found for both techniques [Frick and Richter, 1995; Sokolov et al., 1992] and is thought to stem from the phonon spectrum of nanometre-sized regions. However, a number of alternative explanations have been proposed [Buchenau et al., 1992; Schirmacher et al., 1998; Franosch et al., 1997] making the origin of the boson peak a matter of controversial discussion.

In an adaptation of the Adam-Gibbs model by Donth [1982], standard relations of statistical thermodynamics about mean-square fluctuations of density, temperature, entropy, or energy are restricted to the slow degrees of freedom of the independent distinguishable subsystems (termed V_α and equivalent to CRR's). Thermodynamic fluctuation formulas can then be used to estimate the volume of the independent entities V_α and, hence, the *characteristic* length $\xi_\alpha = V_\alpha^{1/3}$. It is unclear how justified the calculation of ξ_α is considering the implicit assumption about a more or less compact shape of the CRR's. In any case, experimental data from heat-capacity spectroscopy [Korus et al., 1997] and temperature-modulated differential scanning calorimetry allowed the determination of *characteristic* lengths in the nanometre range for a wide assortment of glass formers [Hempel et al., 2000]. In addition, temperature-dependent measurements show that the size of cooperativity increases with decreased temperature.

By measuring the heat capacities of glassy and liquid toluene and ethylbenzene Yamamuro et al. [1998] determined the configurational entropies as a function of temperature. For each of the systems examined, the size of CRR increased with decreasing temperature and was frozen-in at four to eight molecules per region at the glass-transition temperature.

In a recent review, Sillescu [1999] compares various theoretical concepts along with experimental evidence for heterogeneity in glass-forming liquids. To date no theory has been presented that captures all the salient features of the viscous slowdown and the glass transition.

The earliest theories approached the problem by postulating phase transitions at T_K. Since the dynamics already are extremely slow at $T \gtrapprox T_\mathrm{K}$, any diverging fluctuation is not observable. A theory by Adam and Gibbs [1965] was built upon the suggestion by

Eyring [1936] that large apparent activation energies are caused by cooperative molecular motion. In the Adam-Gibbs theory, *cooperatively rearranging regions* were defined as 'subsystems which can rearrange into another configuration independently of their environment'. This theory even allows the prediction of the temperature dependence of relaxation times $\tau = \tau_0 \exp\left(\frac{C}{TS_c}\right)$ provided one assumes the configurational entropy, S_c, goes to zero at finite temperatures. One recovers the VFT equation (Eq. 1.1) if $S_c = a(T - T_K)/T$. From the outset, the size of the CRR is predicted to increase for decreasing temperatures according to

$$\xi \propto (T - T_K)^{-1/3} \quad . \tag{1.5}$$

In contrast to developing inhomogeneities from a liquid, the 'inherent structure' formalism proposed by Stillinger [1988] explores the structural aspects of amorphous solids. Local particle groupings fit together in a near-optimal form. Due to contradicting geometrical demands in neighbouring regions, the groupings cannot spread across the entire sample (as for a crystal). In this context, Kivelson et al. [1994] considered 'frustration-limited domains' that form as a liquid is cooled down. The onset of cooperativity happened at a temperature, T^*, above the melting point. Cooperativity increased slowly as the liquid cooled further towards T_g. The more fragile a system is the bigger the domains were predicted to be (on the order of 10^3 molecules) at T_g [Viot et al., 2000].

The observation that the experimental temperature dependence of relaxation times is better described by a dynamic scaling form rather than the classical Vogel form[5] lead Colby [2000] to propose the description of the glass formation to be based on a mean-field limit of a phase transition. Thus, Colby arrived at a relationship between the size of CRR's and relaxation time in the form of $\tau \propto \xi_{het}^z$. The exponent was determined to be $z = 6$ from experimental data in the absence of a theoretical derivation of its value. Recent work by Erwin and Colby [2001] established a near proportionality between fragility index and size of cooperatively rearranging unit. Yamamoto and Onuki [1998] also found scaling behaviour but a different exponent for supercooled liquids with soft-core potentials in two ($z = 4$) and three ($z = 2$) dimensions.

[5]For a different view supported by dielectric retardation consult Richert [2000].

1.2 NMR Spectroscopy

When atomic nuclei are placed in a constant magnetic field of high intensity and are subjected at the same time to a radio-frequency alternating field, a transfer of energy takes place between the high-frequency field and the nucleus. This phenomenon is known as nuclear magnetic resonance (NMR).

A number of excellent textbooks and reviews have dealt with many of the aspects of NMR [Abragam, 1961; Slichter, 1990; Mehring, 1983; McBrierty and Packer, 1993; Stejskal and Memory, 1994; Schmidt-Rohr and Spiess, 1994]. The Encyclopedia of NMR by Grant and Harris [1996] gives a historical overview, and an insightful treatment of nearly every facet of NMR. A new forthcoming volume is an update on the latest developments in the field.

NMR now has multifarious applications and has become a routine analysis tool in many fields: Structure elucidation by means of high-resolution, liquid-state NMR, and magnetic resonance imaging (MRI) in medical research are two prominent examples. However, solid-state NMR is still far from being a routine investigative method. This is likely due to the virtually unlimited breadth of information that solid-state NMR is capable of providing: structure on a scale from Å to mm, or dynamics on a time scale from $10^{-10} \ldots 10$ s can be probed by an arsenal of various tools. Slow dynamic phenomena, and their time and length scale are of central importance to this thesis and are hence dealt with separately in Section 1.3. Below we will summarise some basic features of NMR.

1.2.1 Quantum Mechanical Description

The Hamiltonian, $\mathscr{H}$, relevant for NMR experiments can be written as:

$$\begin{aligned} \mathscr{H} &= \mathscr{H}_{\text{external}} + \mathscr{H}_{\text{internal}} \\ \mathscr{H} &= (\mathscr{H}_{\text{Z}} + \mathscr{H}_{\text{rf}}) + (\mathscr{H}_{\text{Q}} + \mathscr{H}_{\text{CSA}} + \mathscr{H}_{\text{D}} + \mathscr{H}_{\text{J}}) \end{aligned} \tag{1.6}$$

The first two terms in Eq. 1.6 are external factors, namely:

$\mathscr{H}_{\text{Z}}$ Zeeman interaction, representing the interaction of the nuclear spin with the externally applied static magnetic field, and

$\mathscr{H}_{\mathrm{rf}}$ radio frequency interaction, representing the interaction with time-dependent rf fields ($\mathbf{B_1}(t)$ being the magnetic-field component by common terminology).

These terms, although vital to the NMR experiment, are of marginal direct interest. More important are the remaining internal terms that represent

$\mathscr{H}_{\mathrm{Q}}$ the interaction with the quadrupolar moment for nuclei with $I > \frac{1}{2}$,

$\mathscr{H}_{\mathrm{CSA}}$ the interaction between the nuclear spin and its electronic environment (chemical shift anisotropy),

$\mathscr{H}_{\mathrm{D}}$ the interaction among magnetic moments of neighbouring nuclei (dipolar coupling), and

$\mathscr{H}_{\mathrm{J}}$ the indirect coupling of neighbouring nuclei.

The interaction of the magnetic moment, $\boldsymbol{\mu} = \gamma\mathbf{I}$, with the external field, $\mathbf{B_0}$, is described in quantum theory by:

$$\mathscr{H}_{\mathrm{Z}} = -\boldsymbol{\mu} \cdot \mathbf{B_0} = -\gamma\hbar\mathbf{B_0} \cdot \mathbf{I}, \tag{1.7}$$

where γ is the magnetogyric ratio characteristic for a given isotope. $\mathbf{I}$ is the quantum mechanical operator of the angular momentum. The solution of the above Hamiltonian gives the following expression for the energy levels

$$E_{\mathrm{m}} = -\gamma\hbar m B_0 \quad \text{with quantum number} \quad m = -I, -I+1, \ldots, I-1, I. \tag{1.8}$$

with the Larmor frequency being $\omega_{\mathrm{Larmor}} = \gamma B_0$.

For a spin with $I = \frac{1}{2}$, we find a two-level system giving rise to a situation depicted in Fig. 1.5. Spins align parallel and anti-parallel to the direction of the external field, B_0. In a semi-classical picture, spins are said to precess around the static magnetic field. At ambient temperatures the state distribution is slightly biased towards the 'up' spin state, giving rise to a net magnetisation, $\mathbf{M_0}$. The Boltzmann distribution of the two available energy states is given as

$$N_{-\frac{1}{2}} = N_{+\frac{1}{2}} \exp(-\frac{\hbar\omega_{\mathrm{Larmor}}}{k_{\mathrm{B}}T}). \tag{1.9}$$

In the high-temperature approximation $\hbar\omega_{\text{Larmor}} \ll k_{\text{B}}T$, the excess number of spins that are aligned parallel to the magnetic field, $\Delta N = N_{+\frac{1}{2}} - N_{-\frac{1}{2}}$, can be derived from the truncated Taylor series of Eq. 1.9. Its dependence on temperature and external field is the Curie law of paramagnetism

$$\begin{aligned} M_0 =& \Delta N \mu_z \approx N_{+\frac{1}{2}} \frac{\hbar\omega_{\text{Larmor}}}{k_{\text{B}}T} \frac{\hbar\gamma}{2} \approx N\gamma^2\hbar^2 B_0/4k_{\text{B}}T \\ \approx& C B_0/k_{\text{B}}T. \end{aligned} \tag{1.10}$$

Eq. 1.10 shows that the magnetisation will be stronger at higher fields (B_0), lower temperatures (T), and for greater amounts of sample (N). Since the signal is proportional to magnetisation, it will show the same dependence on B_0, T, and N.

In NMR experiments, properties of the spin system are investigated by the application of rf fields. As previously mentioned, the exact quantum mechanical treatment of interaction of the sample with applied rf fields is rarely done. Two alternative routes for dealing with 'hard' pulses are commonly used: Firstly, the product-operator formalism allows a comparatively elegant description of the spin-state evolution and the effect of pulses [Hore et al., 2000]. Secondly, a vector model allows the most intuitive, although not always applicable, description.

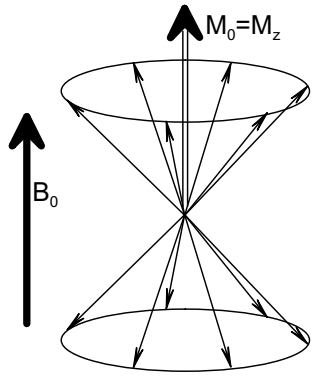

Figure 1.5: Equilibrium magnetisation.

In the vector model, the rf field can be viewed as an oscillating magnetic field $\mathbf{B_1}$ that, alternatively, can be decomposed into two counter-rotating magnetic fields $\mathbf{B_{1+}}$ and $\mathbf{B_{1-}}$ (see Fig. 1.6). The static external magnetic field causes the spins to precess about the direction of $\mathbf{B_0}$. If the frequency of $\mathbf{B_1}$ is chosen to be close to the precession frequency $\omega_{\text{Larmor}} = \gamma B_0$, the rotating field $\mathbf{B_{1+}}$ will be near static with respect to the precessing spins. Since the other magnetic field $\mathbf{B_{1-}}$ is off resonance by $\approx 2\omega_{\text{Larmor}}$, it can be neglected as its interaction with the spin system is weak.

In a rotating frame of reference the precessing spins as well as one component of the magnetic field of the rf pulse, $\mathbf{B_{1+}}$, will appear static. Spins will start to (additionally) precess about the $\mathbf{B_1}$ field for the duration of the pulse. A pulse causing rotation by 90°

(180°) is correspondingly called $\frac{\pi}{2}$ pulse (π pulse). Fig. 1.7a shows how an rf pulse can be considered to be a static albeit time-dependent magnetic field in the rotating frame. Fig. 1.7b visualises the effect of a 90° pulse on magnetisation that is initially aligned parallel to the z axis.

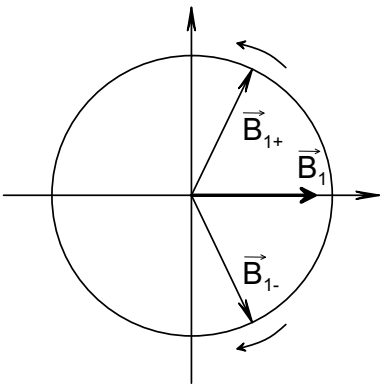

Figure 1.6: RF field decomposed into two counter-rotating magnetic fields.

Based on a Hamiltonian tailored to a certain situation, one can often predict the form of a spectrum. If this is not possible or one is interested in the exact time evolution, one has to apply the Schrödinger equation, $\mathscr{H}|\psi\rangle = i\hbar\partial|\psi\rangle/\partial t$. In NMR, one faces the problem that instead of one wave function $|\psi\rangle$ there is a whole ensemble of spins. This ensemble average can be conveniently described using the density matrix, ρ. It can be defined element by element as a probability-weighted product of the respective coefficients of the wave function, c_{m}.[6]

$$\rho_{\mathrm{nm}} = (|\psi\rangle\langle\psi|)_{\mathrm{nm}} = \overline{c_{\mathrm{m}}^* c_{\mathrm{n}}} \tag{1.11}$$

Using the Schrödinger equation for the ensemble average as given in Eq. 1.11, one arrives at the Liouville-von Neumann equation

$$\frac{\mathrm{d}\rho}{\mathrm{d}t} = \frac{i}{\hbar}(\rho\mathscr{H} - \mathscr{H}\rho) = \frac{i}{\hbar}[\rho, \mathscr{H}] \tag{1.12}$$

[6]For an introduction see Reinsberg [2000].

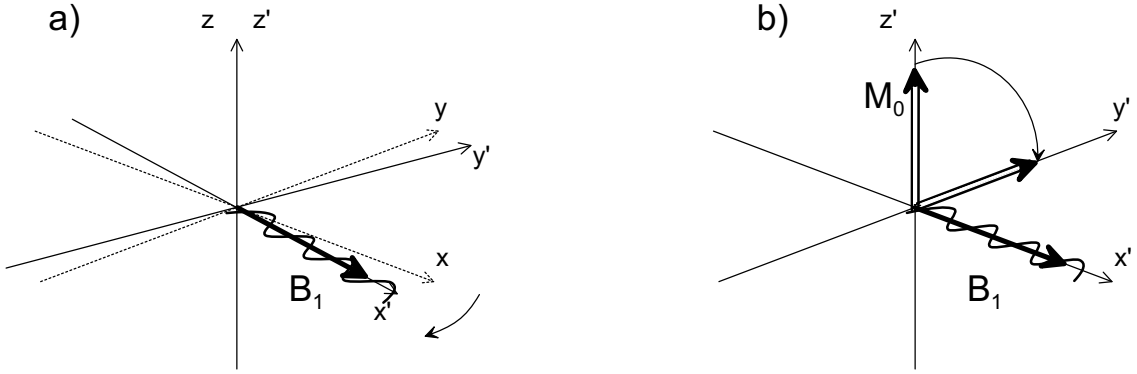

Figure 1.7: Principle of an rf pulse: a) $\mathbf{B_1}$ field is static in a rotating frame, b) a $(\frac{\pi}{2})_x$ pulse flips the magnetisation from z to y according to the left-hand convention.

Provided the starting condition for the density matrix and the explicit shape of the governing Hamiltonian are known, one can, in principle, calculate $\rho(t)$ numerically or, in simple cases, analytically. Usually, the abbreviated equilibrium density matrix is taken as starting condition, e.g. $\rho_0 = \sigma_z$ for a one-spin system, or $\rho_0 = \sigma_z \otimes \mathbf{1} + \mathbf{1} \otimes \sigma_z$ for a two-spin system.

Before we turn to a specific discussion of some of the interaction Hamiltonians mentioned above, some of the generalities associated with all internal Hamiltonian contributions should be considered. A description of Hamiltonians always involves tensor quantities – a property that links two, generally non-parallel vectors. It proves helpful to decompose a tensor into a symmetric and an antisymmetric part, $\sigma = \sigma_{\text{sym}} + \sigma_{\text{asym}}$. Sometimes, an isotropic contribution is separated off yielding a traceless symmetric and a traceless antisymmetric part: $\sigma = \sigma_{\text{iso}} + \sigma_{\text{sym}}^{\text{traceless}} + \sigma_{\text{asym}}^{\text{traceless}}$. The antisymmetric contribution to NMR spectra is usually ignored and the remaining symmetric part can be diagonalised ($\sigma_{\text{sym}} = \sigma_{\text{sym}}^T$) in a frame of reference referred to as principal axis system (PAS). Instead of the three eigenvalues of the diagonal symmetric tensor

$$\sigma = \begin{pmatrix} R_{xx} & 0 & 0 \\ 0 & R_{yy} & 0 \\ 0 & 0 & R_{zz} \end{pmatrix}, \tag{1.13}$$

frequently three other values are reported:

The *isotropic average,* $R_{\text{iso}} = \frac{1}{3}(R_{xx} + R_{yy} + R_{zz})$

The *anisotropy,* $\Delta R = R_{zz} - \frac{1}{2}(R_{xx} + R_{yy})$. The convention for choosing X, Y, and Z is such that $|R_{zz} - R_{\text{iso}}| \geq |R_{xx} - R_{\text{iso}}| \geq |R_{yy} - R_{\text{iso}}|$. Another quantity often referred to as anisotropy is δ which is related to ΔR: $\delta = \frac{2}{3}\Delta R$.

The *asymmetry,* η is a dimensionless quantity defined as

$\eta = 3(R_{yy} - R_{xx})/2\Delta R \equiv (R_{yy} - R_{xx})/\delta$

Be aware that different conventions exist for defining quantities such as anisotropy. Namely, if prior to diagonalisation the isotropic part (R_{iso}) has been separated off, one

obtains, after diagonalisation, a traceless tensor of the form

$$\sigma = \delta \begin{pmatrix} -\frac{1}{2}(1+\eta) & 0 & 0 \\ 0 & -\frac{1}{2}(1-\eta) & 0 \\ 0 & 0 & 1 \end{pmatrix} \tag{1.14}$$

with the anisotropy parameter $\delta = R_{zz}$ and the asymmetry parameter $\eta = \frac{R_{yy}-R_{xx}}{R_{zz}}$. Given a certain orientation of the PAS with respect to the external magnetic field in terms of the polar angles θ and ϕ, the resulting resonance frequency can be given by

$$\omega = \omega_{\text{iso}} + \omega_{\text{aniso}} = \omega_{\text{iso}} + \frac{1}{2}\delta(3\cos^2\theta - 1 - \eta\sin^2\theta\cos 2\phi) \tag{1.15}$$

Two Hamiltonians of dominant importance for the present work are described below.

Chemical Shift Interaction

The electrons of a molecule partly shield the nucleus from the external magnetic field by a small induced field that is related to the external field via a tensor quantity – the chemical shift tensor σ_{CSA}: $\mathbf{B}_{\text{ind}} = -\sigma_{\text{CSA}}\mathbf{B}_0$. As electrons are, in general, not distributed spherically around a given nucleus, this shielding will be anisotropic (i.e. in general, $\mathbf{B}_{\text{ind}} \nparallel \mathbf{B}_0$). The chemical shift interaction is bilinear in its field dependence and spin-operator dependence:

$$\mathscr{H}_{\text{CSA}} = \gamma\hbar\,\mathbf{I}\sigma_{\text{CSA}}\mathbf{B_0} = \gamma(\mathbf{I}_x\sigma_{xz} + \mathbf{I}_y\sigma_{yz} + \mathbf{I}_z\sigma_{zz})B_0 \tag{1.16}$$

Here, $\sigma_{\alpha\beta}$ are elements of a tensor in the laboratory frame of reference where $\mathbf{B_0}$ points along the z axis, i.e. $\mathbf{B_0} = (0, 0, B_0)^{\text{T}}$. The asymmetry of this interaction usually does not vanish. The strength of the interaction varies between 5 kHz for aliphatic carbon atoms and 12 kHz for carbonyl carbons at a field of 11.74 Tesla (500 MHz proton Larmor frequency).

Dipolar Coupling

Another anisotropic interaction commonly encountered in solids is dipolar coupling. It is symmetric and its tensor has the form

$$\mathbf{D} \propto \begin{pmatrix} 1 & 0 & 0 \\ 0 & 1 & 0 \\ 0 & 0 & -2 \end{pmatrix} \tag{1.17}$$

in the PAS. The PAS has its z axis aligned along the internuclear vector between the two coupling nuclei. Contrary to the chemical shift interaction, this is a two-particle interaction that is bilinear in the spin operators of the two involved spins. From classical experience, the energy (scale and angular dependence) of a dipole in a dipole field is known and can be put into quantum mechanical terms:

$$\begin{aligned}\mathscr{H}_{\mathrm{D}} =& \hbar \sum_{i,k} \mathbf{I}^{\mathrm{i}}\mathbf{D}\mathbf{I}^{\mathrm{k}} \\ =& \frac{\gamma_1\gamma_2\hbar^2}{4\pi}(r^{-3}\mathbf{I}_1\mathbf{I}_2 - 3r^{-5}(\mathbf{I}_1\cdot\mathbf{r})(\mathbf{I}_2\cdot\mathbf{r})).\end{aligned} \tag{1.18}$$

If expanded in polar coordinates, one arrives at the so-called alphabet expansion containing a secular term ($\mathbf{I}_{1\mathrm{z}}\mathbf{I}_{2\mathrm{z}}(1-3\cos^2\theta)$), a flip-flop term important for spin diffusion ($-\frac{1}{4}(\mathbf{I}_{1+}\mathbf{I}_{2-}+\mathbf{I}_{1-}\mathbf{I}_{2+})(1-3\cos^2\theta)$), and four more single- and double-quantum terms. For a heteronuclear two-spin system, only the secular term contributes significantly to the total energy and is included in the truncated Hamiltonian. For the homonuclear two-spin case, the spin states $\alpha\beta$ and $\beta\alpha$ are degenerate as far as the Zeeman Hamiltonian is concerned. This means that the above-mentioned flip-flop term is now secular too, i.e. has a direct effect on energies.

Various reoccuring techniques have been used throughout the experimental part of the present work. They are frequently used as building blocks to assemble more complicated experiments. A review of how they function is provided in Sections 1.2.2 to 1.2.5.

1.2.2 Dipolar Decoupling

Amongst the strongest spin interactions in solids are heteronuclear dipolar couplings. In liquid-state NMR these couplings are averaged out due to isotropic tumbling on the time scale shorter than the acquisition time. In solids, however, high-power decoupling must be performed. High-power decoupling poses a challenge to probe and filter design as well as receiver units but has been solved for most of the nuclei combinations (proton-carbon in the present case). For nuclei with close resonance frequencies such as ^{19}F and ^{1}H (for instance see Reinsberg [1998]) the technical difficulties remain. Fig. 1.8a in Section 1.2.3 shows the application of proton decoupling during carbon acquisition after ^{13}C polarisation has been created via cross polarisation (CP).

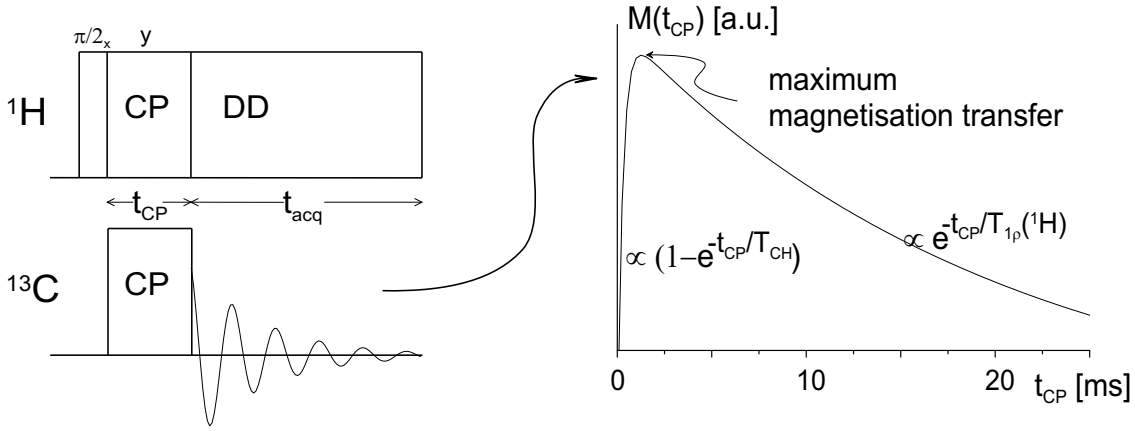

Figure 1.8: a) CP pulse sequence under dipolar decoupling (DD) b) Dilute-spin magnetisation as a function of contact time

1.2.3 Cross Polarisation

NMR studies of organic compounds most often involve the two nuclei proton and carbon. Although protons remain unsurpassed with respect to their high magnetogyric ratio and relative abundance, a number of distinct advantages of ^{13}C NMR exist. Carbons frequently exhibit higher chemical-shift anisotropies revealing useful clues about orientation (and thus rotational motion). Carbons are found at the backbone of molecules whereas protons tend to appear in the periphery.

Despite these advantages, ^{13}C NMR is hampered by long T_1-relaxation delays, low natural abundance, and a 75% smaller magnetogyric ratio than protons. While low natural abundance can only be circumvented by costly isotopic labelling, the other two can be rectified by the technique of cross polarisation (CP) introduced by Hartmann and Hahn [1962]. Fig. 1.8a depicts the sequence of steps for a CP experiment. Using a $\frac{\pi}{2}$ pulse, transversal magnetisation is created that is then 'spin-locked' by a pulse immediately following the first pulse but with a phase different by 90°. Together with the spin locking on the proton channel, a spin-lock pulse on the carbon channel gives rise to a ^{13}C-magnetisation build up. In order to achieve efficient polarisation transfer, energy levels of both spin species have to be matched. This is accomplished by satisfying the so-called Hartmann-Hahn matching condition for spin-$\frac{1}{2}$ systems:

$$\gamma_{\mathrm{H}} B_{1\mathrm{H}} = \gamma_{\mathrm{C}} B_{1\mathrm{C}}. \tag{1.19}$$

The gain in intensity from using cross polarisation is twofold. One factor of 4 in intensity is due to the ratio of magnetogyric ratios: $\gamma_{^1\mathrm{H}}/\gamma_{^{13}\mathrm{C}} \approx 4$. The magnitude of the other depends on the speed up due to a shorter repetition time of scans – normally ^{1}H spin-lattice relaxation times are much shorter than ^{13}C spin-lattice relaxation times.

An important, adjustable parameter for a CP experiment is the contact time, t_{CP}. By correctly choosing t_{CP} one can achieve spectral selectivity in addition to improved signal intensity. A convenient treatment of CP dynamics is based on a thermodynamic approach suggested by Abragam [1961] and Mehring [1983]. Under the assumption of CP from an abundant spin bath (e.g. ^{1}H) to a dilute spin bath (e.g. ^{13}C), one arrives at the following relationship describing the (carbon) magnetisation dependence on the contact time, t_{CP}:

$$M(t_{\mathrm{CP}}) \propto (1 - \exp(-\alpha t_{\mathrm{CP}})) \exp(-\beta t_{\mathrm{CP}}) \tag{1.20}$$

Fig. 1.8b shows a typical development of the ^{13}C magnetisation in a CP experiment of an organic solid. The sharp initial increase is due to the time constant α, which is mainly governed by the ^{1}H-^{13}C cross-relaxation rate, t_{CH}. Once the magnetisation curve reaches a maximum, it decays according to the shorter of the two spin-lattice relaxation rates in the rotating frame, usually $T_{1\rho}(^1\mathrm{H})$. More exactly, the time constants are given by:

$$\alpha = \frac{1}{T_{\mathrm{CH}}} + \frac{1}{T_{1\rho}(^{13}\mathrm{C})} - \frac{1}{T_{1\rho}(^1\mathrm{H})} \qquad \beta = \frac{1}{T_{1\rho}(^1\mathrm{H})}. \tag{1.21}$$

For a rigorous treatment of cross relaxation in double resonance see Demco et al. [1975]. If the assumption of non-dilute S spins does not hold, consult Reinsberg et al. [2000]; For an arbitrary number of spin bath see Hazendonk et al. [2001].

1.2.4 Filters

Often, it is desirable to suppress parts of the signals. These signals can stem from imperfections of a pulse sequence, or from unwanted coherences that arise together with desired coherences. In many cases, unwanted signals can be suppressed based on their different relaxation behaviour if these relaxation processes occur on different time scales.

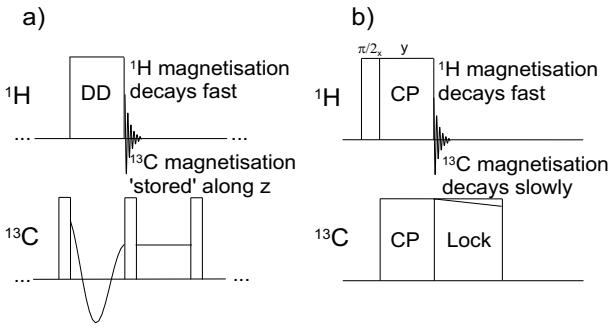

Figure 1.9: a) z filter after ^{13}C evolution, b) $T_{1\rho}$ filter after CP

Among relaxation processes, spin-lattice relaxation is the slowest process ($T_1 \approx$ seconds) followed by spin-lattice relaxation in the rotating frame ($T_{1\rho} \approx$ milliseconds). Relaxation of coherence, i.e. transverse magnetisation, is usually quicker ($T_2 \lessapprox$ milliseconds). Filters can harness these different relaxation behaviours: A z filter will flip magnetisation parallel to the z axis along which it will decay very slowly with T_1. In the meantime, transverse magnetisation of any nucleus will decay much quicker with T_2. After a waiting time of $\approx$ 1 ms, z magnetisation can be flipped back to be read out or to be used further in a pulse sequence. Similarly, a $T_{1\rho}$ filter can be used to spin lock magnetisation on one channel while coherence in a different channel decays, again with T_2.

Fig. 1.9 shows the two common types of filters: z filter and $T_{1\rho}$ filter.

1.2.5 Spin Diffusion

Magnetisation transfer in solids can happen by means of homonuclear dipolar coupling. In principle, spin-flip processes (the responsible part of the dipolar Hamilton, $\mathscr{H}_\mathrm{D}$, reads $\frac{1}{4}(\mathbf{I}_1^+\mathbf{I}_2^- + \mathbf{I}_1^-\mathbf{I}_2^+)(1 - 3\cos^2\theta)$) cause the passing on of coherence. It is not at all obvious why this coherent process is termed and described as *diffusion*, an inherently incoherent

process. In fact, the reversible nature of spin diffusion has been shown by inverting the sign of dipolar coupling. Zhang et al. [1992] used the fact that under spin-lock conditions dipolar couplings are scaled by a factor of $-\frac{1}{2}$ to prove the coherent nature of spin diffusion. Further relevant studies have been performed by Pastawski et al. [1995] (conditions for polarisation echos) and, later, Tomaselli et al. [1996] (polarisation echos also under MAS). Nevertheless, the spin-coherence exchange is often treated as diffusion is supported by striking experimental evidence. Section 4.1 summarises the mathematical description of diffusion. The derivation of the spin-diffusion equation has been attempted from several (not very convincing) sides: A density-matrix approach by Lowe and Gade [1967] makes the questionable assumption that fast T_2 relaxation assures a diagonal density matrix for the duration of the experiment. Similarly, the formalism by Mori and Kawasaki [1962] can not do without an ad-hoc assumption in order to arrive at the diffusion equation. More convincingly, Schmidt-Rohr and Spiess [1994] showed that a large numbers of spins together with a spectrum of dipolar coupling constants result in sufficient dampening of spin-wave oscillations. Their simulations of a coupled multi-spin system enables the observation of an essentially diffusive process.

1.3 NMR Experiments Elucidating Dynamic Phenomena

Among the various techniques elucidating dynamical phenomena at T_g, NMR holds a unique position. It represents, at present, the most powerful and versatile tool compared to other techniques such as dielectrics, optical methods, or dynamic light scattering. Its success is partly based on the fact that the interrogation of spin properties does not influence thermal molecular motion. This holds because spin energies are much smaller than thermal energies at the temperature range of interest of $T > T_\mathrm{g}$: $E_\mathrm{thermal}/E_\mathrm{spin} \gtrapprox 10^5$.

1.3.1 Relaxation-Time Experiments

A non-equilibrium spin state will eventually return to equilibrium by means of relaxation. The path for relaxation is paved by spin transitions that are induced by fluctuating fields which can be achieved by dipole-dipole, chemical shift anisotropy, spin rotation or quadrupolar mechanisms. For each of these mechanisms, a given nucleus experiences fluctuating fields due to motion (its own, that of neighbouring molecules, or groups of atoms). Therefore, relaxation measurements provide a tool for investigating molecular motion.

Molecular motion (vibration, rotation, diffusion etc.) occurs at a distribution of frequencies usually described by a spectral density function,

$$J(\omega) = \frac{2\tau_c}{1+\omega^2\tau_c^2}, \tag{1.22}$$

which is a measure of the probability of finding a component of the motion at a given frequency, ω. The rotational correlation time, τ_c, describes the average time a molecule needs to complete a rotation of one radian. The higher the probability of finding particles moving with $\omega \approx \omega_{\text{Larmor}}$ the faster the transition of spin states will be and, thus, the more quickly relaxation will occur. Three main regimes can be distinguished: (i) The *extreme narrowing limit*, $\omega^2\tau_c^2 \ll 1$, is usually encountered in small molecules and low viscosity solvents at ambient temperatures. With decreasing tumbling rates, spin-lattice relaxation times decrease until the system reaches the (ii) *intermediate motional region*, $\omega^2\tau_c^2 \approx 1$. Polymers and biological macromolecules are usually in the (iii) *slow motional regime*, $\omega^2\tau_c^2 \gg 1$, where spin-lattice relaxation is once again reduced. In ^{1}H NMR and ^{13}C NMR of molecules primarily containing protons and carbons dipole-dipole relaxation is the dominant relaxation mechanism. Note that ω_{Larmor} depends on the external magnetic field resulting in a B_0 dependence of the T_1 minimum. For dipolarly coupled spins the following relationship can be derived [Spiess, 1978]:

$$\begin{aligned} T_1^{-1} &\propto \quad J(\omega_{\text{Larmor}}) + 4J(2\omega_{\text{Larmor}}) \\ T_2^{-1} &\propto \quad 3J(0) + 5J(\omega_{\text{Larmor}}) + 2J(2\omega_{\text{Larmor}}) \end{aligned} \tag{1.23}$$

Fig. 1.10b shows the general dependence of the relaxation times on molecular mobility, which is usually proportional to temperature. Fig. 1.10a depicts how T_1 measurements

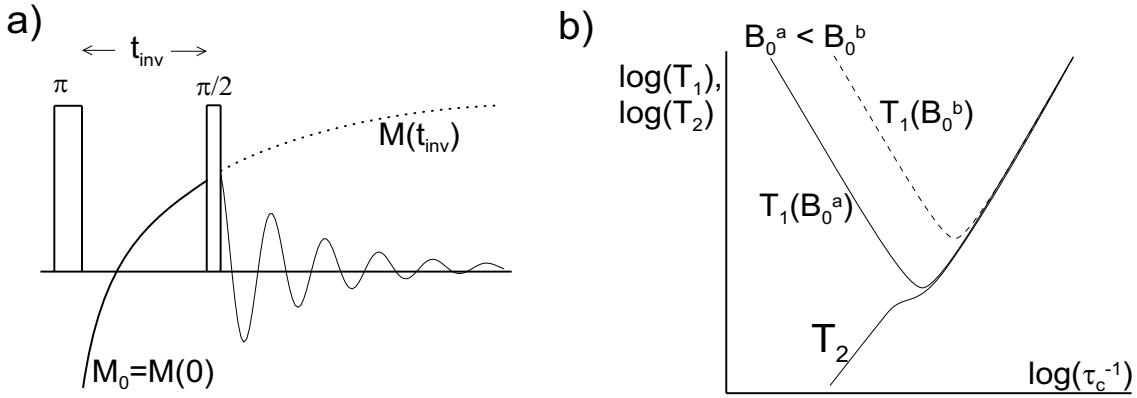

Figure 1.10: a) Measurement of the spin-lattice relaxation time, T_1, by inversion recovery. b) Schematic illustration of the dependence of T_1 and T_2 on molecular tumbling. Higher magnetic fields (dashed line) result in a shifted minimum of T_1.

are usually achieved: after the inversion of the spin state (either by a π pulse or, for ^{13}C, CP followed by a $\frac{\pi}{2}$ pulse), a waiting time t_{inv} is put. The intensity of recovered magnetisation is monitored by a subsequent $\frac{\pi}{2}$ read pulse. A technique applied to nuclei with very long T_1s is saturation recovery: Following a series of fast pulses that serve to equalise spin-state populations, magnetisation recovery is monitored after various delays by application of a $\frac{\pi}{2}$ read pulse.

In glass formers with a spatial distribution of motional relaxation times, one would expect a distribution of spin-lattice relaxation times. This is usually not, however, observed in ^{1}H and ^{13}C NMR. The explanation is that polarisation is quickly spread throughout the sample due to effective spin diffusion among protons. This mechanism is absent for ^{2}H NMR where nonexponential relaxation can be observed as, e.g., for OTP by Schnauss et al. [1990]. While this technique can not be used to estimate length scales, lifetimes of heterogeneities must clearly be on the order of 1 s. Only when the temperature gets raised to 10% above T_{g}, exponential relaxation is observed. This is because motional averaging takes place as τ_α approaches τ_{c} and $\tau_\alpha \approx \tau_{\text{c}} \ll T_1$.

Measurement of transverse dephasing times, T_2, or spin-lattice relaxation times in the rotating frame, $T_{1\rho}$, yield relaxation times that are sensitive to motion on longer time scales. The former can be achieved by spin-echo sequences or CPMG sequences. The latter can be obtained by a variable spin-lock experiment.

1.3.2 Multi-Time Correlation Experiments

The techniques discussed in the previous section are predominantly used to study motion on a time scale of $10^{-10} \ldots 10^{-6}$ s. It is, however, possible to explore motion up to time spans just below the ultimate NMR limit of T_1 – the point at which spin energies have dissipated into the bath of thermal molecular motion. The route to investigation of slow processes was opened by Jeener and Broekaer [1967] by their implementation of a three-pulse sequence for the study of homonuclear coupled spins. Echo experiments by Spiess [1980] facilitated the exploitation of quadrupolar interaction for the study of very slow dynamics in solids. Static exchange spectra allow the direct determination of motional geometries [Schmidt et al., 1986, 1988].

Fig. 1.11 shows the general principle of the three-pulse experiment. Transverse magnetisation is created and is allowed to evolve under the influence of chemical shift interaction. With a $\frac{\pi}{2}$ pulse of appropriate phase either the cosine or sine component is 'saved' along z. In a very short time (< 1 ms), remaining transverse components dephase, leav-

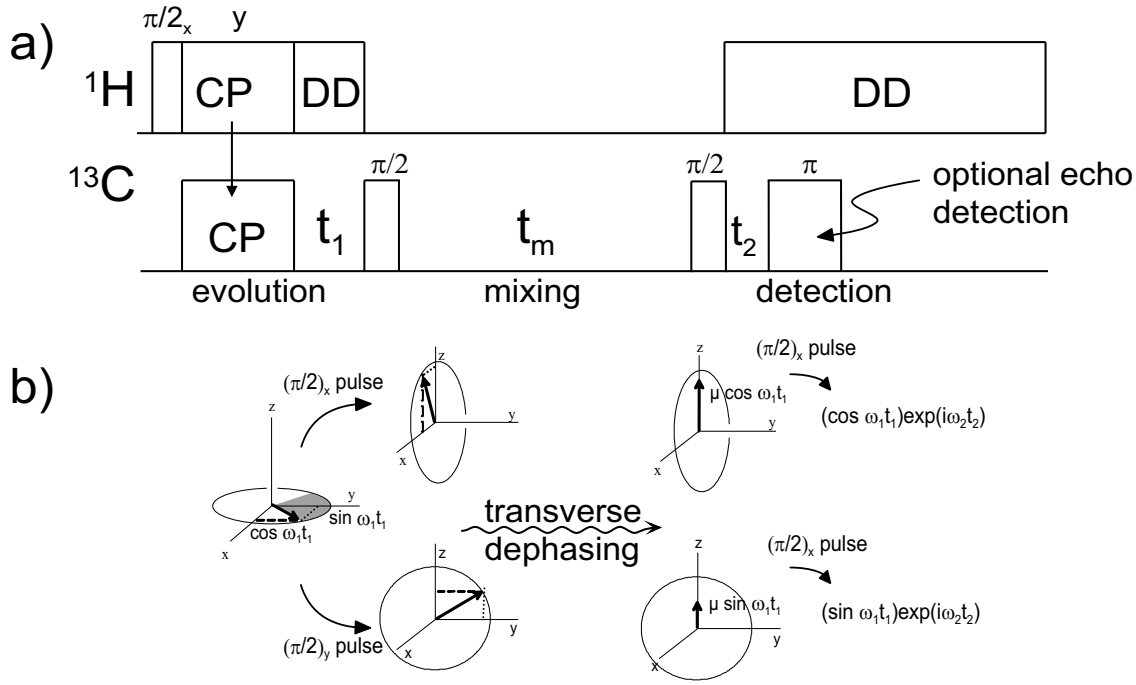

Figure 1.11: Three-Pulse sequence with CP and dipolar decoupling (a) and its working principle (b). Either the sine or cosine component of the evolved magnetisation is saved along the z axis at the start of the mixing time. This component ($\sin \omega_1 t_1$ or $\cos \omega_1 t_1$) modulates the FID acquired during t_2.

ing the projection ($\cos\omega_1 t_1$ or $\sin\omega_1 t_1$) parallel to the z axis. After the mixing time, t_m, magnetisation is flipped back into the xy plane for detection. This experiment has to be changed slightly for use with quadrupolar nuclei: Magnetisation is initially created using a $\frac{\pi}{2}$ pulse and the two following pulses for storing and reading the magnetisation have flip angles of $\frac{\pi}{4}$. Note that this experiment can be performed in two ways.

2D Spectra

When the three-pulse experiment is used as a fully two-dimensional technique for the acquisition of 2D spectra, the mixing time is set to a constant value and the evolution time, t_1, is increased in equal steps. Thus, a two-dimensional data set results:

$$I_2(t_1, t_2, t_\mathrm{m}) = \langle \exp(i\omega_1 t_1) \exp(i\omega_2 t_2) \rangle \tag{1.24}$$

Two Fourier transformations one in each dimensions yield a 2D spectrum ($S_2(\omega_1, \omega_2) = \mathcal{F}_1(\mathcal{F}_2(I_2(t_1, t_2))))$ that represents the joint probability of finding a particle at frequency ω_1 at $t = 0$ and at frequency ω_2 at $t = t_\mathrm{m}$. To obtain absorptive spectra, a number of methods are used: Redfield and Kunz [1975] developed a technique called time proportional phase increment (TPPI). Another method to acquire a fully complex data set in both dimension is the States-Haberkorn method using a hypercomplex data set [States et al., 1982]. If spectra of low spectral width are acquired, one could afford recording a pure cosine dataset off resonance [Schmidt-Rohr and Spiess, 1994].

The distribution of exchange intensity in the $\omega_1\omega_2$ plane is determined by the time scale and geometry of motion as well as the anisotropy parameters of the interaction. If no exchange occurs over a span of t_m, a diagonal 2D spectrum is obtained. Elliptical exchange patterns arise if, under symmetric interaction, jumps about a well-defined angle take place.

2D Echo

Another approach is to leave the evolution time fixed and vary the mixing time. With $t_1 = t_\mathrm{p}$ one obtains

$$\begin{aligned} F_2^{\cos}(t_\mathrm{m}, t_\mathrm{p}) =& \langle \cos(\omega_1 t_\mathrm{p}) \cos(\omega_2 t_\mathrm{p}) \rangle \\ F_2^{\sin}(t_\mathrm{m}, t_\mathrm{p}) =& \langle \sin(\omega_1 t_\mathrm{p}) \sin(\omega_2 t_\mathrm{p}) \rangle, \end{aligned} \tag{1.25}$$

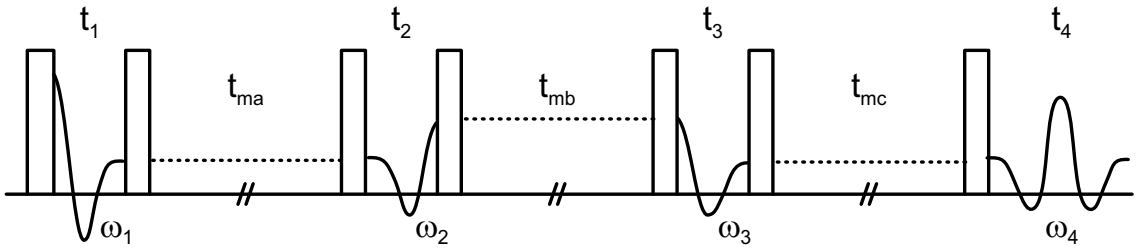

Figure 1.12: Combination of two 2D echo experiments to form a 4D exchange experiment.

depending on which phase regime used for acquisition. Adding both terms yields a two-time correlation function of the form

$$F_2(t_\mathrm{m}, t_\mathrm{p}) = \langle \cos((\omega_2 - \omega_1)t_\mathrm{p}) \rangle \tag{1.26}$$

It was proven by Böhmer et al. [1996] that for large enough $t_\mathrm{p}\delta$, the contribution of $F_2^{\sin}$ is negligible and $F_2^{\cos}$ characterises F_2 sufficiently. The correlation functions are usually obtained by analysing the signal in the time domain. The echo height directly yields the value of $F_2^{\sin}(t_\mathrm{m})$, $F_2^{\cos}(t_\mathrm{m})$, or $F_2(t_\mathrm{m})$, depending on the phase cycle, if one assures that no significant signal contributions come from nuclei other than the one of interest. This is usually achieved using isotopic enrichment.

The thus-acquired correlation function characterises the time dependence of the motion for a given geometrical sensitivity determined by the parameter $t_\mathrm{p}\delta$. If $t_\mathrm{p}\delta$ is relatively small, a molecular unit has to reorient a considerable amount before the argument $\omega_2 t_\mathrm{p}$ of the cosine function in F_2 differs significantly from $\omega_1 t_\mathrm{p}$ (see Eq. 1.15). If it does, the correlation function will be decreased accordingly. In other words, molecular reorientation associated with a significant change in $\omega_{1/2} t_\mathrm{p}$ will result in destructive interference and lead to signal attenuation. For large $t_\mathrm{p}\delta$, even very small orientational changes result in signal decay. This relationship is exploited if t_p-dependent measurements of correlation functions, F_2, are performed in order to reveal the geometry of the motion.

By the mechanism of interference, only magnetisation of those units that have not reoriented significantly survives a given mixing time, t_m. 'Significant reorientation' in this context means rotation by more than the given threshold $t_\mathrm{p}\delta$. For simulation and discussion of the filter properties in the light of nonlinear dependence of resonance frequency on orientation see Section 5.5.

The application of the 2D-echo experiment as a filter was used in a novel 'reduced four-dimensional' exchange NMR experiment by Schmidt-Rohr and Spiess [1991]. This marked the first time a slow subset was selected in a dynamically heterogeneous sample. On one hand, it proved the heterogeneous nature of relaxation in a glass former. On the other hand, it introduced the use of higher-order correlation functions

$$I_4(t_1, t_2, t_3, t_4) = \langle \exp(i\omega_1 t_1) \exp(i\omega_2 t_2) \exp(i\omega_3 t_3) \exp(i\omega_4 t_4) \rangle \tag{1.27}$$

to NMR when applied to the study of dynamics. Fig. 1.12 shows the principle of a 4D exchange experiment, which is capable of measuring higher order correlation functions at four points in time: 0, t_{ma}, $t_{\mathrm{ma}} + t_{\mathrm{mb}}$, $t_{\mathrm{ma}} + t_{\mathrm{mb}} + t_{\mathrm{mc}}$ assuming that $t_{\mathrm{i}} \ll t_{\mathrm{m}\alpha}$.

Given obvious time and memory constraints, a 4D exchange experiment is performed in a reduced fashion, i.e. some of the variable delays are set to constant values resulting in a projection onto lower dimensions. In this form, the experiment is best interpreted in terms of the filter picture introduced above: A slow subset is selected by the first three pulses. The mixing time t_{ma} and the evolution times t_1 and t_2, both of which determine angular selectivity, are fixed. The dynamics of this subensemble is allowed to evolve before a second filter follows. Thus, the evolution in time of the slow subset can be monitored. Chapter 3 is devoted to simulations of dynamics investigated using this kind of technique.

1.3.3 Experiments under MAS

Although the present work studies dynamic properties under static conditions, we shall briefly mention some of the techniques that have been developed for the study under magic-angle spinning (MAS) conditions.

The purpose of rapid sample rotation about an axis at an angle of $\theta = 54.7^\circ$ with respect to the magnetic field is to remove anisotropic interactions in solids. Spinning 'sufficiently' fast in order to remove the interaction λ such as dipole-dipole or chemical shift anisotropy interaction is achieved if spinning rates exceed the interaction strength: $\omega_{\mathrm{R}} > \omega_\lambda$. While line narrowing is a desirable goal to achieve, useful information is lost if interactions are removed. A number of experiments have been devised to reintroduce

these orientation-dependent interactions. In the framework of multiple quantum spectroscopy, techniques for the recoupling of homonuclear dipolar interaction[Geen et al., 1995; Feike et al., 1996; Graf et al., 1997] have been developed. Heteronuclear dipolar interactions have been first recoupled by Gullion and Schaefer [1989]; this method was presented in a multiple-quantum framework by Saalwächter [2000].

Several attempts have been made to harness chemical shift anisotropy in multidimensional experiments under MAS conditions for the study of dynamics [Yang et al., 1989; Hagemeyer et al., 1998]. Only recently, though, has an experiment been proposed that has the potential these other techniques were lacking [deAzevedo et al., 1999]. Centreband Only Detection of EXchange (CODEX) allows the extraction of time scale and geometry of motion in a site-specific fashion. Given favourable signal conditions (efficient cross polarisation, short repetition times etc.), this approach circumvents the need for costly isotopic labelling.

Chapter 2

Substances

A number of criteria influences the choice of a particular model substance. From the vast group of glass formers one must choose organic glass formers if ^{13}C NMR is to be performed. In principle the experiments could be performed using other nuclei as well, in order to allow the study of inorganic glasses. The glass transition temperature has to lie in an accessible temperature range (usually unconveniently high for inorganic glass formers). The carbon chemical shift tensor should exhibit a reasonable chemical shift anisotropy. The motion of the tensor should directly follow the motion responsible for the α relaxation. This means that the ^{13}C probe should preferably not be located in peripheral groups, e.g. mobile and decoupled side-group of polymers, or phenyl rings that perform independent ring flips.

Over the course of this work, several supercooled liquids were investigated. According to the above criteria, two systems from the different classes of glass formers were selected. Glycerol was chosen as an example of an intermediate glass former. *o*-terphenyl was investigated as the substance representing weak glass formers.

2.1 Glycerol

Glycerol (1,2,3-propanetriol) labelled at the central carbon was purchased from Aldrich and diluted with an equal amount of regular glycerol (99.8%, Aldrich). $CuNO_3$

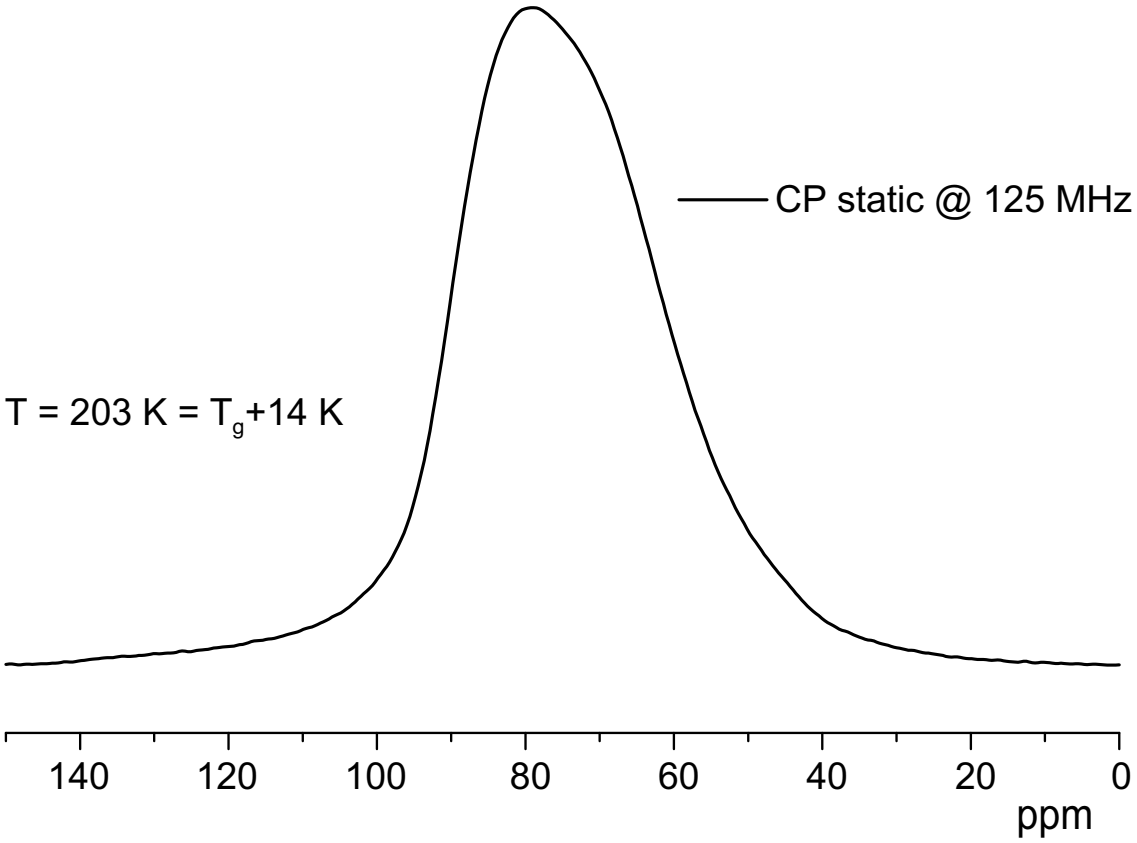

Figure 2.1: ^{13}C spectrum of ^{13}C-enriched glycerol measured at B_0=11.47 T using cross polarisation.

was used as spin relaxation agent at a low concentration of 0.1 wt%. Böhmer and Hinze [1998] believe that contamination with water is not problematic due to the related hydrogen-bonding nature of molecular interactions in water and glycerol. To avoid this potential uncertainty, the very hygroscopic sample was glass sealed. Glycerol can easily be supercooled and does not necessitate special precautions to prevent crystallisation as does *o*-terphenyl (cf. next section).

Fig. 2.1 shows the ^{13}C spectrum of glycerol as obtained from cross polarisation at $T = 205K$ K. With the edges blurred out due to the strong line broadening it is difficult to read off the principal values of the ^{13}C chemical shift tensor. The anisotropy can be estimated to be $\delta \approx 30$ ppm.

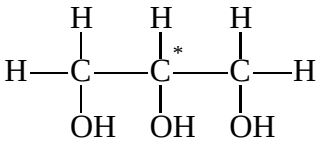

Figure 2.2: Chemical structure of glycerol, labelled at the central carbon.

2.2 *o*-terphenyl

OTP (1,1':2',1"-4'[^{13}C]terphenyl) labelled at the *meta* carbon of the central ring has been synthesised by Herbert Zimmermann. Appendix B provides information on the nine-step synthesis of OTP. To avoid ^{13}C-^{13}C spin diffusion, the sample was diluted with an equal amount of regular *o*-terphenyl (purchased from Fluka). The problem of long spin-lattice relaxation times at temperatures nearing T_g was overcome by adding a relaxation agent. $CuNO_3$, however, does not dissolve in *o*-terphenyl as it does in glycerol because hydrogen bonds do not play a role in inter-molecular interactions. Instead, $Cu(acac)_3$ was used at a concentration of less than 0.1 wt%. The concentration was chosen so that the measured spin-lattice relaxation parameter, $T_1(^1H)$, was at a convenient value of 2 s.

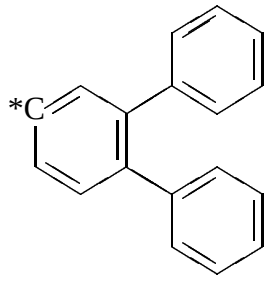

Figure 2.3: Chemical structure of *o*-terphenyl, labelled at the meta position of the central ring.

Another difficulty initially encountered was fast crystallisation at all temperatures above T_g. Heating above the melting point, T_m, and quenching to temperatures slightly above T_g did not sufficiently remove this behaviour for the duration of the experiments. To exclude heterogeneous crystallisation as reason for this unfavourable response, measures were taken to purify the sample. The crystalline *o*-terphenyl powder was dissolved in acetone that contained $Cu(acac)_3$ and filtered with a 2 μm filter. The solution was filled into a previously cleaned glass phial and the acetone was extracted under vacuum at 40°C. This glass phial was then glass sealed. The sample remained amorphous on the time scales of days and could thus be used for NMR experiments. Furthermore, crystallisation could still be detected inside the NMR probe because spin-lattice relaxation times of the *o*-terphenyl crystal rose considerably above 2 s. Similarly, rotational correlation times diverged. In a reduced 2D echo experiment, which took only 8 minutes, correlation times as well as temperature stability could be reliably tested.

Care was taken as the solution showed a tendency to phase separate into solutions of

Parameter	Value	Parameter-Determining Experiment
$T_1(^1\mathrm{H})$	2 s	inversion recovery
$T_1(^{13}\mathrm{C})$	100 s	inversion recovery after $^1\mathrm{H}\rightarrow{}^{13}\mathrm{C}$ CP
$T_{1\rho}(^1\mathrm{H})$	100 μs	variable spin-lock experiment
$T_{1\rho}(^{13}\mathrm{C})$	100 μs	variable spin-lock experiment

Table 2.1: Summary of Parameters Relevant for Experiments on *o*-terphenyl.

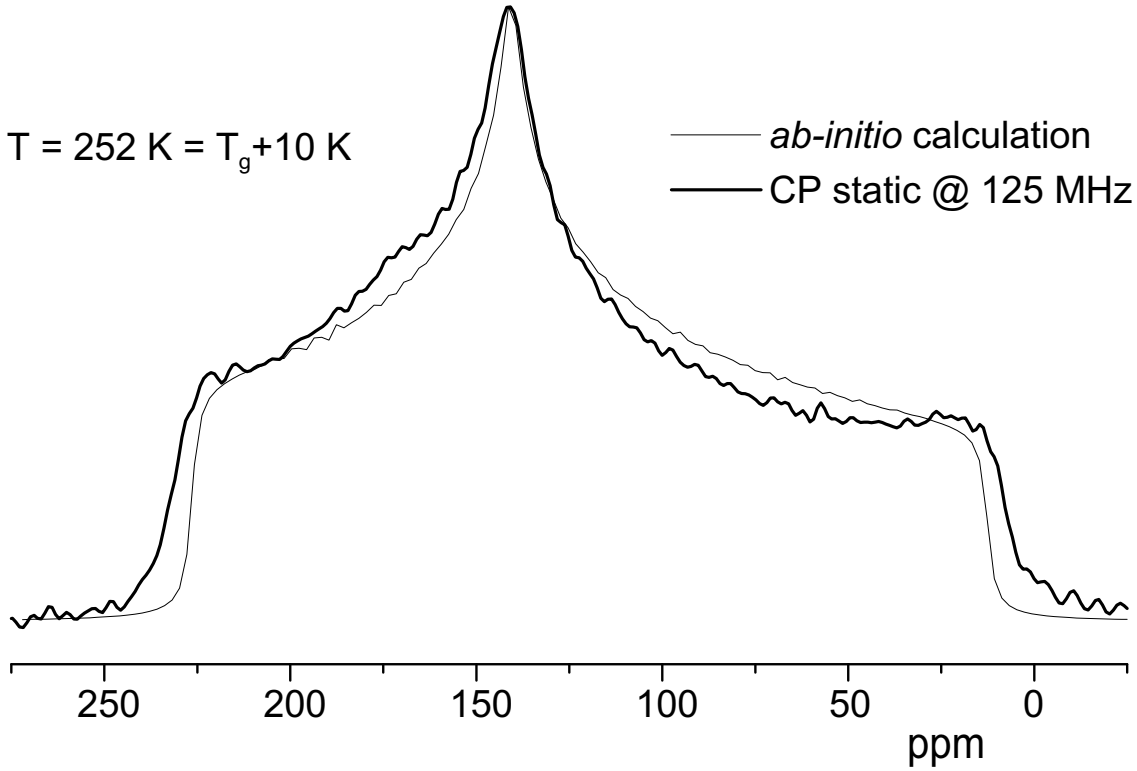

Figure 2.4: ^{13}C spectrum of selectively enriched *o*-terphenyl measured at B_0=11.47 T using cross polarisation (bold line). The experimental principal values are $\sigma_{\mathrm{xx}} = 232$ ppm, $\sigma_{\mathrm{yy}} = 141$ ppm, $\sigma_{\mathrm{zz}} = 8$ ppm. The chemical shift tensor has been calculated using Gaussian 98 (fine line) yielding $\sigma_{\mathrm{xx}} = 227$ ppm, $\sigma_{\mathrm{yy}} = 141,$ ppm, $\sigma_{\mathrm{zz}} = 13$ ppm.

higher and lower Cu^{2+}-ion concentrations as indicated by a pink hue in the upper portion of the sample. This, too, resulted in unfavourably long spin-lattice relaxation times, T_1. When heated above T_{m} and gently agitated, this concentration gradient vanished completely. As a result of high viscosity at temperatures close to T_{g}, phase separation did not occur during the NMR experiments.

Table 2.1 summarises all the parameters relevant for experiments on *o*-terphenyl.

They were determined by standard NMR experiments as listed in the last column for the respective parameter.

Fig. 2.4 shows a ^{13}C spectrum of OTP as obtained from cross polarisation under ^{1}H decoupling conditions. It is possible to directly measure the three principal values of the carbon chemical shift tensor $\sigma_{xx}, \sigma_{yy}, \sigma_{zz}$ (see Fig. 2.4 caption). The values translate into an isotropic chemical shift of $\sigma_{iso} = 127$ ppm, an anisotropy of $\delta = -119$ ppm, and an asymmetry of $\eta = 0.76$ (cf. Eqs. 1.13 and 1.14). Note that in the liquid-state NMR spectrum (solvent $CDCl_3$) the isotropic chemical shift of the enriched carbon was determined to be $\sigma_{iso,liquid} = 127.4$ ppm. Fig. 2.4 also displays results from CSGT [Keith and Bader, 1993] chemical-shift calculations at the DFT/BLYP [Becke, 1988; Lee et al., 1988] level of theory using the basis set 6-311G**. The three principal values are $\sigma_{xx} = 227$ ppm, $\sigma_{yy} = 141,$ ppm, $\sigma_{zz} = 13$ ppm resulting in anisotropy $\delta = -114$ ppm and asymmetry $\eta = 0.75$. The isotropic shift from DFT has been corrected to match the isotropic shift from the experiment as absolute shift values are notoriously less accurate for ab-initio calculations. However, for relative values (i.e. anisotropy, asymmetry) we find a reasonable agreement between the experimental and calculated tensor.

Chapter 3

The Rate Memory – Simulations of 4D Experiments

As outlined in Chapter 1, the existence of dynamic heterogeneities poses the question of how long such heterogeneities persist. A variety of experiments on a diversity of glass formers answered this question [Schmidt-Rohr and Spiess, 1991; Cicerone et al., 1995b; Heuer et al., 1995; Böhmer et al., 1996; Schiener et al., 1996; Russell et al., 1998]. The present chapter presents simulations that help the interpretation of available data from multidimensional NMR experiments [Tracht, 1998]. A brief outline and discussion of the experimental NMR data is given in Section 3.1. The two subsequent Sections 3.2 and 3.3 deal with the details and conclusions of the Monte Carlo simulations.

The intuitive approach to investigate rate fluctuations is to select a slow subensemble prior to the subsequent monitoring of the redistribution of these slow relaxation rates. This view is sketched in Fig. 3.1 for a bimodal rate distribution. As shown, a 2-D echo filter (essentially a 2-D exchange experiment) selects the slower of two subensembles. During a mixing time, t_{m2}, the redistribution of rates occurs. A second 2-D echo filter accomplishes the final selection of the slow portion of the sample. The decay of the function proves that (i) the ensemble is heterogeneous, and (ii) on what time scale the redistribution happens.

Equivalently, this experiment can be viewed as the direct measurement of a four-time

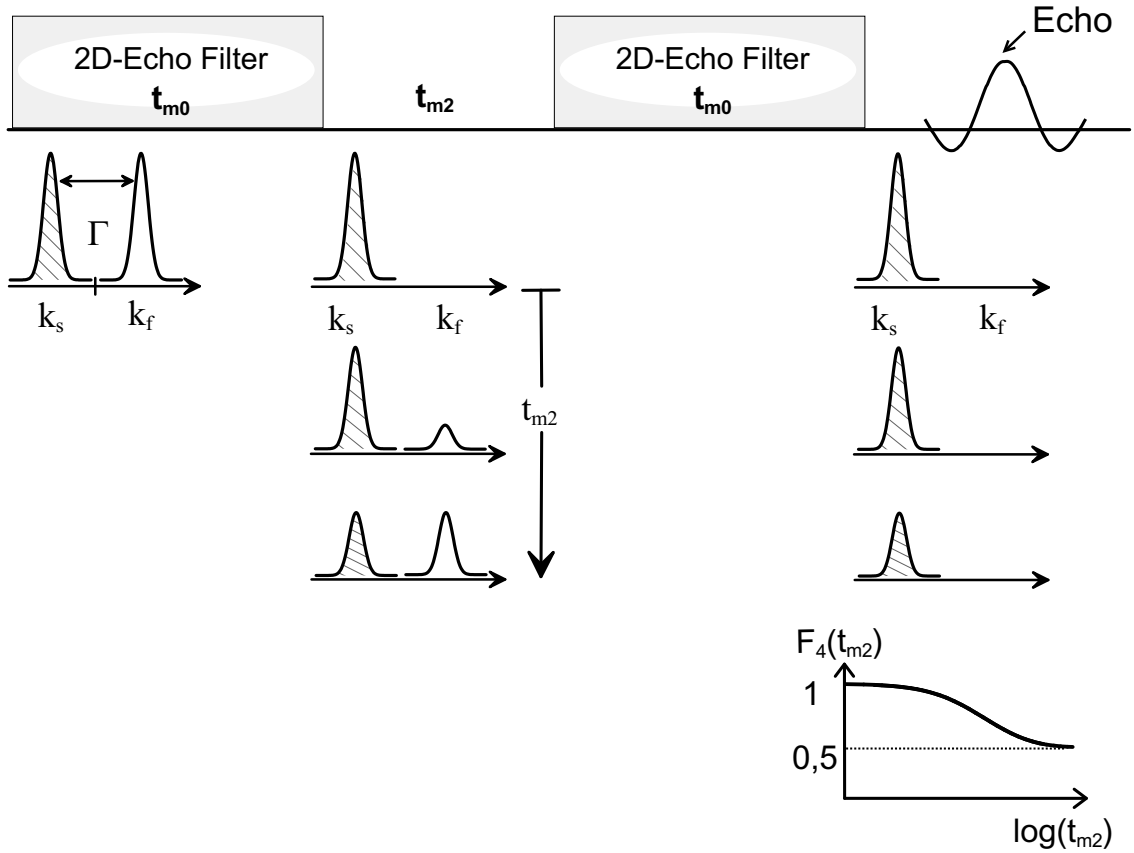

Figure 3.1: Principle of the 4D experiment. During the first mixing time t_{m0} a slow subensemble is selected and its return to equilibrium with time t_{m2} is monitored.

correlation function, such as:

$$\begin{aligned} F_4(t_{\mathrm{m1}}, t_{\mathrm{m2}}, t_{\mathrm{m3}}) &= \langle \cos(t_{\mathrm{p}}(\omega(t_{\mathrm{m1}}) - \omega(0)) \\ &\quad \times \cos(t_{\mathrm{p}}[\omega(t_{\mathrm{m1}} + t_{\mathrm{m2}} + t_{\mathrm{m3}}) - \omega(t_{\mathrm{m1}} + t_{\mathrm{m2}}))) \rangle. \end{aligned} \tag{3.1}$$

This correlation function can be measured using a reduced, four-dimensional NMR experiment, as depicted in Fig. 3.2. Appropriate phase cycling allows the acquisition of exactly the function given in Eq. 3.1.

Heuer [1997] showed how to analyse four-time correlation functions within the theoretical framework of the rate exchange. Merely on the basis of a known two-time correlation function F_2 and a single parameter Q, a theoretical curve F_4^Q can be found that

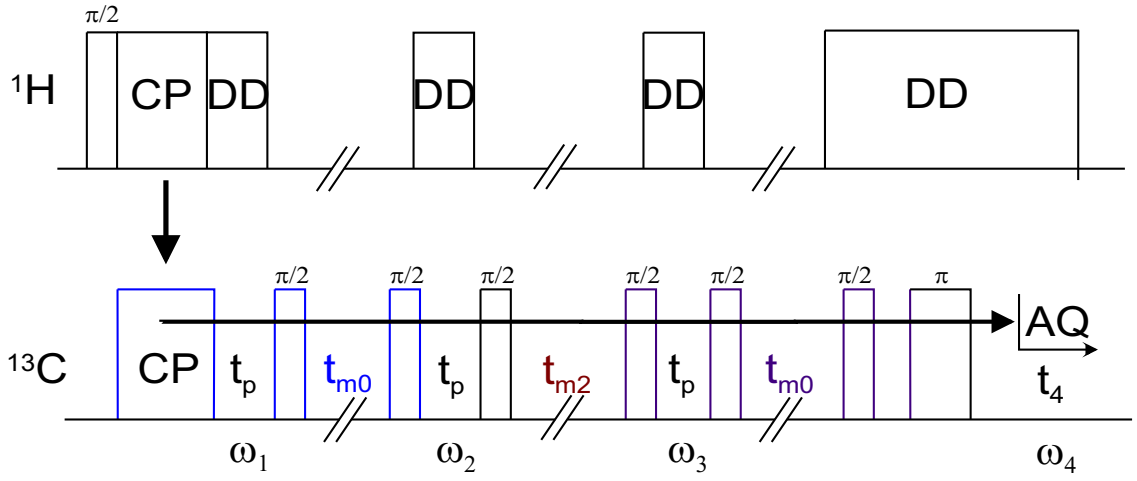

Figure 3.2: Pulse sequence for the (reduced) four-dimensional exchange experiment; $t_{m1} = t_{m3} =: t_{m0}$ is set to select a portion of the slow ensemble while t_{m2} is incremented to monitor the rate exchange

fits the experimental data, $F_4(t_{m2})$, well[1]:

$$F_4^Q(t_{m2}) = \left[F_2(2t_{m0} + t_{m2}/Q) + \frac{(F_2(t_{m0}) - F_2(t_{m0} + t_{m2}/Q))^2}{1 - F_2(t_{m2}/Q)}\right] \frac{1}{F_2(2t_{m0})} \qquad (3.2)$$

The parameter Q is interpreted as the number of relaxation processes after which a molecule (or re-orienting unit for polymers) has a mobility that is uncorrelated to its initial mobility. For a system with only two different jump rates as depicted in Fig. 3.1, the rate memory can be defined as the ratio of the slow relaxation rate, k_s, and the exchange rate, Γ, via $Q = k_s/\Gamma$. In the general case of a continuous rate distribution, the approximation

$$Q \approx 1 + k_s/\Gamma \qquad (3.3)$$

holds as long as the exchange rate Γ_{ij} between two states i and j with relaxation rates k_i and k_j, respectively, scales like $\Gamma_{ij} \propto k_i k_j$. Even in the case of more complex distributions of exchange rates, Eq. 3.3 sufficiently describes the observed rate-memory parameter, Q. For these more complex scenarios, the rate-memory parameter, Q, will depend on the choice of t_{m0} because the meaning of k_s is the average relaxation rate of the selected subensemble. A variation in t_{m0} will change the size of the subensemble and, thus, also the value of the rate k_s.

[1] Appendix A of [Heuer, 1997] gives an exact, recursive algorithm for the determination of the four-time correlation function F_4^Q. It deviates only marginally from the approximate solution given in Eq. 3.2

Sillescu [1996] discusses a simple rate-exchange model for non-Markovian molecular reorientation. This model was later generalised and embedded in a free energy landscape model by Diezemann et al. [1998].

3.1 Available Experimental Data

Observations of rate exchange processes (for one exception see below) revealed that these processes occur on the same time scale as the molecular reorientation associated with the α relaxation: The first successful experiment at all was performed by Schmidt-Rohr and Spiess [1991]. The novel, reduced, four-dimensional exchange NMR experiment was carried out on PVAc at $T = T_{\mathrm{g}} + 20$ K and clearly proved that fluctuations of the rates occur within times scales on the order of the longest correlation times. The application of this pulse sequence to a ^{13}C-enriched sample together with the introduction of the rate memory as the experimental observable [Heuer et al., 1995] allowed a more exact determination of the time scale of rate fluctuations. Böhmer et al. [1996] used deuteron NMR and investigated the rate exchange processes in *o*-terphenyl; Their results further substantiates the notion of the same time scale for rate exchange and α relaxation. A non-NMR experiment, namely the observation of electric polarisation fluctuations using non-contact scanning probe microscopy by Russell et al. [1998], supported the general opinion of rate fluctuations being on the same time scale as the relaxation of the slow entities.

Cicerone et al. [1995b] reported exceptionally long rate memories in *o*-terphenyl. As they measured molecular rotation of probes very close to the glass transition, the temperature range did not overlap with the one of NMR experiments. Ediger [2000b] argued that a strong temperature dependence of the rate exchange parameter, Q, could resolve a conceivable discrepancy of the rate memory determined by different means.

In a recent study by Tracht et al. [1999a], an extensively detailed study of the 4D experiment on PVAc was presented. In particular, the influence of experimental parameters such as t_{m0} and t_{p} was investigated. This study provides a unique methodical tool to investigate the motional dynamics and complements previous results from 2D experiments

[Tracht et al., 1999b]. As the simulations presented in the present chapter have been motivated by the experimental NMR findings of this 4D study, they will be summarised below.

The angular sensitivity (as adjusted by the value of $t_{\mathrm{p}}\delta$) was varied for a fixed level of selection (as adjusted by t_{m0}). It was found that for small parameters $t_{\mathrm{p}}\delta$, i.e. sensitivity to large-angle jumps only, the rate memory, Q, is near the minimum of 1. If longer evolution times t_{p} are employed, Q rises to about 3. This can be seen in Fig. 5 of [Tracht et al., 1999a].

A variation of the level of selection was facilitated by changing the mixing time of the first and last dynamic filter, t_{m0}. This variation was attempted in two regimes. For low angular sensitivity the rate memory remained constant at the minimum of ca. 1. For a high angular sensitivity, the rate memory was marginally increased ($Q \approx 4$) for low levels of selection, i.e. short filter times t_{m0}. It remained constant at $Q = 3$ for smaller levels of selection. The results of these experiments are shown in Figs. 5 and 6 of [Tracht et al., 1999a]. In the following section, it has been attempted to capture these features by simulation and to propose models of motion that agree with the experimental findings.

3.2 Simulations

Due to the nature of 2$^{\mathrm{nd}}$ rank tensor interactions, 'heterogeneity' of the sample can also result from different orientations of molecules with respect to the magnetic field. In simulations we explore under what circumstances such a heterogeneity, which actually is an NMR artefact, can occur. We will then explore whether the 4D experiment offers clearer information on the geometry (small vs. large angle jumps) as compared to a 2D experiment.

Monte Carlo simulations of two-time and four-time correlation functions were carried out by evaluating the resonance frequency of the carbon. The CSA tensor under study had an orientation that changed according to the different jump and diffusion models simulated. The Larmor frequency ω was examined at two (F_2) or four (F_4) points of time

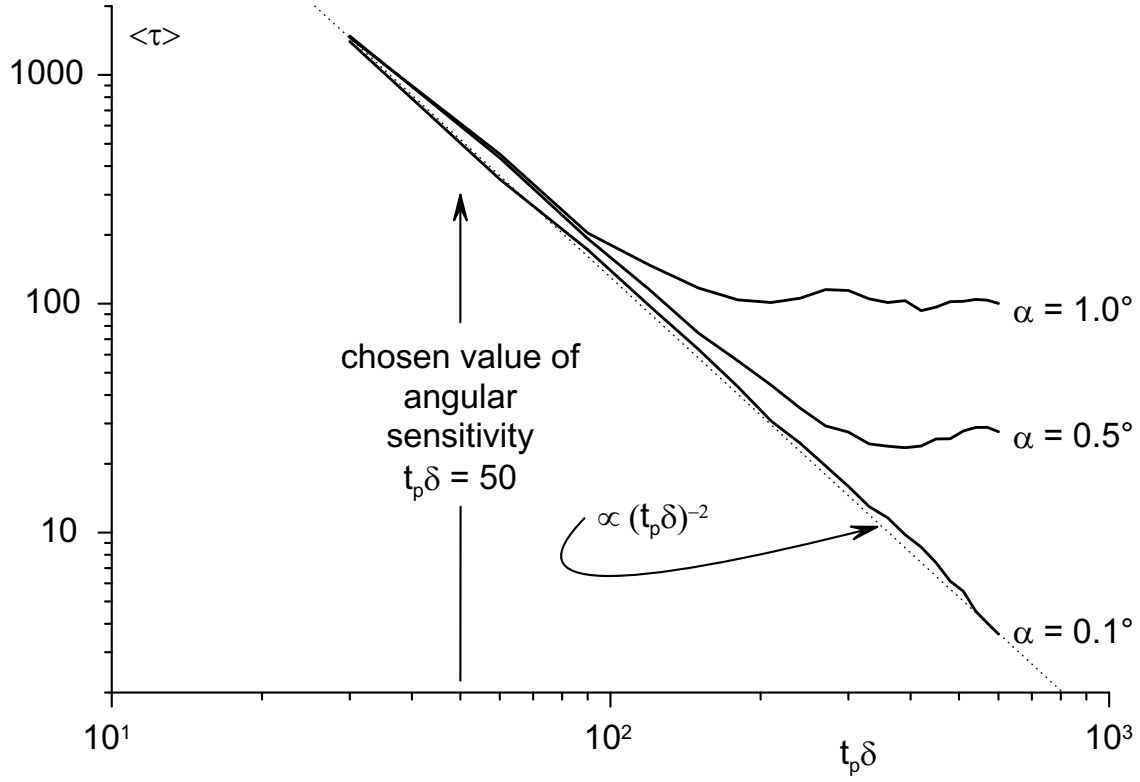

Figure 3.3: Test whether the emulation of diffusion by very-small-angle jumps is justified. Expected $(t_\mathrm{p}\delta)^{-2}$ dependence of $\langle\tau\rangle$ (dashed line) is found for 0.1° and 0.5°. Levelling off of 1.0°-jump simulation occurs close to the chosen angular sensitivity regime of $t_\mathrm{p}\delta = 50$.

using

$$\omega = \frac{\delta}{2}(3\cos^2\vartheta - 1 - \eta\sin^2\vartheta\cos 2\varphi) \tag{3.4}$$

and the currently valid tensor orientation, $[\theta, \phi]$, at the time of observation.

The initial orientation of the CSA tensor was randomly chosen, but the orientation changed over the course of the experiment due to successive rotational jumps according to the applied model (see below). By effecting a rotation about an angle α a change of orientation of the tensor orientation (x, y, z) to a new orientation (x', y', z') was achieved. Appendix A.1 gives the mathematical details and a sketch of the general jump process. Jump angles were 5°, 10°, or 20° for 'large'-angle jumps. Rotational diffusion was simulated using jumps of very small angles.

The value of angular sensitivity, which is related to the evolution time, was fixed to $t_\mathrm{p}\delta = 50$ for all simulations. For this chosen angular sensitivity, diffusional motion can be adequately approximated by 0.5° jumps occurring at every time step of the simulation.

This test is shown in Fig. 3.3. For diffusional motion one expects a proportionality between $\langle\tau\rangle$ and $(t_{\mathrm{p}}\delta)^{-2}$. This is indeed observed for jumps of a very small angle $\alpha = 0.1^\circ$. For $\alpha = 0.5^\circ$, $\tau(t_{\mathrm{p}}\delta)$ levels off at ca. 300. With an angular sensitivity of $t_{\mathrm{p}}\delta = 50$, a jump angle of 0.5° seems a reasonable compromise between sufficiently fast simulation and approximation of diffusion. For $\alpha = 1.0^\circ$, levelling off occurs too close to the chosen value of geometric sensitivity and was hence rejected as too coarse.

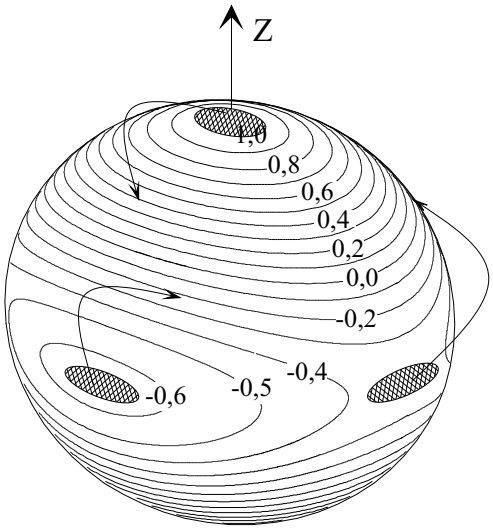

Figure 3.4: Equifrequency lines for the CSA tensor, asymmetry $\eta = 0.27$

Fig. 3.4 shows the variation of the NMR frequency (normalised to $\delta/2$) along the unit sphere for $\eta = 0.27$, the asymmetry parameter for the carboxyl carbon of PVAc. Note how the resonance frequence changes by different amounts depending on where on the unit sphere the jump occurs. For small-angle fluctuations close to the pole caps only minor frequency changes can be expected while the same fluctuations in the regions in between will result in a noticeable change of frequency. This will be further discussed below in the context of apparent heterogeneity.

The following three motional models were simulated in the course of this work:

(i) pure diffusion,

(ii) jump motion, and

(iii) superposition of diffusion and jump.

The used jump models are schematically visualised in Fig. 3.5. The ‘jump’ rate for diffusional motion for cases (i) and (iii) was one per unit time step. It is to be noted that this jump rate results in a diffusion constant of $D_{\mathrm{rot}} = \frac{\alpha^2}{4\tau} = 0.0625$. Jump motion for the two cases (ii) and (iii) was realised by a bimodal jump rate distribution with jump rates $k_{\mathrm{fast}} = 0.0625$, $k_{\mathrm{slow}} = 0.003125$, an exchange rate $\Gamma_{12} = 0.006$ and equal weight of slow

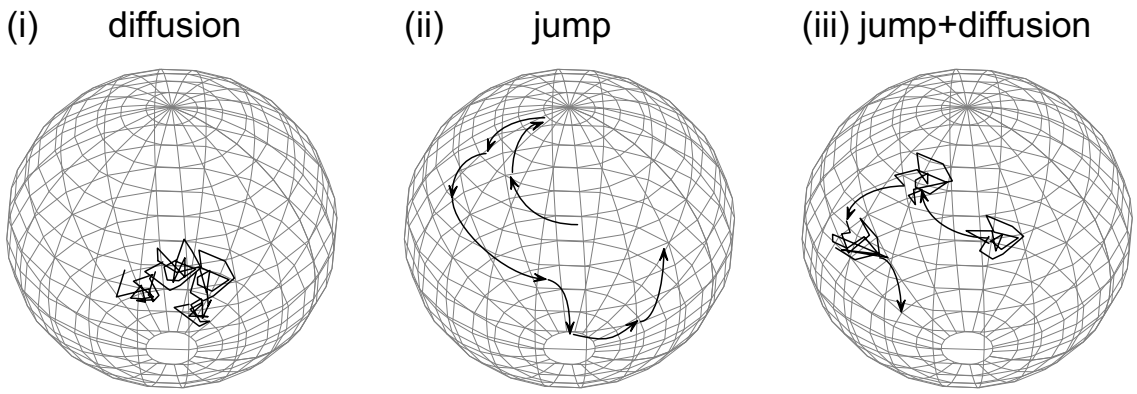

Figure 3.5: Three proposed models of motion: pure diffusion (i), jump motion about a fixed angle (ii), and superposition of diffusion and jump (iii).

and fast subsets. All rates are quoted as jump probabilities per unit time step. The same unit time step was used for the mixing time t_{m} in all displayed figures of this chapter.

3.3 Results

Fig. 3.6 shows a comparison of the two-time relaxation functions F_2 for all three models of motion. Jump angles of 10° for models (ii) and (iii) were used. As expected, if a particle can relax via combined diffusion and jump processes, one obtains the shortest decay time. As a rough approximation, the combined relaxation rate is the sum of the individual relaxation rates. Note that despite a constant rate for the diffusion (model (i)) a significant nonexponentiality can be observed.

In Fig. 3.7 the F_4 curves for the same three models are displayed. The value of the mixing time t_{m0} was chosen as the decay time τ_0 of F_2, defined via $F_2(\tau_0) = 1/e$. The efficiency of equilibration of relaxation rates, as expressed by the rate-memory parameter, Q, is very different for the two extreme models of pure jumps and pure diffusion. The case of pure jumps can be described by $Q = 1.5$. The latter result is in agreement with expectation, see above. One should note the small deviations of F_4 from the theoretical curve $F_4^{Q=1.5}$. These could be avoided when using the exact description of the rate memory with an infinite sum for F_4^Q rather than the approximation stated in Eq. 3.2 as discussed by Heuer [1997]. For the model of pure diffusion the rate-memory parameter turns out to be $Q = 18$. Strictly speaking, the rate-memory concept is not applicable

to pure diffusional motion. Rather, Q takes the function of an orientational memory as discussed further below. Nevertheless, the parameter Q can be understood as a phenomenological measure which – under the condition that rotational jumps occur – can be interpreted as rate memory. Sillescu [1996] discussed under what circumstances the the rate-memory parameter Q can be used as a measure of the memory of individual rates of molecular reorientation.

The large value of $Q = 18$ is in disagreement with the experimental results. Interestingly, the addition of jump processes with a jump angle of 10° gives rise to a dramatic increase of the exchange rate, Γ, compared to purely diffusive dynamics. This increased exchange leads to $Q = 4$.

Thus, the value of Q is strongly influenced by the nature of the jump motion. The presence of jump processes dramatically influences the relaxation function F_4 (Fig. 3.7)

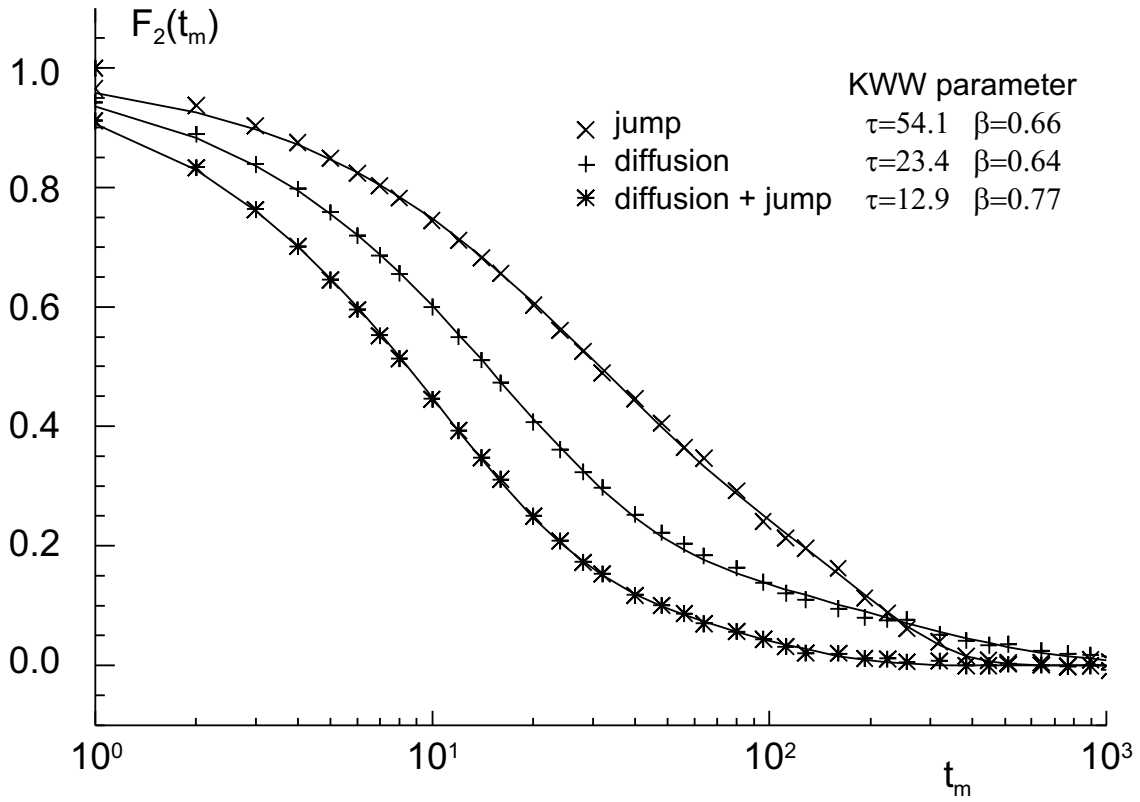

Figure 3.6: Relaxation functions F_2 as obtained from simulations. The three jump models are pure diffusion, pure jump motion and superposition of both as described in the text. The solid lines correspond to KWW fits (parameters given in the legend) of simulated data using Eq. 1.4. The fit results were the basis for the calculation of F_4^Q.

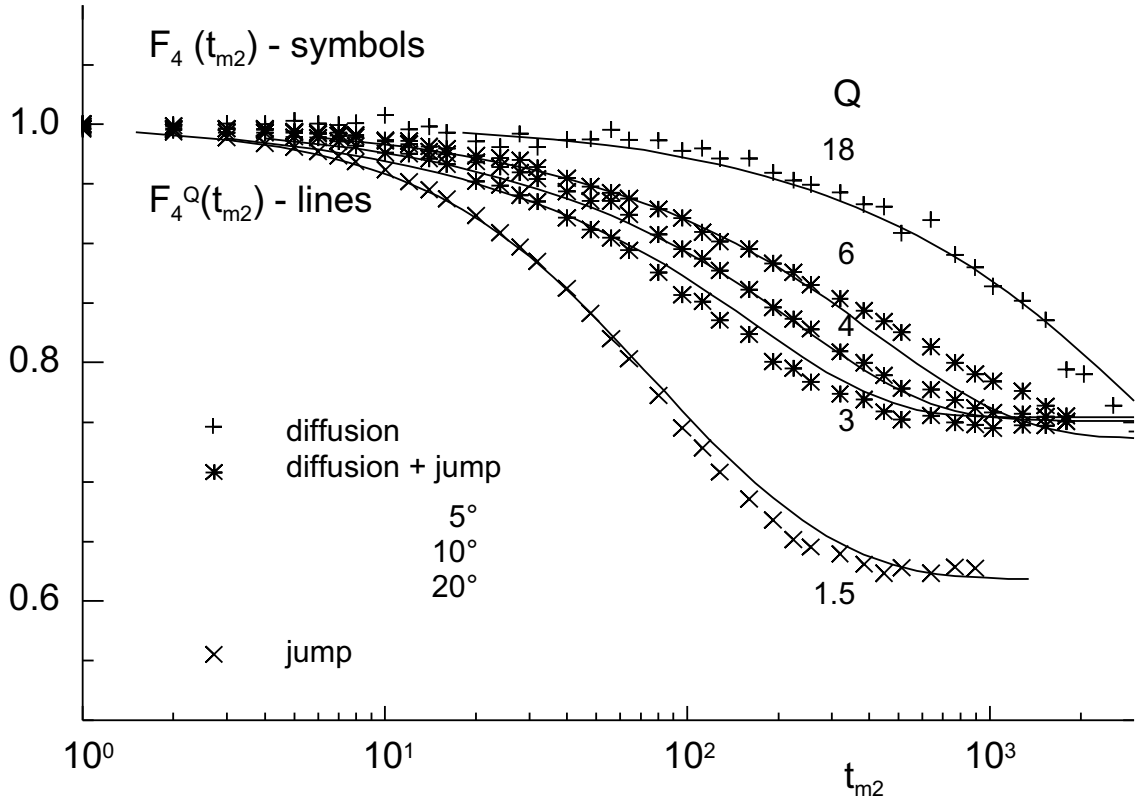

Figure 3.7: Relaxation functions F_4 corresponding to F_2 curves displayed in Fig. 3.6. The filter time t_{m0} was chosen such that $F_2(t_{\mathrm{m0}}) = 1/e$. Solid lines are theoretical functions $F_4^Q(t_{\mathrm{m2}})$ (cf. Eq. 3.2) based on $F_2(t_{\mathrm{m}})$ (cf. Fig. 3.6). For the jump model three different jump angles have been used.

whilst having only a marginal effect on the relaxation function F_2 (Fig. 3.6). To comprehend this phenomenon, one has to understand the exchange process monitored by F_4 and, at an even more fundamental level, the nature of the heterogeneity that manifested itself in the nonexponentiality of F_2 for the pure-diffusion model. Despite a constant jump rate and a constant angle for the diffusion process ($\equiv$ very small-angle jumps), F_2 is nonexponential. This can be understood by considering the nonlinear dependence of the resonance frequency, ω, on molecular orientation (see Eq. 3.4). As $\partial\omega/\partial\theta$ strongly depends on θ, the apparent diffusion constant, D_{a}, will vary with the orientation of the local molecular frame with respect to the external magnetic field. The apparent diffusion coefficient can be defined as

$$D_{\mathrm{a}} = \left(\frac{\partial\omega}{\partial\theta}\right)^2 + \left(\frac{\partial\omega}{\sin\theta\partial\phi}\right)^2 \tag{3.5}$$

Consequently, the exchange process detected by the relaxation function F_4 in the pure

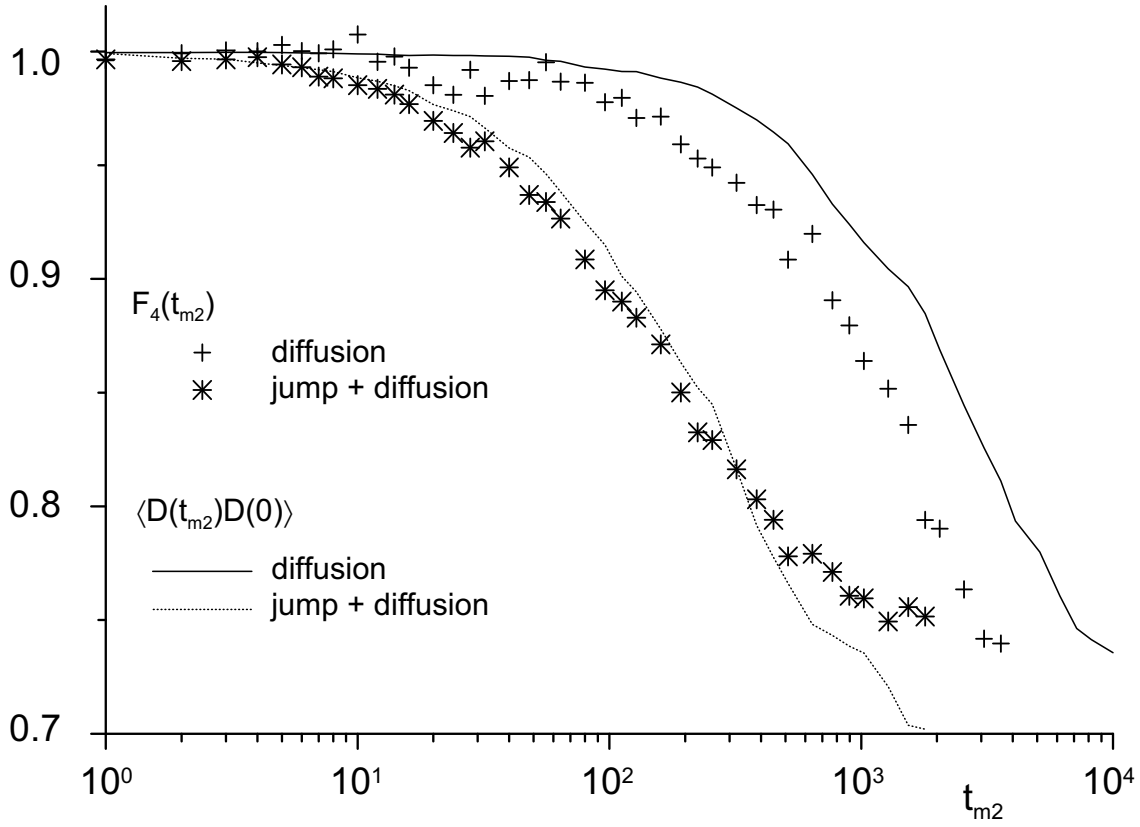

Figure 3.8: Relaxation functions F_4 for pure diffusion and for superposition of diffusion and 10° jumps together with the correlation function $\langle D_{\mathrm{a}}(t_{\mathrm{m2}})D_{\mathrm{a}}(0)\rangle$. The decay of $F_4(t_{\mathrm{m2}})$ and $\langle D_{\mathrm{a}}(t_{\mathrm{m2}})D_{\mathrm{a}}(0)\rangle$ occurs on the same time scale.

diffusion model must be the equilibration of the apparent diffusion constant, D_{a}. In order to check this conclusion, the decay of the correlation function $\langle D_{\mathrm{a}}(t)D_{\mathrm{a}}(0)\rangle$ has been compared to the decay of F_4. Fig. 3.8 reveals that the decay times of the four-time correlation function F_4 coincide with the decay times of the correlation function $\langle D_{\mathrm{a}}(t)D_{\mathrm{a}}(0)\rangle$ which describes the equilibration of the apparent diffusion constant.

Motivated by experimental NMR results, a variation of the selected subensemble was performed. The t_{m0}-dependence of F_4 was analysed for both the model of pure diffusion and for the model of superposition of diffusion and jump motion.

The results for $t_{\mathrm{m0}} = \tau_0$ and $t_{\mathrm{m0}} = 3\tau_0$ for the model containing the superimposed diffusion and 10° jumps are shown in Fig. 3.9. Interestingly, despite the considerable variation of the size of the selected subensemble reflected in the different degrees to which F_4 decays, the rate-memory parameter, Q, hardly changes upon variation of t_{m0}. This result has also been found in NMR experiments by Tracht et al. [1999a]. In contrast,

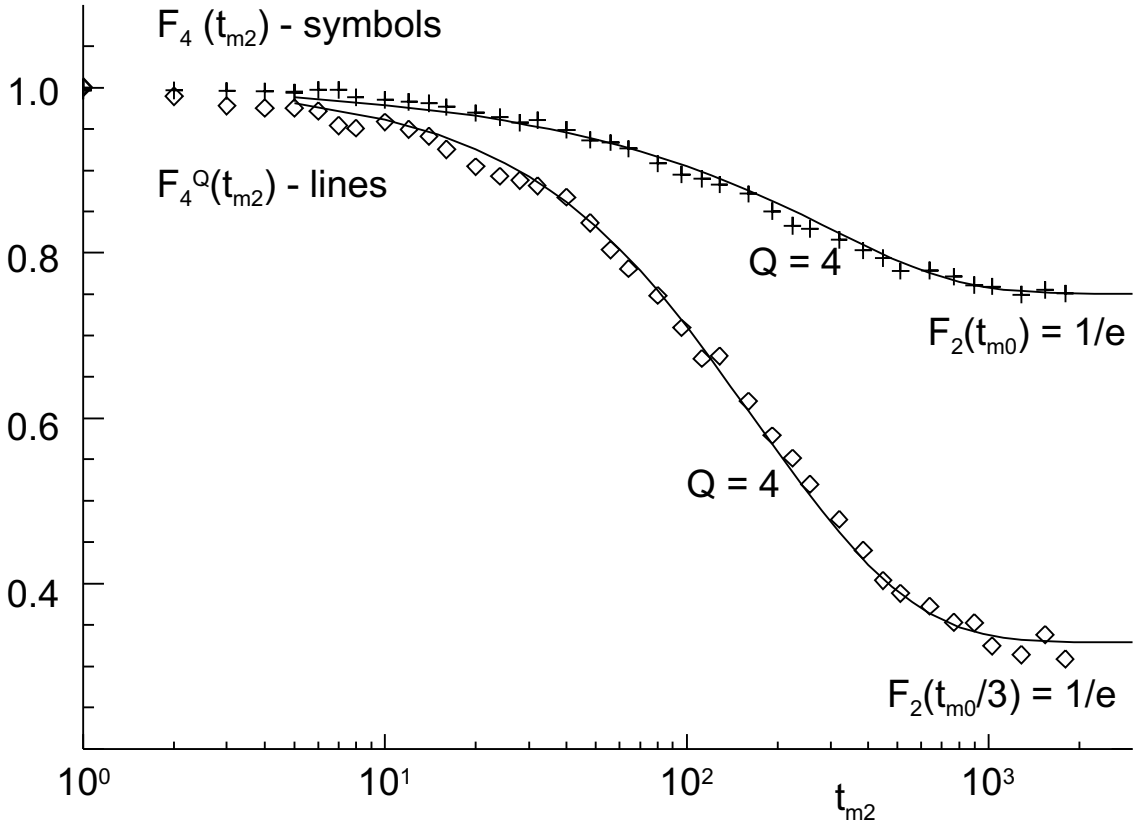

Figure 3.9: Relaxation functions F_4 for superposition of diffusion and jump motion. The filter time t_{m0} was set to τ_0 and $3\tau_0$, where $F_2(\tau_0) = 1/e$. Solid lines are theoretical functions $F_4^Q(t_{\mathrm{m2}})$ (cf. Eq. 3.2).

Q shows a strong dependence on the value of t_{m0} for a model of pure diffusion. This can be explained based on Eq. 3.3. The discussion of following the equation on page 43 alludes to the fact that under certain conditions the parameter, Q, depends on the size of the selected subensemble (i.e. depends on t_{m0}) in multistate systems. For the model of pure diffusion, this means that a larger t_{m0} results in particles with lower apparent diffusion coefficient, D_{a} (shaded areas in Fig. 3.4) and thus with a smaller 'jump' rate k_{s} being selected. An increase of t_{m0} (decrease of the subensemble size) will result in a decrease of Q. This corresponds to the self-evident statement that it takes less time for a tensor orientation to leave a small area of selection than it takes it to leave a larger area of selection.

A different picture arises if jump motion is added. Then, the rate of the slow subensemble, k_{s}, is limited at the lower end by the slowest jump rate. At sufficiently small subensemble sizes (the details such as the size of t_{m0} will depend on the model

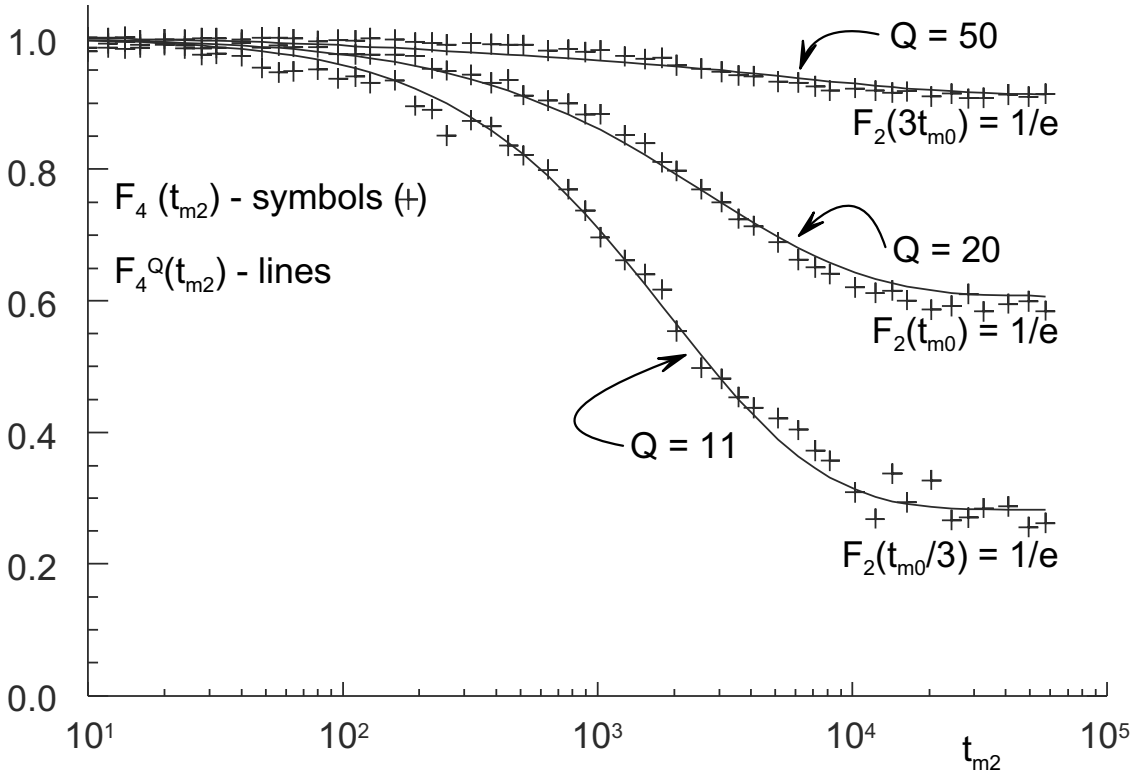

Figure 3.10: Relaxation functions F_4 for pure diffusion. The filter time t_{m0} was set to $\tau_0/3$, τ_0, and $3\tau_0$, where $F_2(\tau_0) = 1/e$. Solid lines are theoretical functions $F_4^Q(t_{\mathrm{m2}})$ (cf. Eq. 3.2). Notice the decrease of Q with increased filter time, t_{m0}.

parameters), k_{s} and therefore Q will not change any further. In other words, with a small enough area of selection, only one jump will move the tensor orientation from the region of selected low apparent diffusion to an unselected area.

In the present case, for $t_{\mathrm{m0}} \gtrapprox \tau_0$ no variation of Q is observed. This means that for a selection of roughly less than 32% already one single jump leads to the loss of memory.

3.4 Discussion and Conclusion

For all the different motional models (diffusion, bimodal jumps, and superposition of both), nonexponential relaxation was observed. In experiments it has been shown that heterogeneities are the underlying reason for this nonexponential behaviour. The nature of this heterogeneity can, however, be different. The purpose of performing the simulations is to study the importance of certain types of heterogeneity. Furthermore, the simulations help drawing conclusions about the geometry of the motional processes in

PVAc from 4D echo experiments. These conclusions agree with findings from an earlier, conceptually different approach of Tracht et al. [1999b].

The most obvious scenario as a reason for the observed heterogeneity in the case of large-angle jumps is a distribution of jump rates. This was replicated in the simulations by a bimodal rate distribution for the model of jump motion. One could envisage the existence of rapidly and slowly diffusing molecules as the reason for heterogeneities being observed in purely diffusive dynamics. While shown in colloid systems, this cannot be true for the presented simulations. Despite a uniform diffusion constant in the presented simulations, nonexponential relaxation was still evident in Fig. 3.6. This can only be understood by invoking the concept of the so-called apparent heterogeneity. By recognising that the apparent diffusion coefficient (see Eq. 3.5) depends on the orientation of the CSA tensor with respect to the external magnetic field, one understands the exponent of the KWW decay of $\beta \approx 0.6 \neq 1$.

We have discussed the various forms of heterogeneity that are observed in NMR experimental data and simulations. However, the simulations (Fig. 3.6) show that the two-time correlation function $F_2(t_\mathrm{m})$ is only mildly influenced by the different jump models. The difference becomes strikingly obvious in the four-time correlation function F_4. While diffusional motion results in considerably higher Q parameters, the addition of jump motion by about 10° dramatically reduces Q. As we observed in NMR experiments a rate memory close to the minimum rate memory ($Q \approx 1$), we can positively assert the presence of large-angle jumps in PVAc.

Comparison of the apparent diffusion coefficient's auto-correlation function with the four-time correlation function (Fig. 3.8) showed that they both decayed on the same time scale. This observation proves that the extraordinarily large Q parameters in the case of pure diffusion are due to a slow exchange process, an equilibration, of the apparent diffusion coefficient. One should remember that the parameter Q is a phenomenological measure that serves as a rate-memory measure in the case of rotational multimodal jump motion. The addition of jumps to the diffusion decreases the memory of D_a in accordance with a reduction of Q for the superposition model.

The variation of the dependence of Q on the portion of the selected subensemble fur-

ther corroborates the notion of a superposition of jump and diffusional motion. Varying t_{m2} and with it the portion of the sample that gets labelled as slow leaves the rate memory unchanged for the jump+diffusion model. For pure diffusion, Q is calculated in a range of 10 to 50 for the selection levels studied. This can be understood based on the approximation for Q given in Eq. 3.3.

The geometry of rotational motion in the glass former PVAc is in harmony with earlier analysis by two-dimensional NMR by Tracht et al. [1999b]. Two conceptually different approaches (the 2D and 4D echo experiments) in conjunction with simulations, lead to the picture of diffusional motion with additional large-angle jumps.

Chapter 4

Theory and Simulation of Spin Diffusion in Glass Formers

Computer simulations provide a link between models, theoretical predictions, and experiments: When compared to real experiments, computer experiments serve as a test for the model underlying the simulation process. If the model turns out to behave as expected, simulations can provide insight to the experimentalist and might assist in the interpretation of experimental results. To help in the interpretation of data obtained from the length-scale NMR experiment, simulations of the spin diffusion process were carried out on hard-sphere systems.

The question of the length scales in glass formers is, as pointed out in the introduction, a long-standing issue of debate for the glass-research community. Unfortunately, a variety of definitions of a length scale make straightforward comparison of results from different types of experiments difficult. The obvious advantage of simulating hard-sphere systems is that all microscopic information is retrievable. In particular, the length scale obtained by means of a pseudo NMR experiment can directly be compared with other definitions of a length scale. Moreover, the data-analysis procedure of the length-scale NMR experiment can be validated.

This chapter deals with the theoretical background of the 4D3CP experiment. Its foundation on the well-established formalism of diffusion is briefly portrayed. From this formalism one can derive ways of analysing as well as simulating the NMR experiments.

This is discussed in detail and backed by studies on hard-sphere systems.

4.1 How to Describe Spin Diffusion

Before we turn our attention to the algorithm used, let us now briefly sketch the formal description of diffusion tailored to the simulation. The following equation is a solution of the general differential diffusion equation $\frac{\partial}{\partial t}M = D\ \nabla^2 M$ in three dimensions.

$$M(\mathbf{r},t) = \frac{M_0}{(4\pi Dt)^{3/2}}\,\mathbf{e}^{-\frac{\mathbf{r}^2}{4Dt}} \tag{4.1}$$

$M(\mathbf{r},t)$ represents the magnetisation diffusing from a point source located at $\mathbf{r}=0$ at time $t=0$. Due to the normalisation, the overall diffusing magnetisation, $\int \mathrm{d}\mathbf{r}\, M(\mathbf{r},t)$, is constant and equals M_0 at all times, t. Note that at $t=0$ there is an unphysical δ distribution of magnetisation at $\mathbf{r}=0$.

Accordingly, we consider more realistic initial conditions as encountered in the data analysis of the simulation or of the 4D3CP NMR experiment. In the case of the 4D3CP experiment, magnetisation after the second cross-polarisation step (details see Section 5.1.1 on p. 75) can be visualised as 'spread out' over the protons in the vicinity of the originally slow ^{13}C. Thus motivated, let us imagine that instead of an initial magnetisation confined to $\mathbf{r}=0$ the starting magnetisation $M_0(\mathbf{r})$ is spread out as given by a Gaussian distribution with a width a according to:

$$M_0(\mathbf{r}) = \frac{M_0}{(2\pi a^2)^{3/2}}\,\mathbf{e}^{-\frac{\mathbf{r}^2}{2a^2}} \tag{4.2}$$

A δ distribution, the starting condition that leads to the diffusion solution of a point source (Eq. 4.1), is contained in the magnetisation density given in Eq. 4.2 in the form of the limit: $\lim_{a\to 0} M_0(\mathbf{r})$. Due to the linear nature of the diffusion equation, the magnetisation at position $\mathbf{r}_0$ at times $t>0$ can be determined from a superposition of diffusion processes originating in a point source (see Eq. 4.1). The terms of the diffusion processes are weighted with the appropriate $\mathbf{r}$-dependent factor as given in Eq. 4.2.

$$M_{\text{point}}(\mathbf{r}_0,t) = \int \mathrm{d}\mathbf{r}\ \frac{\mathbf{e}^{-\frac{\mathbf{r}^2}{2a^2}}}{(2\pi a^2)^{3/2}} M(\mathbf{r}-\mathbf{r}_0,t) = \frac{M_0}{(2\pi(a^2+2Dt))^{3/2}}\mathbf{e}^{-\frac{\mathbf{r}_0^2}{2a^2+4Dt}} \tag{4.3}$$

Eq. 4.3 shows how general initial conditions $M_0(\mathbf{r})$ can be treated. For the specific case of $M_0(\mathbf{r})$ as given by Eq. 4.2, one can see how the initial spread a translates into a shift in time by t_0 according to $a^2 = 2Dt_0$ (compare Eq. 4.1 and Eq. 4.3).

In the 4D3CP experiment, magnetisation is initially located only at places of *selected* particles. This selection happens by means of a dynamic filter in the NMR experiment. For the simulation we are free to choose a suitable selection criterion for setting the starting magnetisation. This initial condition of several (vs. just one) magnetisation sources can conveniently be described by a suitably chosen $M_0(\mathbf{r})$ or, as detailed below, by directly utilising the solution obtained in Eq. 4.3.

Additionally, a second (identical) selection has to happen in the 4D3CP experiment so that only the magnetisation left at the initially selected subensemble is measured. This means that the total detected magnetisation is the sum over the magnetisation experienced at all of the *selected* sites. It will be shown that an average initial density can be used instead of the summation over all *selected* particles. To show the equivalency, we consider the total detected magnetisation M_{detect} where an integration over all selected regions as well as an integration over all diffusion starting locations is performed:

$$M_{\text{detect}}(t) = \frac{1}{N} \int \mathrm{d}\mathbf{x}\ \rho(\mathbf{x}) \int \mathrm{d}\mathbf{y}\ \rho(\mathbf{y}) M_{\text{point}}(\mathbf{x}-\mathbf{y}, t). \tag{4.4}$$

Here, $\rho(\mathbf{x}) = \sum_i \delta(\mathbf{x}-\mathbf{r}_{\text{i}})$ signifies a density function that chooses only magnetisation at selected locations. Equally, we use the same function $\rho(\mathbf{y})$ for the second integral because diffusion starts from the locations defined by the same criterion (in the 4D3CP experiment utilising the same filter, see following chapter). The total magnetisation detected at all selected locations $\{\mathbf{r}_{\text{i}}\}$ can then be rewritten from the last Eq. 4.4. If we perform the double integration over $\mathbf{x}$ and $\mathbf{y}$ we arrive at the following sum:

$$M_{\text{detect}}(t) = \frac{1}{N} \sum_{\text{i,j}} M_{\text{point}}(\mathbf{r}_{\text{i}} - \mathbf{r}_{\text{j}}, t). \tag{4.5}$$

As this expression only depends on differences $\mathbf{r}_{\text{i}} - \mathbf{r}_{\text{j}}$, one can rewrite it in terms of a sum over probabilities $p_{\text{i}}(\mathbf{z})$ for finding a particle at distance $\mathbf{z} = \mathbf{r}_{\text{i}} - \mathbf{r}_{\text{j}}$ from a starting

point $\mathbf{r}_\mathrm{i}$:

$$\begin{aligned} M_{\text{detect}}(t) =& \frac{1}{N}\sum_i \int \mathrm{d}\mathbf{z}\; p_\mathrm{i}(\mathbf{z}) M_{\text{point}}(\mathbf{z},t) \\ =& \int \mathrm{d}\mathbf{z}\; \overline{p}(\mathbf{z}) M_{\text{point}}(\mathbf{z},t) \\ =& \int_0^\infty \mathrm{d}r\; \hat{p}(r) M_{\text{point}}(r,t) \end{aligned} \tag{4.6}$$

This sequence of equations shows how one can transform the dependence of $M_{\text{detect}}(t)$ on a vector-dependent distance probability, $\overline{p}(\mathbf{z})$, to a distance-dependent probability $\hat{p}(r)$.[1]

Eq. 4.6 equips us with a tool to simulate and analyse spin diffusion. On the one hand, a particular $\hat{p}(r)$ along with some parameters of $M_{\text{point}}(r,t)$ fully determine the behaviour of $M_{\text{detect}}(t)$. Hence, one only needs to find a suitable $\hat{p}(r)$ from the system under study to simulate diffusion. On the other hand, if measured $M_{\text{detect}}(t)$ data is available, on can, in principle, determine the pair-correlation function. In practice, this is done by guessing a reasonable $\hat{p}(r)$ and fitting the parameters which describe its final shape.

Fig. 4.1 shows four different functions $\hat{p}(r)$. The first two, a) and b), are convenient approximations used for data analysis and program testing. Whereas c) and d) are measured on a hard-sphere system and MD simulation data of glycerol, respectively. Of course, functions $\hat{p}(r)$ will approximately be proportional to $4\pi\rho r^2$ which is why $\hat{p}(r)$ has been normalised to $4\pi\rho r^2$ to better show the deviation from the r^2 dependence at shorter radii.

One should point out that the model describing the 4D3CP experiment is further complicated by taking into account (i) a time-dependent density of slow regions and (ii) the effect of cross-polarisation. Both are described in detail in the appendix of Tracht et al. [1998]. A solution that makes the diffusion equation more amenable to being treated numerically is given in section 4.3 (Eqs. 4.10-4.13).

[1] The case of constant density for calculating the mass of a sphere, V, exemplifies this transformation: $\overline{p}(\mathbf{z}) = \rho = \text{const.} \curvearrowright m = \int_V \mathrm{d}\mathbf{z}\; \overline{p}(\mathbf{z}) = V \cdot \rho$. This corresponds to $\hat{p}(r = |\mathbf{z}|) = 4\pi r^2 \cdot \rho$ which leads to $m = \int_0^R \mathrm{d}r\; \hat{p}(r) = \frac{4}{3}\pi R^3 \cdot \rho = V \cdot \rho$.

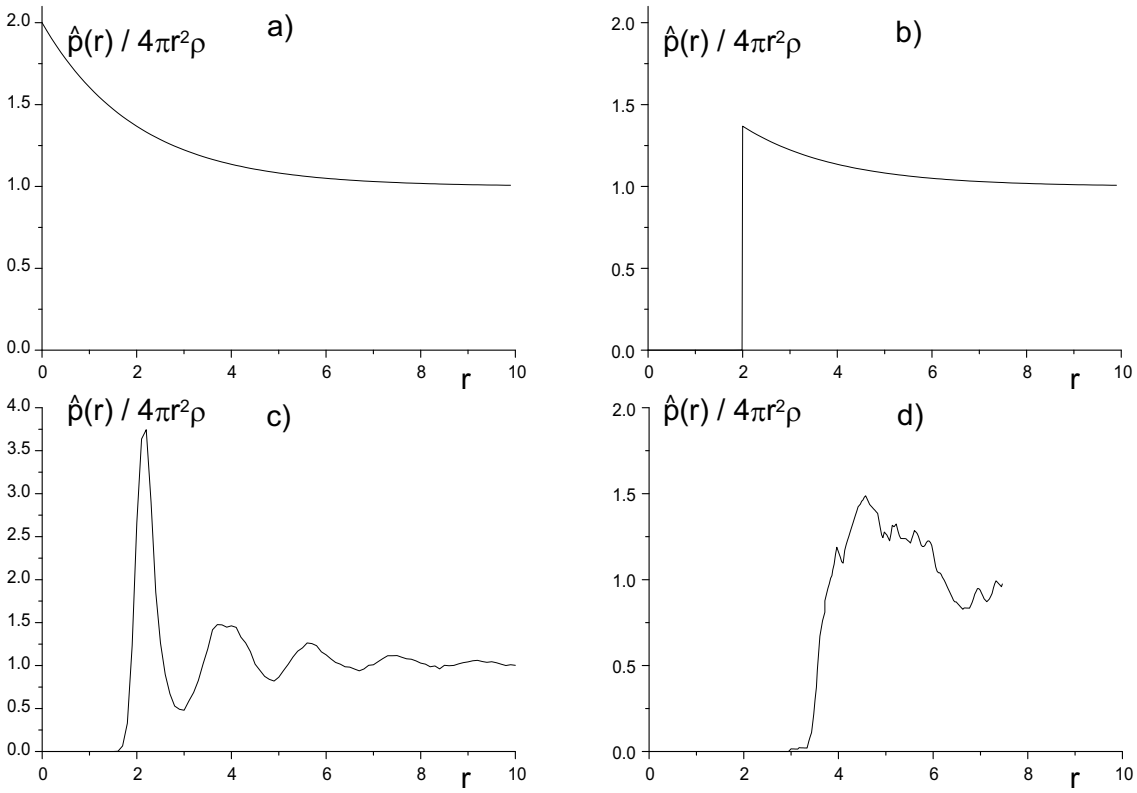

Figure 4.1: Distribution functions $g(r) = \frac{\hat{p}(r)}{4\pi\rho r^2}$ that are the basis for calculating magnetisation decays $M(t_{\mathrm{m}})$. a) simplest form used in the conventional analysis procedure, b) modified form featuring a gap, g, c) measured pair-correlation function for a system of hard spheres, d) pair-correlation function for carbon atoms in glycerol, reproduced from Root and Stillinger [1989]

4.2 Simulation of Spin Diffusion

The diffusion experiment on a hard-sphere system consists, quite analogously to the 4D3CP experiment, of (i) a subensemble selection based on a criterion of free choice, (ii) a diffusion process, and (iii) a measurement of the magnetisation remaining at locations of the initially selected subensemble. As outlined in the previous section, once a selection criterion is translated into the corresponding pair-correlation function, the diffusion process is fully described.

Before turning to the matter of selection criteria, the systems under study will be briefly described. It is desirable to have a well-equilibrated system that exhibits the features, particularly of dynamic heterogeneities, in supercooled liquids. At the same time, one desires a system that is big enough to avoid the influence of finite-size effects. In a study by Doliwa and Heuer [2000] three-dimensional hard-sphere systems were ex-

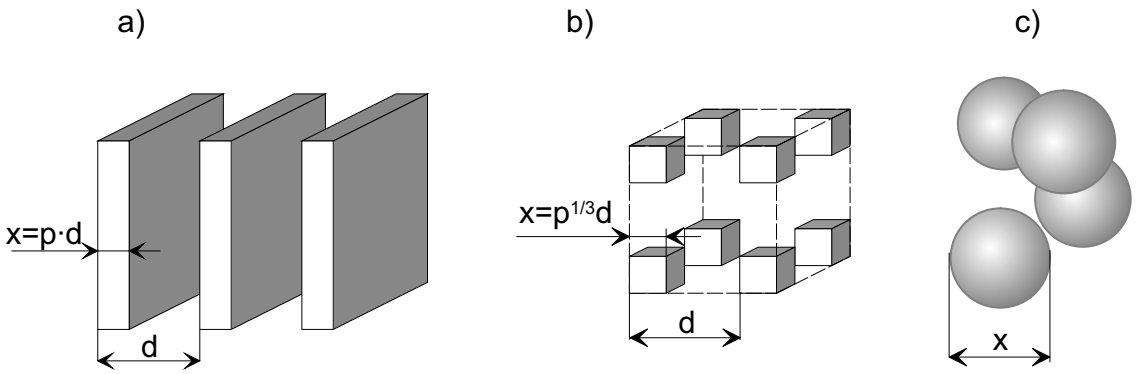

Figure 4.2: Topologies used for 'artificial' selection criteria: Particles were defined as *slow* if they happened to reside in periodically positioned lamellae (a), cubes (b), or randomly placed spheres (c). x is the geometric parameter that serves as a measure for the smallest dimension of the heterogeneity under question.

tensively investigated. These systems proved to be the ideal candidates for the above reasons. More specifically, two systems were investigated: The denser system comprises 16307 particles ($\rho = 0.56$), while the less dense ($\equiv$'hotter') system consists of 15422 particles ($\rho = 0.53$) both in a box of the size $(50R_0)^3$. In other words, this is a cube with dimension 25 mean particle diameters (given an average particle radius of 1). Doliwa and Heuer [2000] described the details of the simulation and provide the system configurations which are used in the present study.

Initially, somewhat artificial selection criteria were attempted: Hard spheres inside boxes, spheres, or lamellae of well-defined sizes were said to be 'slow'. Fig. 4.2 sketches the used topologies and introduces the geometric parameter, x. Ideally, the fit procedure should reproduce the size of those heterogeneities. Note that the repeat length, d, of periodic structures and the geometry parameter, x, determines the number of selected particles. The ratio is $p = \frac{x}{d}$ for lamellae and $p = \frac{x^3}{d^3}$ for cubes. For the spheres, the ratio depends in a less-straightforward fashion on radius, r, and number, N, of spheres.

To take the selection one step further, one considers fast and slow particles in a more realistic sense. Particles that have experienced fewer than a certain number of nearest-neighbour (NN) changes[2] over a given time are considered 'slow'. This criterion mimics quite well the selection of slow particles. Fig. 4.3 shows one such scenario. For purposes

[2]A change of nearest neighbours constitutes the leaving of one adjacent sphere in exchange for the arrival of another sphere in the neighbour shell of a particle under consideration

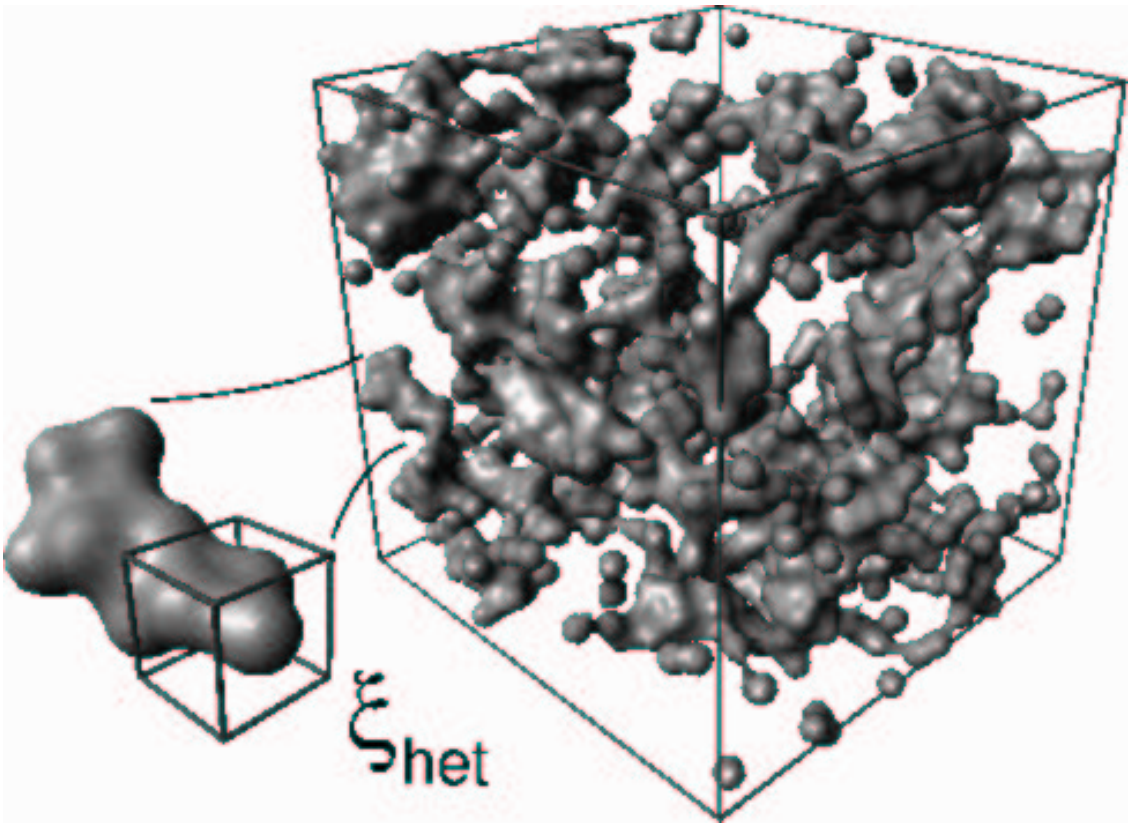

Figure 4.3: Slow hard spheres. Particles that experienced fewer than five changes of nearest neighbours are enveloped by a surface while fast particles not displayed. The inset shows an enlarged slow domain with the scale of fitted heterogeneity indicated.

of clarity, only spheres that are considered slow by this criterion are displayed while fast particles are not shown. Surface are shown enveloping regions of slow mobility.

Once a selection criterion was identified, histograms of particles labelled as 'slow' yielded pair-correlation functions similar to the ones displayed in Fig. 4.1c. For better statistics, they were averaged over a number of configurations. Using

$$M(t) = \int_0^R \mathrm{d}r \frac{1}{(4\pi Dt)^{3/2}} \exp(-\frac{r^2}{4Dt}) \quad p(r), \tag{4.7}$$

and a time offset of $t = t_0 + t_m$ (cf. Eqs. 4.3 and 4.6) resulted in magnetisation-decay curves similar to the ones shown in Fig. 4.4. This was done for a variety of selection scenarios and selection levels, p, the results of which are discussed below.

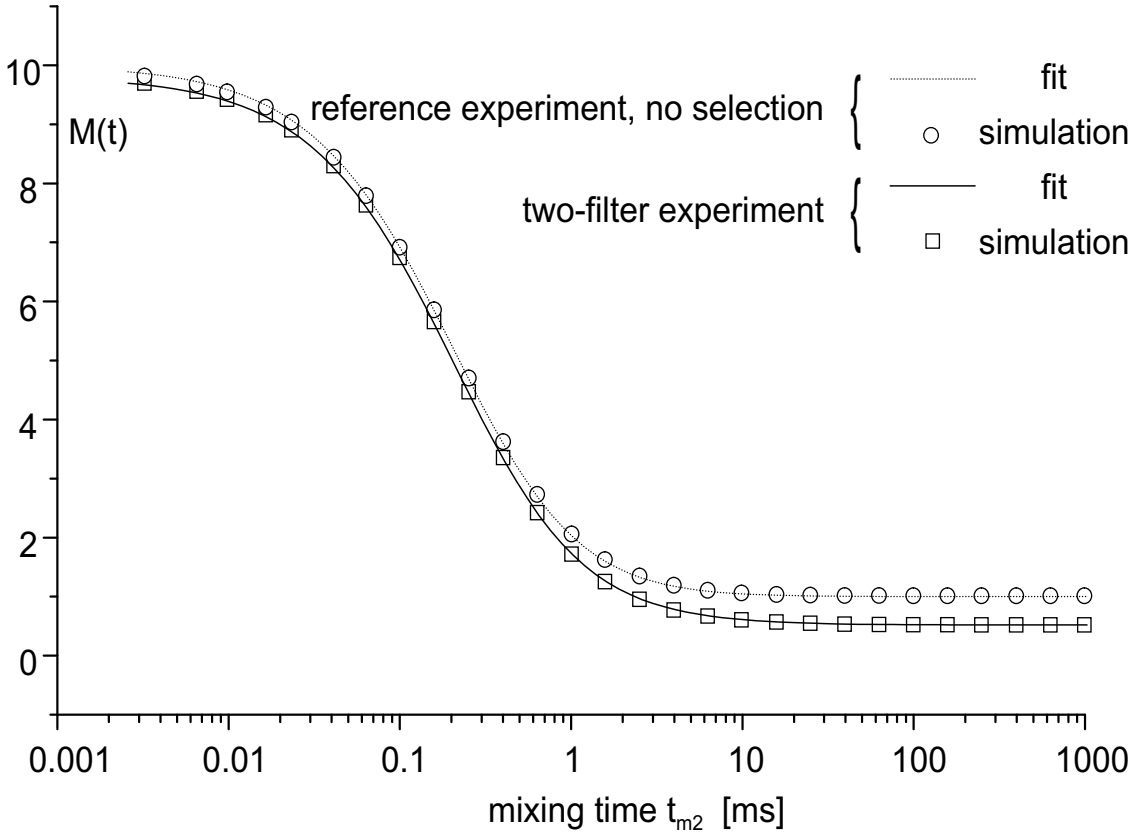

Figure 4.4: Magnetisation decay for 10% randomly labelled sample (circles). This corresponds to the reference experiment and yields the diffusion constant. Also shown (squares) is the magnetisation decay in an ensemble selected according to the Voronoi criterion (corresponding to particles with less than five nearest-neighbour changes within a time span of four τ_α). The best fits as obtained from the model are shown as solid lines.

4.3 Data Analysis of Spin-Diffusion Experiments

At first, the fit procedure introduced by Tracht et al. [1998] was used to fit the magnetisation curves obtained from heterogeneities in the shape of lamellae, cubes, or spheres. Fig. 4.5a shows fits of length scales, ξ_{het}, resulting from fits based on the pair-correlation function as shown in Fig. 4.1a. The value ξ_{het} shows a significant offset from the chosen geometric parameter (lamellae thickness, box side length, or sphere diameter) for small ξ_{het}.

This incongruity can be rationalised as follows: Although the exponential form of the pair-correlation function as plotted in Fig. 4.1a is a reasonable assumption it will certainly not be true for small $|\mathbf{r}|$. This can easily be concluded from looking at pair-correlation function 4.1c measured for the hard-sphere systems under study. A good 'second-order'

approximation would have to include a *gap* around the origin $\mathbf{r} = 0$ (see Fig. 4.1b). Accounting for the gap, which corresponds to roughly twice the minimal particle radius, would rectify the above-described discrepancy. Hence, the spatial extent of the slow regions would take the form of

$$p(\mathbf{r}_{ij}) = \begin{cases} \delta(\mathbf{r}_{ij}) & : |\mathbf{r}_{ij}| \leq g \\ \xi_0^{-3}(p + (1-p)\mathrm{e}^{(-\frac{2|\mathbf{r}_{ij}|}{\xi_{\mathrm{het}}})}) & : |\mathbf{r}_{ij}| > g \end{cases} , \tag{4.8}$$

where p represents the fraction of molecules designated as slow and g is the gap around a particle that can not be entered by neighbours. The average ^{13}C density is reflected in the parameter ξ_0^{-3}. Note that as g approaches 0 the above relationship represents the pair-correlation function as given by Eq. [4] in Tracht et al. [1998]. Naturally, one has to determine a reasonable parameter for the gap size, g. By fitting reference diffusion curves, it was found that the gap has to be smaller than the centre distance of two nearest neighbours, r_{NN}. The exponential approximation (Eq. 4.8) best accounts for the deviation from the real pair-correlation function (as shown, e.g., in Fig. 4.1c) if a gap of $g = \frac{3}{5} r_{\mathrm{NN}}$ is used. As nearest-neighbour distances, r_{NN}, of glycerol and OTP are available from MD simulations in the literature, we will later make use of this empirical finding (Sections 5.2 and 5.3).

Fig. 4.5b shows how the improved procedure yields values for ξ_{het} that match the ge-

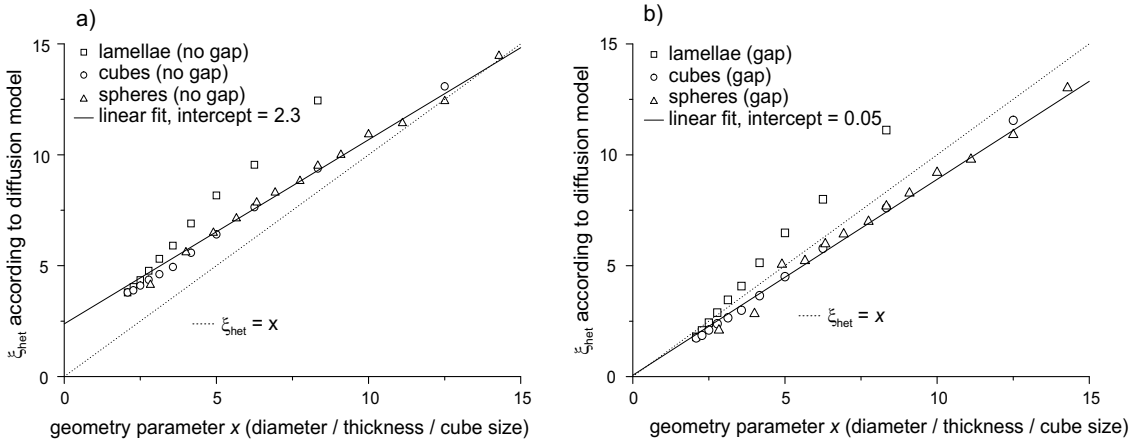

Figure 4.5: Fitted values of ξ_{het} vs. the geometry parameter d (lamellae thickness, sphere diameter, cube side length). The left plot (a) shows fits using a continuous exponential decay (cf. Fig. 4.1a). The right plot (b) shows fits obtained with a magnetisation distribution that accounts for a region that is 'forbidden' for nearest neighbours(cf. Fig. 4.1b). The dashed line indicates the ideal 1:1 relationship between geometric parameter and measured heterogeneity.

ometric input parameters, x. It is noteworthy that ξ_{het} has to be plotted against diameters (spheres) or side length (cubes) in order for ξ_{het} to directly represent the geometry parameter. This motivated the particular decay constant, $\xi_{\text{het}}/2$, in Eq. 4.8. One can also see that structures that are heterogeneous in all three dimensions (i.e. spheres, cubes) give nearly the expected 1:1 relationship between ξ_{het} and d whereas one-dimensional heterogeneities (lamellae) deviate from the expected curve $\xi_{\text{het}} = x$.

Before the seemingly improved model is applied, some attention shall be given to its interior function. Substituting the proposed pair-correlation function in Eq. 4.8 for the one given by Tracht et al. [1998] the complete integral changes to

$$\begin{aligned} F_4^{\xi}(t_{\text{m2}}) =& \frac{1}{(4\pi D t_{\text{eff}})^{3/2}} \int_0^{\infty} \mathbf{e}^{(-\frac{\mathbf{r}^2}{4Dt_{\text{eff}}})} \times \\ & \Big[\mathbf{e}^{-\frac{\mathbf{r}^2}{2a^2}} F_4(t_{\text{m2}}) + \frac{1}{\xi_0^3} \int_g^{\infty} \mathbf{e}^{-\frac{(\mathbf{r}-\mathbf{r}_{\text{c}})^2}{2a^2}} \big(p + (1-p)\mathbf{e}^{-\frac{2|\mathbf{r}_{\text{c}}|}{\xi_{\text{het}}}} y(t_{\text{m2}})\big) d\mathbf{r}_{\text{c}}\Big] d\mathbf{r}. \end{aligned} \tag{4.9}$$

$F_4(t_{\text{m2}})$ describes rate exchange as investigated in Chapter 3. It can be safely assumed that $F_4(t_{\text{m2}}) = 1$ for our hard-sphere systems because we deal with dynamic heterogeneities that are static on the time scale of observation. Note that the lower limit of the second integral over $\mathbf{r}_{\text{c}}$ in Eq. 4.9 changed from 0[Tracht et al., 1998] to g. This will render a convenient integration over $\mathbb{R}$ impossible. Nevertheless, by substitution and partial integration[3] one arrives at the following solution that can still be used in a fit procedure without the use of costly numerical integration.

Integral 4.9 simplifies into three summands of the form

$$A = \frac{1}{(1+\frac{2Dt}{a^2})^{\frac{3}{2}}} F_4(t), \tag{4.10}$$

$$B = p\frac{a^3}{\xi_0^3}\Big(2\pi g\, \mathbf{e}^{\frac{g^2}{2a^2+4Dt}} (2a^2+4Dt)^{-\frac{1}{2}} + (2\pi)^{\frac{3}{2}} \text{erfc}\,(\frac{g}{\sqrt{2a^2+4Dt}})\Big), \tag{4.11}$$

$$C = \frac{1}{(1+\frac{2Dt}{a^2})^{\frac{3}{2}}} \frac{1-p}{\xi_0^3}\, y(t)\, 4\pi \int_g^{\infty} r^2 \exp\Big(-\frac{r^2}{2a^2+4Dt} - \frac{r}{\xi_{\text{het}}/2}\Big)\, dr\ . \tag{4.12}$$

Substituting $\alpha = 2a^2 + 4Dt$ and $\beta = \xi_{\text{het}}/2$ and performing the integration, Eq. 4.12 can

[3]Note that straightforward but tedious integration eliminates most of the integrals. Consider $\int_0^{\infty} e^{-ar^2}\, dr = \frac{\sqrt{\pi}}{2\sqrt{a}}$, and $\int_{\mathbb{R}^3} e^{-a\vec{r}^2}\, d\vec{r} = 4\pi \int_0^{\infty} r^2 e^{-ar^2}\, dr = (\frac{\sqrt{\pi}}{a})^{3/2}$.

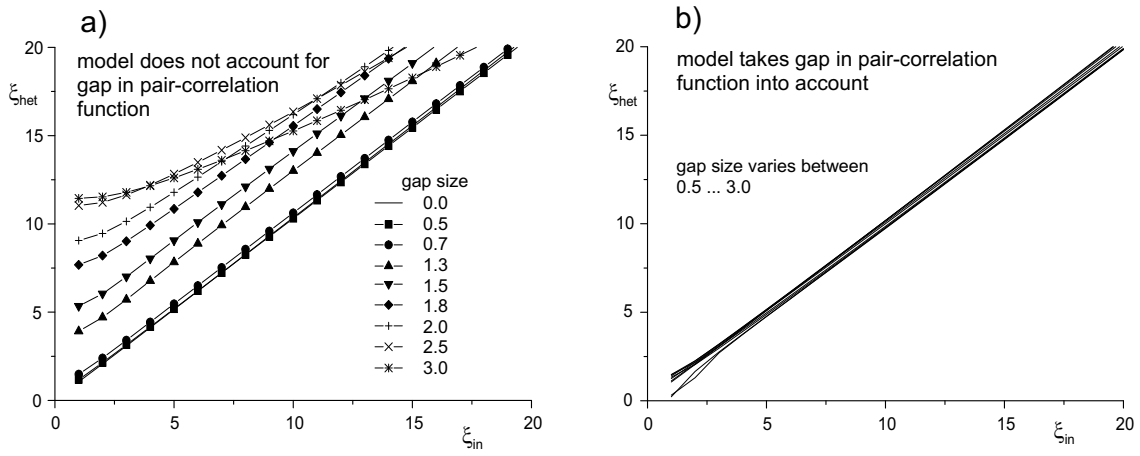

Figure 4.6: Fitted values of ξ_{het} vs. the value of ξ_{in} that was input into the pair-correlation function $p(r) = p + (1-p)\mathbf{e}^{-2r/\xi_{\text{in}}}$ for $r > g$ and $p(r) = 0$ for $r \leq g$. While the conventional fit procedure (a) fails to reproduce the input heterogeneity length scale, ξ_{in}, the modified analysis scheme (b) obeys the desirable relationship $\xi_{\text{het}} = \xi_{\text{in}}$.

be rewritten as

$$C = \frac{1}{(1+\frac{2Dt}{a^2})^{\frac{3}{2}}} \frac{1-p}{\xi_0^3} y(t) 4\pi \left[\frac{\sqrt{\alpha\pi}}{2} \mathbf{e}^{\frac{\alpha}{4\beta^2}} \left(\frac{a^2}{4\beta^2} + \frac{\alpha}{2} \right) \operatorname{erfc}\left(\frac{g}{\sqrt{\alpha}} + \frac{\sqrt{\alpha}}{2\beta} \right) + \left(\frac{1}{2} g\alpha - \frac{\alpha^2}{4\beta} \right) \left(1 - \mathbf{e}^{\frac{g^2}{\alpha} - \frac{g}{\beta}} \right) \right] . \tag{4.13}$$

Hereby $\operatorname{erfc}(x)$ denotes the complimentary error function

$$\operatorname{erfc}(x) = 1 - \operatorname{erf}(x) = 1 - \frac{2}{\sqrt{\pi}} \int_0^x e^{-t^2}\, dt, \tag{4.14}$$

which is part of the C-library `math.h` functions and proved to speed up the evaluation of the integral by a factor of ca. 1900 as compared to numerical integration.

The function $F_4^{\xi}(t) = A + B + C$ is used for the curves without selection by setting $p = 1$ and for the curves with selection by choosing the appropriate value for p, ($0 < p < 1$).

A good test for the correctness of Eqs. 4.10 to 4.13 would be to attempt fitting a synthetic function $\hat{p}(r)$ where all shape-determining parameters are known. The result of such a test is shown in Fig. 4.6. The modified fit procedure reproduces all input parameters (diffusion constant, D, initial magnetisation spread, a, gap size, g. Fig. 4.6b shows how the heterogeneity length scale, ξ_{het}, is recovered by the improved model. However, the conventional method has to compromise between a better fit and a larger

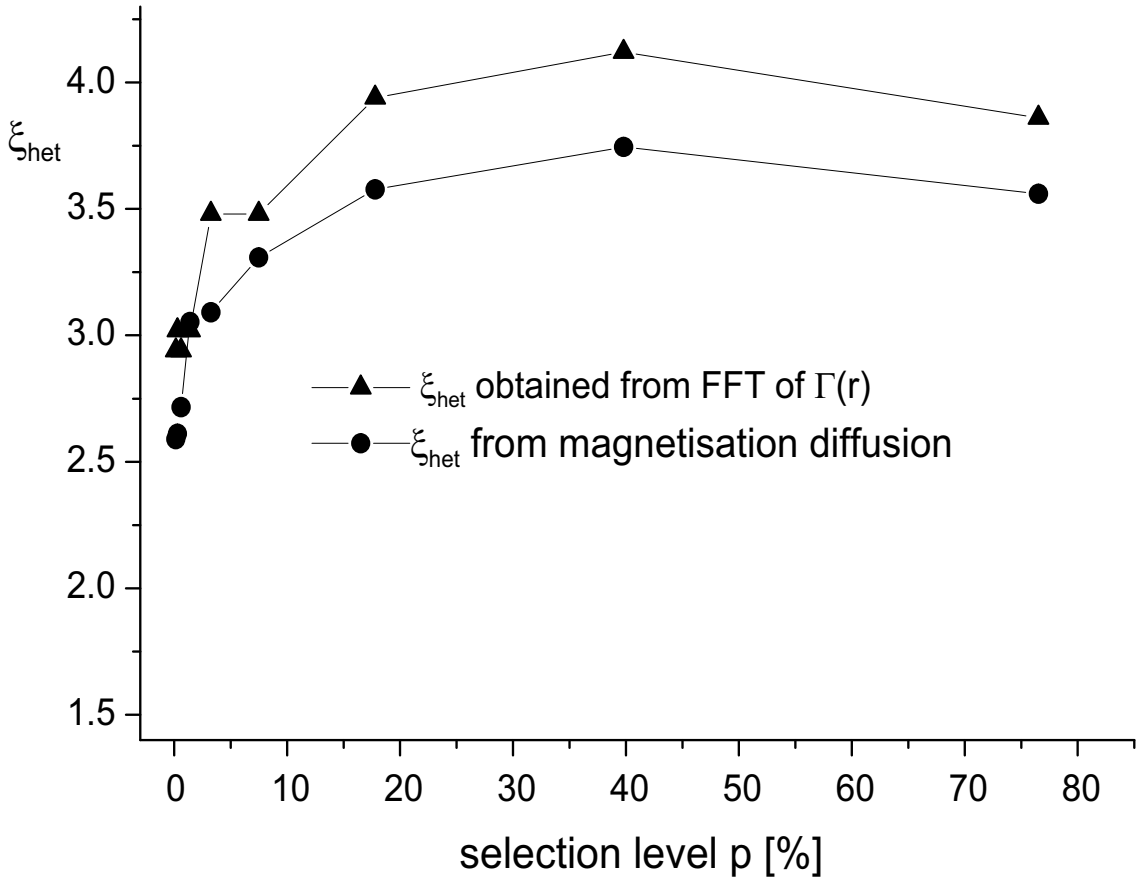

Figure 4.7: Fitted values of ξ_{het} vs. selection level, p. Fits were obtained from diffusion simulation (spheres) and fitting a Lorentz function to the Fourier transformation of the normalised pair-correlation function. Details see text.

diffusion constant (30% in the case of $g = 3.0$) in combination with an offset ξ_{het} (cf. Fig. 4.6a).

4.4 Results

The results from studying 'artificial' heterogeneities were – if not surprising – at least helpful in calibrating the fit procedures and in convincing ourselves to trust this method of data extraction. Thus equipped, we can now investigate dynamic heterogeneities of the previously described type. Fig. 4.3 depicts what dynamic heterogeneities as defined by the NN-change criterion look like. As a reminder, particles are considered 'slow' if they have experienced less than five changes of nearest neighbours in a given time period, t_{wait}. Particle selection was performed with waiting time varying between τ_α and $9\tau_\alpha$. For

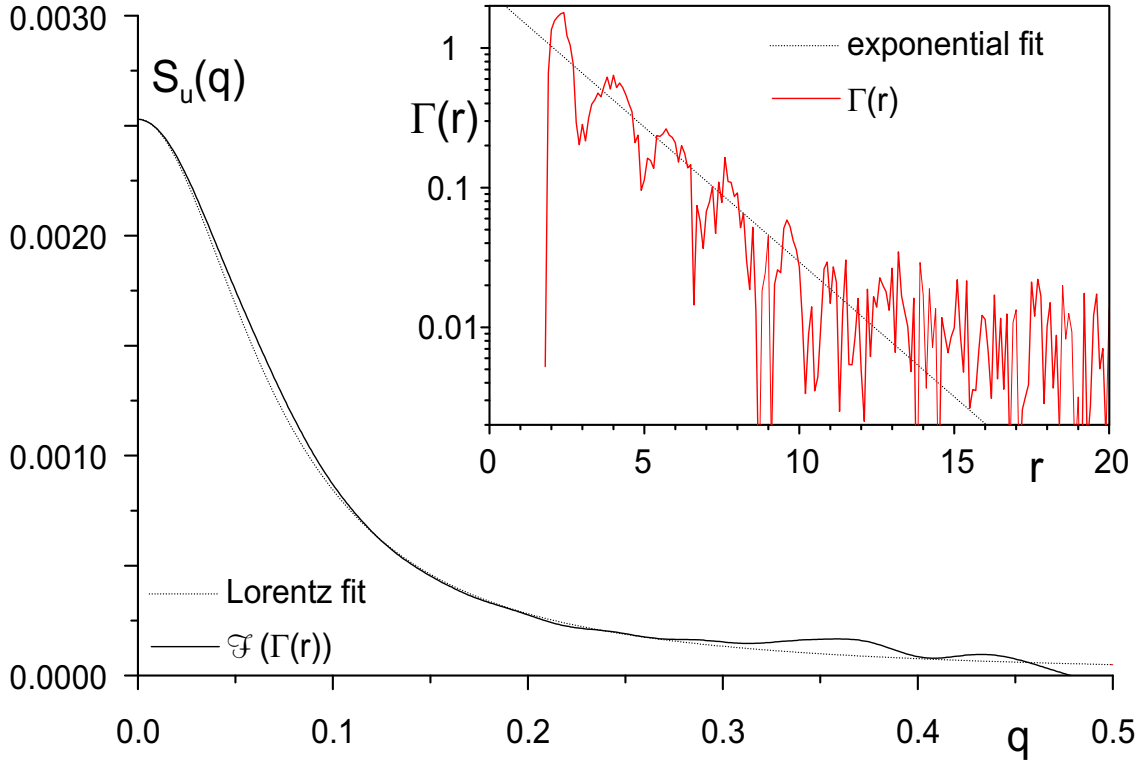

Figure 4.8: Fourier transform of $\Gamma(r)$ (see text) for illustration of alternative means for length-scale determination. The inset shows $\Gamma(r)$ and the corresponding Lorentz fit. HS system ($\rho = 0.53$), slow $\equiv$ fewer than five NN changes in $2\tau_\alpha$, $\xi_{\text{het}} = 4.12$

the system with $\rho = 0.53$ (15422 particles), this resulted in 76% of the total ensemble being selected as slow. The selection level decreased down to 0.1% for a waiting time $t_{\text{wait}} = 9\tau_\alpha$. Due to the drastic change of selection, we can thus measure the heterogeneity length scale of subensembles representing different portions of the entire sample. As expected, Fig. 4.7 shows that the length scale, ξ_{het}, increases when the selection level, p, is increased. However, ξ_{het} quickly levels off at about 30%.

The beauty of performing this experiment in hard-sphere systems is that one can check the result by directly measuring the length scale in the sample by other means. The normalised pair-correlation function $\Gamma(r) = p_{\text{sub}}(r)/p_{\text{total}}(r) - \rho_{\text{total}}/\rho_{\text{sub}}$ is a measure of the degree to which a selected subensemble ($p_{\text{sub}}(r)$) deviates from a homogeneous sample ($p_{\text{total}}(r)$). In the literature, two equivalent ways of extracting the length scale from $\Gamma(r)$ are given. Doliwa and Heuer [2000] fitted an exponential to the decaying function which yielded ξ_{het} as the decay constant. However, the procedure previously applied by Donati et al. [1999] was favoured in the present study: The 'structure factor',

$S_{\mathrm{u}}(q)$, is calculated from the the Fourier transform $S_{\mathrm{u}}(q) = \mathcal{F}(\Gamma(r))$. The principal equivalence of fitting to the Fourier transform or to the exponential is obvious from:

$$\mathcal{F}\left(\mathrm{e}^{-\frac{2r}{\xi_{\mathrm{het}}}}\right) = \int_0^\infty \mathrm{d}r\ \exp(-iq - 2/\xi_{\mathrm{het}}) \quad \propto \quad \frac{1}{1 + q^2(\frac{\xi_{\mathrm{het}}}{2})^2} \tag{4.15}$$

However, just as many NMR spectroscopists prefer to draw conclusions from spectra rather than FIDs it is preferable in the present case to choose the reciprocal-space representation for data analysis because the parameter ξ_{het} can be fitted with greater accuracy. Fig. 4.8 shows both the structure factor and its Fourier transform with respective fits using the same parameter ξ_{het}. One of the curves in Fig. 4.7 is a plot of the length scale obtained from Fourier transforms of $\Gamma(r)$. It closely follows the other curve, that was obtained from diffusion simulations. This further corroborates the validity of the developed analysis procedure. The small difference between ξ_{het} determined from FT and the one originating from spin-diffusion simulation is explicable in the light of the discussion of the pair-correlation function underlying the diffusion process: The 'gap' pair-correlation function is nonetheless – even though a manifestly good – approximation of the real underlying function. Subsequently, the insignificant differences in ξ_{het} have substantiated the adoption of the spin-diffusion ξ_{het} values.

Of course, it would be highly desirable to learn something about the shape of the domains under scrutiny. In principle, such information could be gathered from selection level-dependent determination of ξ_{het}. In fact, this seems feasible for the hard-sphere system. One could imagine that the presence of a (fixed) number of slow domains with a diffusion gradient from the core to the surface would, upon increased selection, p, exhibit an increase in length scale, ξ_{het}. This is not the case as can be seen in Fig. 4.7. Quantitatively, one could say that, above 30% selection, slow domains do not simply increase by scaling their size. Instead, they grow dendritic-like sprouts which leads to the characteristic length scale being *constant* at ca. 3.5. As desirable as a similar statement would be for 'real' glass formers, it is not likely that one can find definite clues about the shape of heterogeneous domains from NMR data due to the scatter and scarcity of experimental data.

4.5 Conclusion

In summary, the simulations of diffusion in hard-sphere as well as continuous-medium systems strongly support the data-analysis method applied to extract a heterogeneity length scale from experimental NMR data. If one assumes artificial heterogeneous regions in the shape of, e.g., spheres, we find that the heterogeneous length scale exactly matches the geometric parameter, e.g., sphere diameter, in a 1:1 relationship. Heterogeneous structures of such regular (spheric, cubic, lamellar) shape will not be found in a dynamically heterogeneous sample such as the subensemble in a hard-sphere system that shows fewer than average nearest-neighbour changes. Nevertheless, a length scale can be attributed to such likely fractal structures by means of the diffusion experiment as well as analysis the static 'structure factor'. Values of ξ_{het} obtained either way match. From studies on lamellae we learn that ξ_{het} represents something like the 'smallest' dimension of a heterogeneity. Furthermore, a modification of the analysis procedure to include a gap, g, around the origin of magnetisation spread explains diffusion data on model systems in a superior way.

Chapter 5

Length-Scale Experiments

The length scale of cooperativity is one of the remaining unsolved – or at least heatedly debated – issues of glass-transition research. The importance of this type of length scale was stressed in the introductory Section 1.1. As pointed out, the ambiguity when comparing the obtained results is partly due to differing definitions of this length scale. A very practical viewpoint stems from the answer to the fundamental question of whether relaxation in glass formers is heterogeneous or homogeneous [Böhmer et al., 1998a]. The ability of an experimental technique to perform a selection of a subensemble (e.g., based on a relaxation rate that is more or less constant throughout this subensemble), proves the heterogenous nature of relaxation in glass formers. This was shown to be true for PVAc by Schmidt-Rohr and Spiess [1991]. Length scales describing domains using their method of selection are the subject of the present chapter. Other attempts to determine ξ_{het} [Li et al., 1989; Heuer et al., 1995; Arndt et al., 1996; Korus et al., 1997] exist but make various assumptions. All these attempts are indirect estimates of the length scale.

The breakthrough in direct measurement of the dynamic-heterogeneity length scale came recently with a multi-dimensional solid-state NMR experiment introduced by Tracht et al. [1998]. The concept of combining the following two aspects in one multi-dimensional NMR experiment has been discussed in the literature by Tracht et al. [1999c]. The experiment makes use of the fact that the NMR frequency can monitor the *orientation* of the molecular unit under investigation. Furthermore, the length scale of regions which differ in their dynamic characteristics (in our case, correlation times

of rotational motion) can be measured using spin diffusion [Schmidt-Rohr and Spiess, 1994; Abragam, 1961].

A number of questions can be addressed with the experiment at hand. It is not clear whether ξ_{het} should be similar for polymers, low molecular weight glass formers, fragile, or strong glasses. Comparing measurements to both simulation and theory can be more directly done if simple systems are studied. Furthermore, no experimental information has been available on the temperature dependence of a directly determined ξ_{het}. Theoretical estimates predict how fragility influences cooperativity [Erwin and Colby, 2001] but these predictions could neither be verified nor falsified.

Given the above guidelines, two low molecular weight glass formers, glycerol and *o*-terphenyl(OTP), have been chosen for length-scale studies to provide possible answers to the above questions. Glycerol is a model low molecular weight glass former which has been investigated by numerous techniques such as two-dimensional ^{2}H NMR [Böhmer and Hinze, 1998], broad-band dielectric spectroscopy [Arndt et al., 1996], non-resonant dielectric hole burning [Schiener et al., 1997], and heat-capacity spectroscopy [Korus et al., 1997]. While the geometry and time development of the dynamics are well understood, no direct measurement of the heterogeneity length scale has been presented. In this chapter, the determination of ξ_{het} for glycerol from $T_{\text{g}}+10$ K to $T_{\text{g}}+18$ K is reported. OTP is one of the most widely studied glass formers. Various techniques such as homodyne light-beating spectroscopy [Fytas et al., 1981], ^{2}H NMR [Dries et al., 1988; Geil et al., 1998; Böhmer et al., 1998b; Stumber et al., 2001], photobleaching techniques [Cicerone et al., 1995b; Cicerone and Ediger, 1995], and heat-capacity spectroscopy [Donth et al., 2001] were utilised to investigate *o*-terphenyl.

In this chapter a short introduction to the experimental and analytical techniques used is given. This is followed by a discussion of the actual NMR experiment performed on glycerol and *o*-terphenyl. A method for estimating statistical errors is presented and the influence of inefficient filters on the obtained results is considered. Finally, conclusions are drawn from the length-scale measurements in the context of proposed theories of supercooled liquids and other experiments that measure heterogeneous length scales.

5.1 Experimental Technique

5.1.1 The 4D3CP experiment

Cross polarisation, dynamic filters, spin-lock and z filters, and spin-diffusion measurements are discussed in the introductory Section 1.3. We shall now briefly assemble these building blocks to form the reduced four-dimensional spin-diffusion NMR experiment by Tracht et al. [1998]. Fig. 5.1 shows the pulse sequence of the 4D3CP experiment, the integral part of which is the selection of a slow subensemble by means of a dynamic filter. After the first dynamic filter (b) and before the second cross polarisation, magnetisation is left only at places of molecules or polymer segments that have reoriented an unusually small amount in a given time period, $t_{\mathrm{m1}} =: t_{\mathrm{m0}}$. Two measures were taken to assure that no magnetisation remains in the proton spin bath. First, during a carbon spin lock, proton magnetisation is flipped back to the +z axis prior to a delay during which decay of transverse ^{1}H magnetisation occurs (b). Second, a ^{13}C z-filter stores the filtered magnetisation (just before the cross polarisation back to the proton spin bath) whilst waiting for any proton coherence to decay (c). After the second cross polarisation and a ^{1}H spin-lock period, we are left with magnetisation at protons within or in direct vicinity of slow domains. To avoid excessive ^{1}H spin diffusion in the rotating frame before a sufficient magnetisation

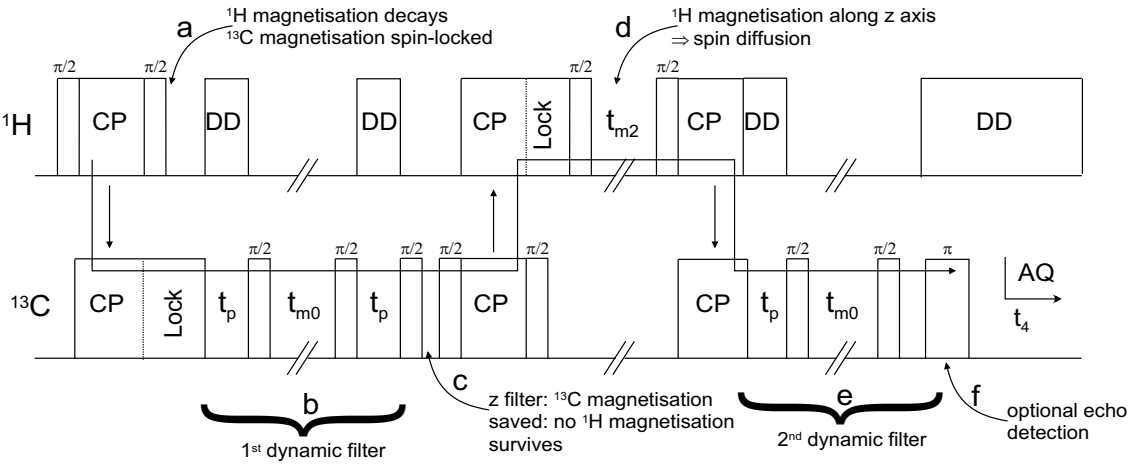

Figure 5.1: Pulse sequence for the (reduced) four-dimensional spin-diffusion exchange experiment (4D3CP); $t_{\mathrm{m1}} = t_{\mathrm{m3}} =: t_{\mathrm{m0}}$ is set to select an adjustable portion of the slow ensemble while t_{m2} is incremented to monitor the spin diffusion starting from slow domains into the whole sample.

transfer occurs, it is desirable to choose short cross-polarisation and spin-lock times; this favours protonated carbons, which are under investigation. The monitoring magnetisation redistribution starting from centres of low mobility throughout the entire sample, the core of the 4D3CP experiment, is facilitated by aligning magnetisation along the $\pm$z axis and allowing spin diffusion to occur (d). After the spin-diffusion stage, magnetisation is again transferred back to the carbon spin bath. This step causes the bulk of the signal to be lost because magnetisation located at protons will find only very few carbons nearby that can receive magnetisation during the following short CP contact time. This third transfer is nonetheless necessary because only with the final dynamic filter (e) can one selectively interrogate (f) sites of slow mobility (just as was done at the outset of the pulse sequence).

Given the design of the pulse sequence, one can fortunately calibrate constants (most of all, the spin-diffusion coefficient) needed for extracting a length scale internally. This can be done by completely deactivating the two dynamic filters thus suppressing any sensitivity to dynamical processes in the supercooled liquid. If filter times t_{m1} and t_{m3}, or evolution times $t_1 = t_2 = t_3 = t_4 = t_{\mathrm{p}}$ are set to their minimum, no dynamic selection would happen. Instead, we would find that, after the second cross polarisation, protons in proximity to all ^{13}C would be polarised. Spin diffusion and subsequent monitoring of magnetisation remaining in the catchment area of ^{13}C atoms by short cross polarisation would yield information about the diffusion coefficient, D, and the initial magnetisation spread prior to the diffusion stage, a. The magnetisation thus measured at various times t_{m2} serves as a so-called reference.

With the information gathered from the reference experiment, one can proceed to perform the actual length-scale measurements with the tunable dynamic filters ‘switched on’. After various times t_{m2}, ^{13}C spins are monitored to determine if the diffused magnetisation is still associated with slow units; at sufficiently long times, the magnetisation of ^{13}C spins are found on sites whose dynamics are characteristic of the entire ensemble.Given the time required for the magnetisation to leave the slow subensemble, the heterogeneity length scale can be calculated using the independent measurement of the spin diffusion coefficient as described above.

5.1.2 Relaxation Agents

Low molecular weight glass formers close to the glass transition pose a challenge to the experimentalist in that they exhibit exceptionally long spin-lattice relaxation times, T_1, of up to several minutes. An approach often taken in solution-state NMR is the addition of a relaxation agent containing a paramagnetic ion, e.g. Cu^{2+}. For our experiments, the substance must naturally be compatible with the glass under investigation. Foremost it must dissolve properly in the glass former. In the present case, $CuNO_3$ and $Cu(acac)_3$ were used for glycerol and for *o*-terphenyl, respectively, as relaxation agents (cf. Chapter 2).

An experiment was designed to confirm that the presence of ca. 0.1 wt% [1] or less of this relaxation agent does not influence the heterogeneous behaviour of the supercooled liquid. This experiment allows the selective measurement of the two-time relaxation

[1]This concentration corresponds to ca. one Cu^{2+} ion every 10 glycerol molecules.

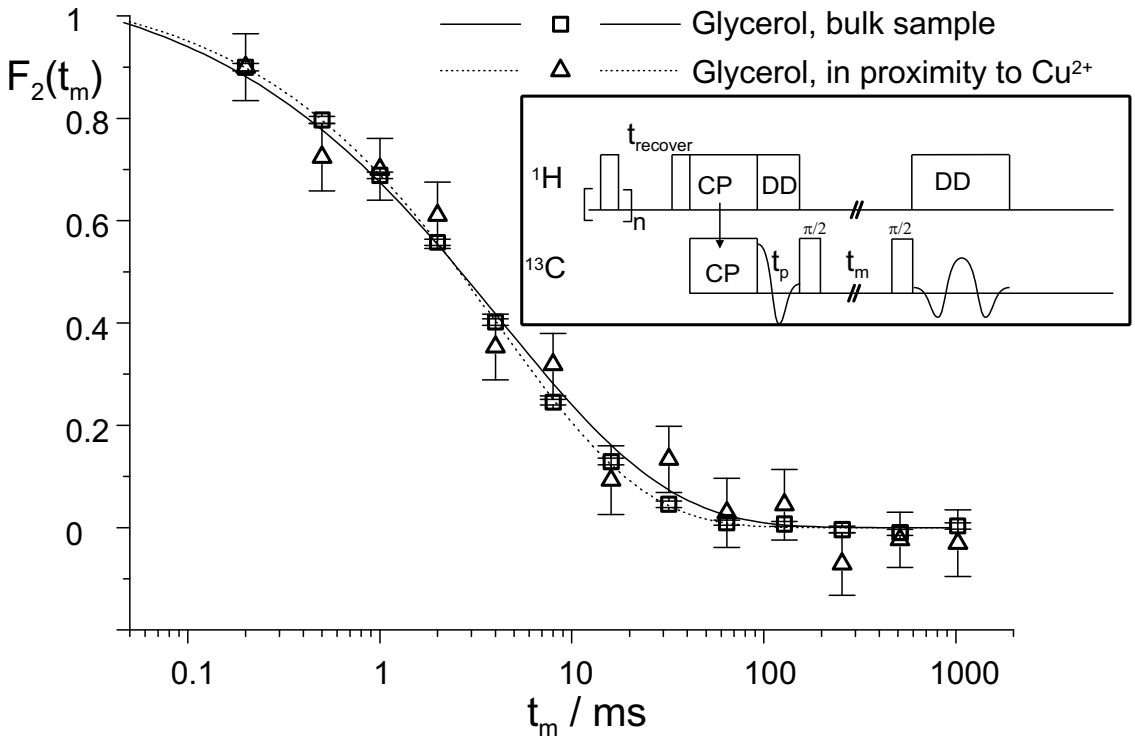

Figure 5.2: Two-time correlation function $F_2(t_\mathrm{m})$ with and without saturation pulses before a 2D echo experiment ($t_\mathrm{p}\delta = 9.9$). The close agreement indicates that the spin relaxation agent does not perturb orientational dynamics in glycerol. The inset shows the applied pulse sequence with $n = 0$ (bulk 2D echo) and $n = 10$ (selective 2D echo). Error bars: smaller than symbol size (bulk sample), in agreement with fits (selective 2D echo)

function of molecules that would be most influenced by the introduced impurity. The resulting dynamic relaxation response can be then compared to that of the bulk sample. The mechanism of spin-lattice relaxation is crucial for the success of the experiment. Proton spins further from the Cu centres relax at their inherent T_1-relaxation rate. Protons in proximity to Cu^{2+} ions relax significantly more quickly. An averaged spin-lattice relaxation time is then achieved due to efficient spin diffusion between protons.

The feature of the experiment is to apply a series of saturation pulses to the protons. After a very short delay ($t_{\text{recover}} \approx 1$ ms), only protons close to Cu^{2+} will have relaxed at which point a standard two-time correlation experiment is carried out. Fig. 5.2 shows the comparison of the two-time correlation function $F_2(t_{\text{m}})$ for the bulk glycerol and for glycerol close to Cu centres. The inset in Fig. 5.2 sketches the applied pulse sequence. The signal-to-noise ratio of the selectively acquired 2D echo curve is considerably lower despite the increased number of transients. This is due to the fact that now only a small portion of the sample, namely the molecules next to Cu^{2+}, contribute to the FID. From the similarity of the two curves, we inferred that the dynamics of glycerol are not influenced by the presence of the relaxation agent in low concentration.

5.2 Glycerol: Temperature Dependence

Since the temperature dependence of the heterogeneity length scale is central to many theories, we attempted to measure ξ_{het} as a function of temperature. Unfortunately, there are strict experimental limitations. The accessible temperature range is limited at the low end by the requirement that filter delays have to be shorter than the ^{13}C spin-lattice relaxation time, T_1. The high temperature limit was chosen so that the rate exchange process occurred on a longer time scale than the ^{1}H spin diffusion. Additionally, one has to ensure that evolution and acquisition times (during both of which it is assumed that no motion occurs) are much shorter than mixing times. This means roughly: $t_1 = t_{\text{p}} \approx 1\text{m}s < t_{\text{m}} < T_1(^{13}\text{C}) \lessapprox 10$ s. Only small changes in the temperature near T_{g} will result in drastic changes of the α-relaxation time which is only measurable in the above mixing-time window.

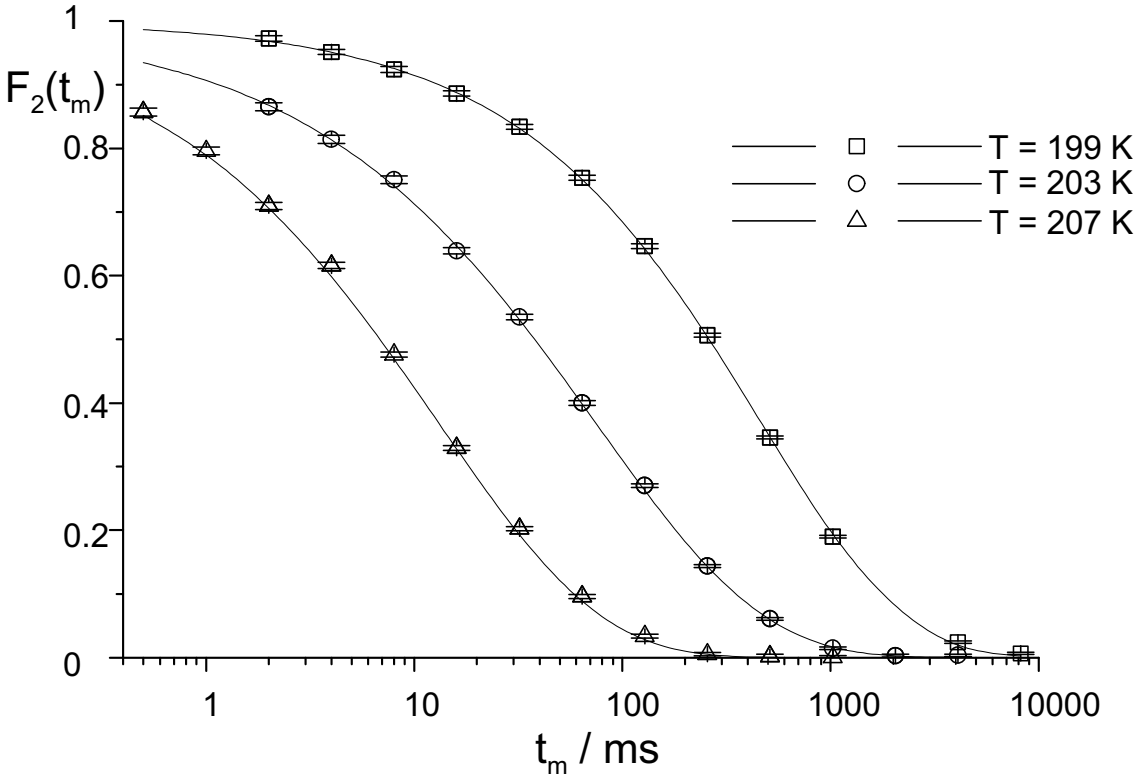

Figure 5.3: Two-time correlation functions $F_2(t_\mathrm{m})$ for glycerol, fitted with a KWW function at 199 K ($\tau = 460$ ms and $\beta = 0.62$), 203 K ($\tau = 72$ ms and $\beta = 0.51$), and 207 K ($\tau = 14$ ms and $\beta = 0.56$).

Fig. 5.3 shows two-time correlation functions $F_2(t_\mathrm{m})$ together with their fits to the KWW function for the three temperatures 199 K, 203 K, and 207 K. The 4D3CP experiments were performed at these temperatures. Fig. 5.4 shows the results of the 4D3CP NMR experiment at $T = 203$ K. The data with and without dynamic selection decay on similar time scales. Higher signal-to-noise ratios were obtained in these NMR experiments as compared to experiments by Tracht et al. [1999c] for three reasons: the labelling density was higher by a factor of three, temperatures were lower resulting in a gain of roughly 50% due to the Boltzmann factor (cf. Eq. 1.10)

$$M_0(210\ \mathrm{K}) = \frac{CB_0}{k_\mathrm{B} 210\ \mathrm{K}} \approx 1.5 \quad \frac{CB_0}{k_\mathrm{B} 315\ \mathrm{K}} = M_0(315\ \mathrm{K}). \tag{5.1}$$

and, due to a short $T_1(^1\mathrm{H})$ the recycle time of successive scans could be reduced from 4.8 s to 2 s. These three factors result in a nine-fold gain in signal intensity over the PVAc experiment assuming comparable CP efficiency.

The heterogeneity length scale, ξ_het, is determined using a modified concept originally

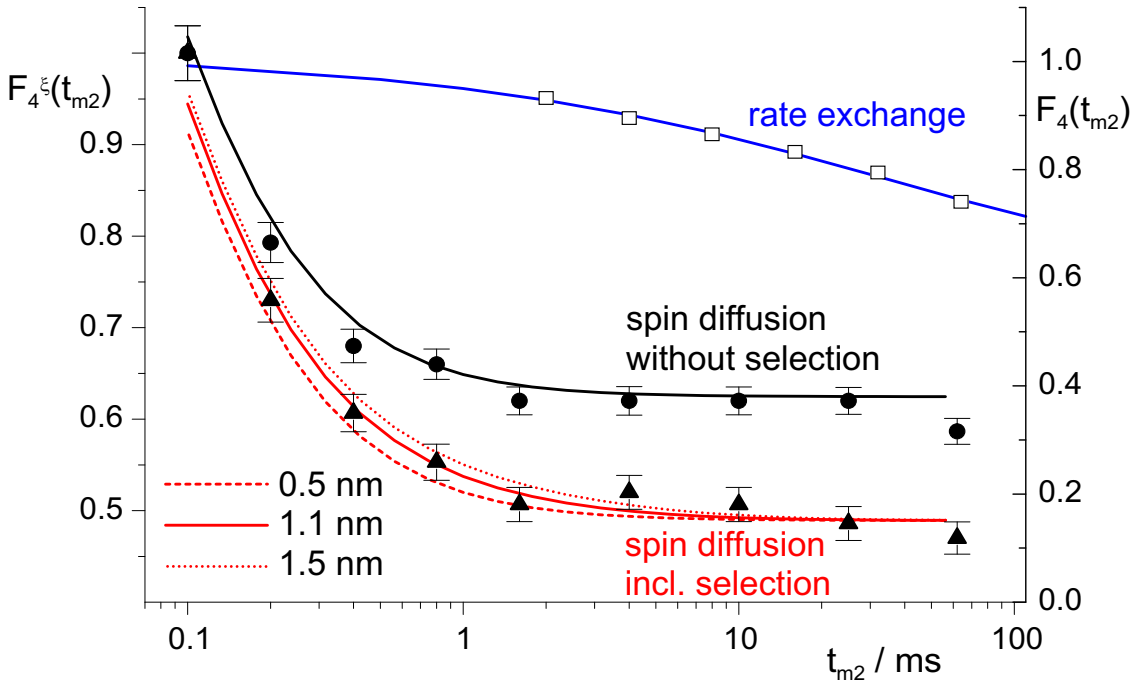

Figure 5.4: Echo intensities for the 4D3CP NMR experiment on glycerol as a function of the second mixing time, t_{m2}, for experiments with (filled triangles) and without (filled spheres) dynamic selection. Displayed are simulations for the reference experiment and for the two-filter experiment for different values of ξ_{het}. Over the course of the experiment rate exchange plays no important role (open squares).

described by Tracht et al. [1999c]. In Section 4.3 of the preceding chapter, this modified concept is developed. Using the modified method one arrives at Eq. 4.9 (p.66) used in the present data analysis. Eq. 4.9 sufficiently describes the dependence of magnetisation, M, on the spin-diffusion time t_{m2} and on four constants: the average ^{13}C density (ξ_0^{-3}), the spin-diffusion coefficient (D), the magnetisation spread after cross polarisation (a), and the gap in the pair-correlation function (g). While the ^{13}C density is defined by the level of enrichment, the latter two constants can be determined in a separate reference experiment. A reasonable value describing the gap, g, in the pair-correlation function has to be found.

In Section 4.3 it is shown by fitting reference diffusion curves for 3D hard-sphere systems that the gap, g, has to be smaller than the centre distance of two nearest neighbours, r_{NN}, (cf. Section 4.3). The exponential approximation (Eq. 4.8) best accounts for deviation from the real pair-correlation function (see, e.g., Fig. 4.1d taken from Root and Stillinger [1989]) when a gap of $g \approx \frac{3}{5} r_{NN}$ is used. Fortunately, the parameter r_{NN} is

directly accessible from MD simulation studies performed on the molecules of concern for the present study. Root and Stillinger [1989] find an $r_{\mathrm{NN}} \approx 3.5$ Å for glycerol, which leads to $g_{\mathrm{glycerol}} := 0.2$ nm.

The lower data set in Fig. 5.4 is fit by Eq. 4.9. For details of the fit procedure see Section 4.3. The level of selection, p, is determined by the mixing times t_{m1} and t_{m3}, and was equal to 70% for these experiments. To achieve the same p for all temperatures, t_{m1} and t_{m3} have to be set according to the relaxation rate obtained in the 2D echo experiment. Since the values of a, D and g are fixed, ξ_{het} is the only free parameter in this fit. This procedure yields ξ_{het} values of 1.3 nm for 199 K, 1.1 nm for 203 K and 1.0 nm for 207 K. A cube with a sidelength equal to ξ_{het} contains 18, 11, and 8 glycerol molecules for these three temperatures, respectively.[2] Note that this deviates from earlier published results [Reinsberg et al., 2001]. However, this deviation, stemming from re-analysis of the data (i.e. using the modified pair-correlation function featuring a gap), is within the estimated error bars and thus has no implications on the conclusion drawn from the results to date.

The error-estimation method is explained in Section 5.4.

5.3 OTP: Selection-Level Dependence

In addition to the temperature dependence of the heterogeneity length scale, the shape of the domains forming the heterogeneities is an interesting question. One must admit that this is a rather ambitious undertaking. Nevertheless, in the preceding chapter it is shown how a qualitative statement about the domain shape in 3D hard-sphere systems can be made based on selection level-dependent measurement of the length scale, ξ_{het}. The present section attempts a proof-of-principle for level-dependent NMR measurement on the molecular glass former OTP.

Fig. 5.5 displays the results of the 4D3CP experiment on *o*-terphenyl for a selection level $p = 62\%$ as measured by Reinsberg et al. [2002]. Similar to the glycerol analysis (Section 5.2), first experimental parameters (spin-diffusion coefficient, magneti-

[2]For this estimate a density of $\rho = 1.26 \frac{\mathrm{g}}{\mathrm{cm}^3}$ and a molecular weight of $M_{\mathrm{w}} = 92.1 \frac{\mathrm{g}}{\mathrm{mol}}$ were used. Accordingly, a glycerol molecule occupies a volume of 0.12 nm^3.

sation spread) have to be fixed by fitting the reference curve (solid spheres in Fig. 5.5). Again, the gap, g, characteristic for the modified pair-correlation function Eq. 4.8, can be extracted from published MD simulations [Mossa et al., 2000]. Mossa et al. found a neighbour distance $r_{\mathrm{NN}} \approx 5$ Å for OTP. This leads to $g_{\mathrm{OTP}} := 0.3$ nm.

With the additional parameter g being fixed, fitting yields $\xi_{\mathrm{het}} = (2.2 \pm 1)$ nm, $\xi_{\mathrm{het}} = (2.3 \pm 1)$ nm, and $\xi_{\mathrm{het}} = (2.9 \pm 1)$ nm for 42%, 62% (displayed in Fig. 5.5), and 82% selection, respectively. We see in Chapter 4 that it is possible to quantitatively assert a dendritic-like topology for a hard-sphere system in a computer experiment. It is impossible to draw such a positive and definite conclusion based solely on the NMR results for any of the three glass formers OTP, glycerol, and PVAc. We only know that ξ_{het} gives the shortest dimension of a likely fractal moiety of slow molecules. Under the experimental conditions of selection levels in excess of 70%, this fractal object could well be one fully percolating cluster.

Statistical errors will be discussed in the following section while other systematical

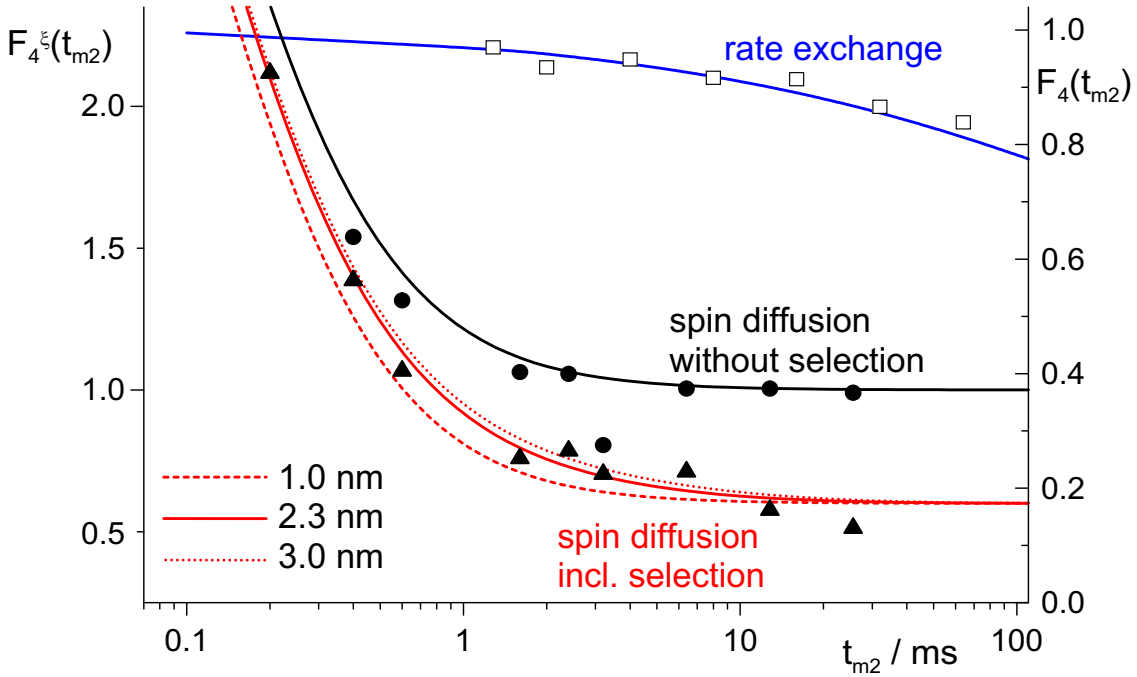

Figure 5.5: Echo intensities for the 4D3CP NMR experiment on OTP as a function of the second mixing time, t_{m2}, for experiments with (filled triangles) and without (filled spheres) dynamic selection. Simulations are displayed for the reference experiment and for the two-filter experiment for different values of ξ_{het}. Over the course of the experiment rate exchange within regions of dynamic heterogeneity plays no important role (open squares) as detected by $F_4(t_{\mathrm{m2}})$.

errors are studied in Section 5.5.

5.4 Estimation of Error

Of course, an experimental result is only useful if it is reported in conjunction with the associated error. This is especially important if, based on an experimental result, one tries to rule out or substantiate a theoretical prediction. The error estimate for the value ξ_{het}, which is central to this section, is not straightforward and hence deserves to be examined more carefully. The procedure for determining this error estimate is explained below and is sketched in Fig. 5.6.

Every FID that is used to determine the echo height at a certain mixing time, t_{m2}, carries a certain amount of noise. The statistical error of the echo intensity, $F_4^{\xi}(t_{\text{m2}})$, limits the accuracy of the experimentally derived heterogeneity length scale. Given an analytical dependence of ξ_{het} on $F_4^{\xi}(t_{\text{m2}})$, it would be possible to extract an uncertainty $\Delta\xi_{\text{het}}$ based on a known statistical error of the measured data points of $F_4^{\xi}(t_{\text{m2}})$. However, ξ_{het} is iteratively extracted as a parameter from the best fit of a function representing the experimental observable. That is why an error estimation is approached differently from conventional methods.In general terms, the uncertainty of the measured data points of the magnetisation decay is investigated for its influence on the variance of the extracted heterogeneity length-scale parameter, ξ_{het}.

As mentioned above, the standard deviation of an echo intensity representing a value of the function F_4^{ξ} at a certain mixing time t_{m2} can be obtained from the noise of the data points in a region of the FID where no signal is observed (see Fig. 5.6 step (i)). Given this statistical error of the noise, $\sigma_{\text{noise}} =$ standard deviation of one data point of the FID, the adjusted standard deviation of the determined echo height $\sigma(F_4)$ is estimated based on how many FID data points, N, in the time domain contribute to the determination of the echo height according to

$$\sigma(F_4^{\xi}) = \frac{1}{\sqrt{N}}\,\sigma_{\text{noise}}. \tag{5.2}$$

Once this uncertainty is known, a set of echo decay curves is created (step (ii)). The data points of these curves are taken from the measured decay, F_4^{ξ}, plus an additional

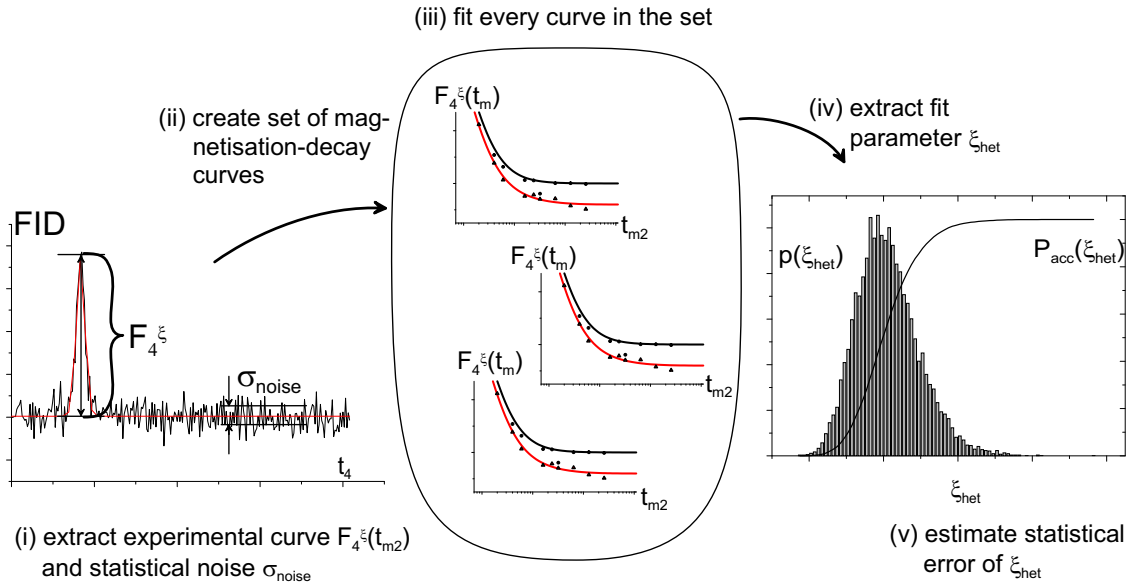

Figure 5.6: Sketch of the procedure for determining the statistical uncertainty of ξ_{het}. Starting from the FID (left) acquired using the 4D3CP pulse sequence a set of curves (middle) is created that yield a distribution of ξ_{het} (right). Steps (i) to (v) are explained in the text. The resulting histograms are shown in Fig. 5.7 and discussed in the text

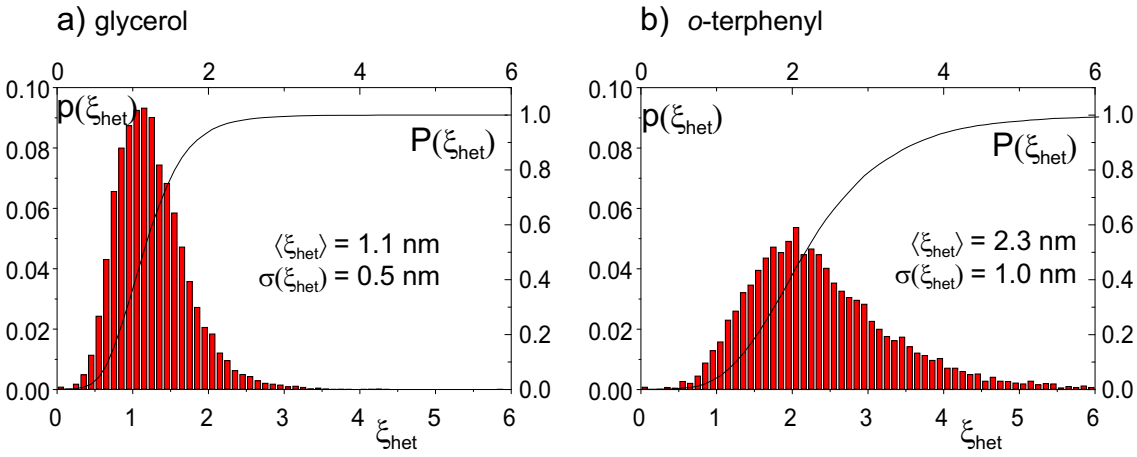

Figure 5.7: Histograms of ξ_{het} for glycerol (a) and *o*-terphenyl (b) as obtained from 10,000 fits of data sets that were created as described in the text and sketched in Fig. 5.6.

random fluctuation determined by a Gaussian distribution with an average of $F_4^\xi(t_{m2})$ and a standard deviation of $\sigma(F_4)$. Then, each of these created data sets is fit to yield a value of the heterogeneity length, ξ_{het} (steps (iii) and (iv)). Histograms of ξ_{het} are shown in Fig. 5.7. Although the uncertainty for the OTP experiment (Fig. 5.7b) seems to be greater, the relative uncertainty is about the same as for the glycerol experiment.

5.5 Erroneous Selection of Single Molecules: Simulations

It could be argued that potential artefacts make the actual heterogeneity length appear larger than the measured ξ_{het}. If some "fast" molecules were incorrectly labelled as slow, then these molecules would appear to form a cluster of slow entities the size of one molecular diameter (0.5 nm) and thus bias the results. In general, this mislabelling will be less influential than expected because lower CP efficiency for fast molecules will generally decrease the contribution these molecules make to the overall NMR signal. However, the problems of mislabelling are looked at carefully below. As the analysis shows, the two potential artefacts do not have a significant effect on the obtained results. The two problems that can occur are:

(i) Fast molecules can seem slow because their orientation relative to the magnetic field is such that the differential change of frequency with respect to change in orientation is close to zero.

(ii) The initial filter in the 4D3CP NMR experiment might select fast molecules that have reoriented only by a very small amount as would happen with a finite probability for a random walk on a sphere.

The first issue was addressed experimentally. As shown by Tracht et al. [1999a] and explained in Section 3.3, when this type of selection error is dominant, the value of the rate exchange parameter, Q, becomes greater than 10. Since the 4D NMR experiments on glycerol gave Q near unity, consistent with results by Hinze et al. [1998], this artefact is not significantly influencing the results. Additionally, simulations have been performed to estimate both effects (i) and (ii).

As the selection method of the 4D3CP experiment relies on 2D echo filters, the efficiency of such filters are investigated using Monte Carlo simulations. A distribution of rates is created and monitored using a (simulated) reduced 2D exchange experiment. The results are simultaneously cross-checked with information about the actual reorientation of the molecules. Fig. 5.8 to Fig. 5.10 explain the procedure adopted. Fig. 5.8 shows

the starting point of the simulation. The parameters σ and τ_0 of the displayed log-Gauss distribution are chosen so that the corresponding 2D echo curve can be fit with τ_{KWW} and β_{KWW} values similar to the obtained experimental result. The reason for choosing log-Gauss rather than KWW distribution is that the latter has no closed analytical form (for $\beta \neq 0.5$) whereas the former closely reproduces the required asymmetric shape of a KWW distribution and is tractable in a closed analytical form. The details of calculating the log-Gauss distribution are given in Appendix A.2.

The 2D echo filter measures molecular motion by detecting a change in resonance frequency ω. For the foregoing reason the molecule's frequency before and after molecular motion is noted. As the geometry of motion is not expected to substantially influence the analysis of filter efficiency, only diffusional motion mimicked by small angle (2°) jumps at the assigned rate, τ_0^{-1}, is implemented. A sufficient change in frequency ($\Delta\omega > \Delta\omega_{\mathrm{threshold}}$) labels a molecule as *moved* (i.e. apparently fast) irrespective of its assigned rate. The threshold $\Delta\omega_{\mathrm{threshold}}$ is chosen so that the 2D curve obtained from the correlation function $\langle \cos\omega_1 t_{\mathrm{p}} \cos\omega_2 t_{\mathrm{p}} \rangle$ is reproduced by the curve measuring the rigid fraction ($N_{\mathrm{r}}/(N_{\mathrm{m}} + N_{\mathrm{r}})$) of the entire ensemble at any given mixing time, t_{m}.

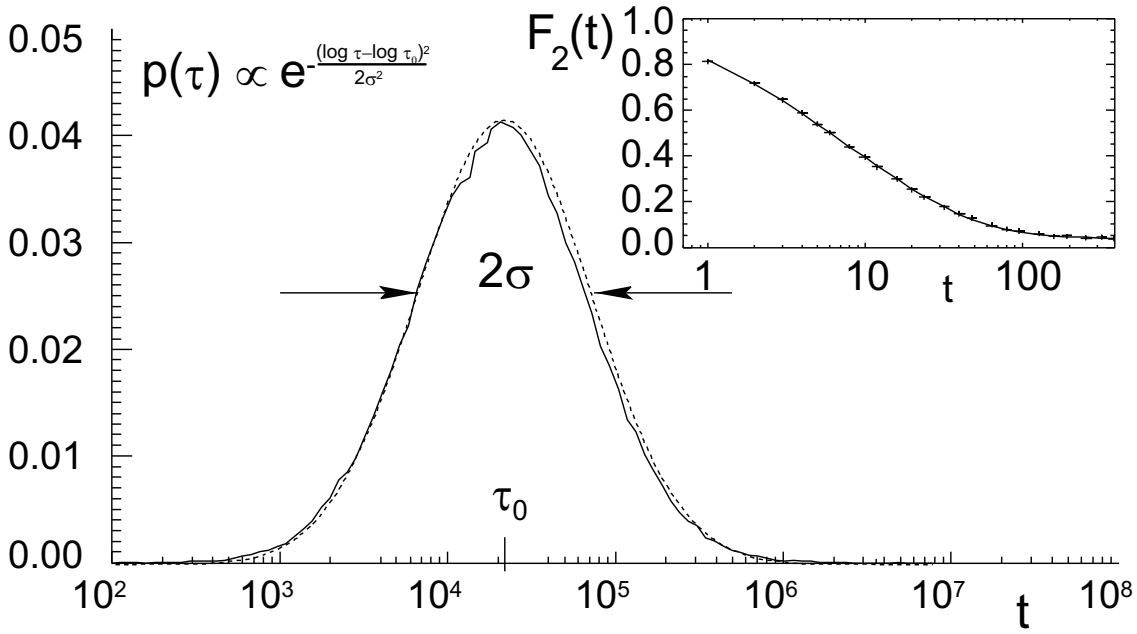

Figure 5.8: Log-Gauss distribution of relaxation rates as used for the simulation. Parameters τ_0 and σ were chosen so that the corresponding 2D echo curve (cf. inset) could be fit (solid line in the insert) with a KWW function using parameters β and τ as found for the experiment.

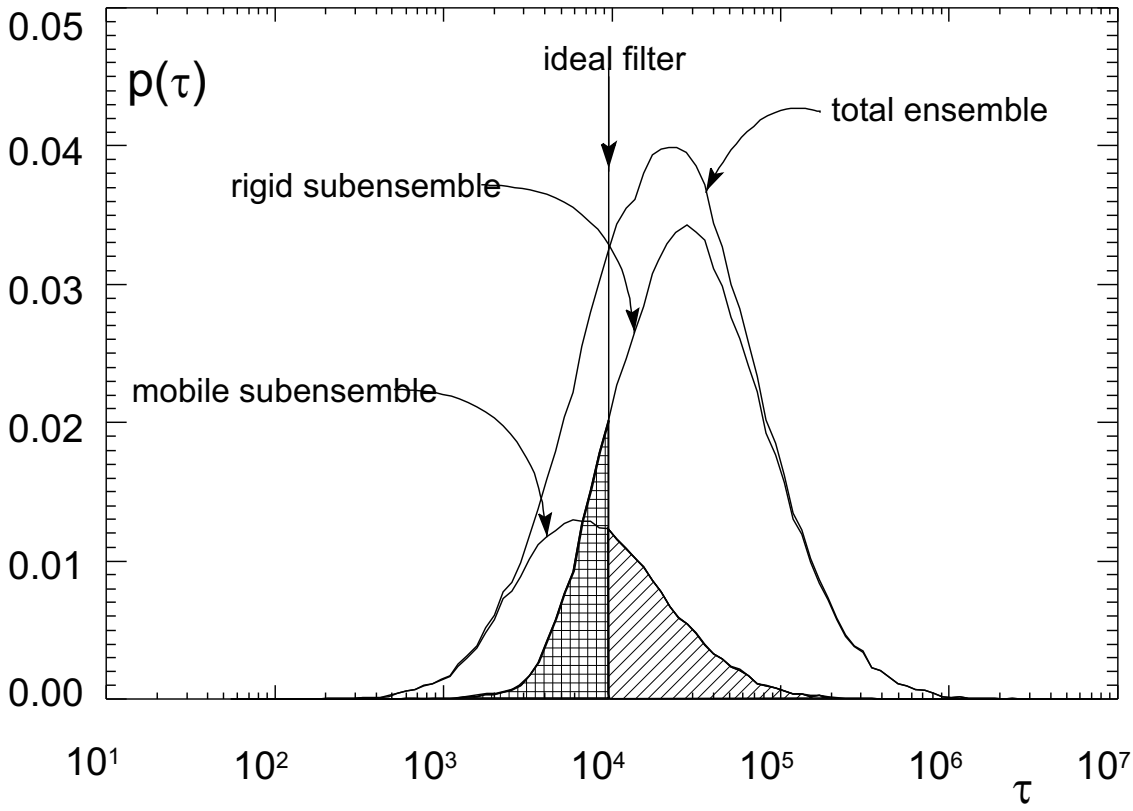

Figure 5.9: Snapshot of the selected subensembles from MC simulation for a mixing time of $t_{\mathrm{m}} = 2$. The sum of the slow and rigid subensembles gives the total ensemble as already shown in Fig. 5.8. Given the ratio of the two subensembles, an ideal filter would have to split the rate distribution as indicated by the vertical line at $\tau = 9600$. However, as the applied 2D echo filters exhibits non-ideal properties (see text) the edges of the ideally-filtered subensembles are blurred out. The checked and hatched area indicates regions that have been erroneously selected.

The ratio of molecules labelled as *moved* to molecules considered as *rigid*, $N_{\mathrm{m}}/N_{\mathrm{r}}$, should obviously increase over the course of a continued waiting (mixing) time, t_{m}. Fig. 5.9 displays a snapshot taken for a comparatively short mixing time. Only a few molecules have moved (represented by the 'mobile-subensemble' curve in Fig. 5.9) whereas most molecules remained rigid as judged by the criterion $\Delta\omega > \Delta\omega_{\mathrm{threshold}}$. The vertical line indicates where an ideally sharp filter would have divided the total ensemble assuming the ratio of $N_{\mathrm{m}}/N_{\mathrm{r}}$ extracted from the two-time correlation function.

Generally, particles can be mislabelled in two ways: They can be considered as *mobile* although they are slow (hatched area in Fig. 5.9), or, molecules can be considered as *rigid* although their short relaxation time qualifies them as fast (checked area in Fig. 5.9). Obviously, the hatched and the checked area must be equal in size. Note that both rea-

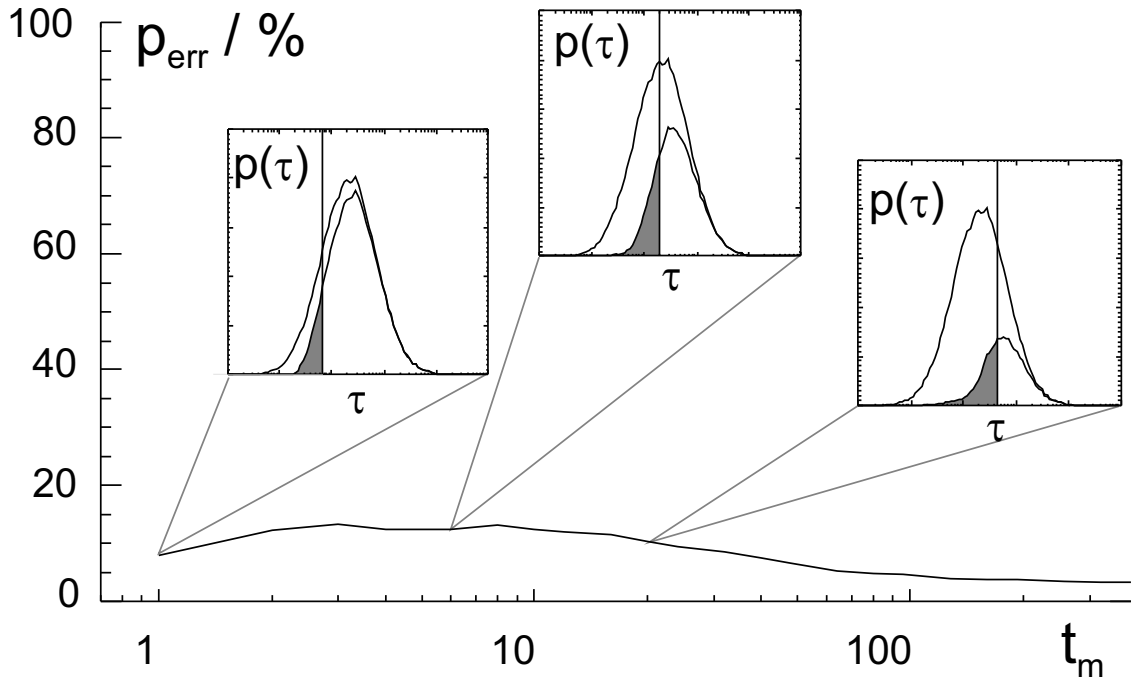

Figure 5.10: Relative portion of the erroneously selected subensembles (cf. marked areas in Fig. 5.9) as function of the mixing time. The three insets shown from left to right exemplify the selected subensembles at a short, an intermediate, and a long mixing time, respectively.

sons (i) and (ii), as are introduced at the outset of this section, are modelled by the above-described simulation procedure.

Fig. 5.10 shows how the portion of erroneously labelled particles evolves while the mixing time is increased. As can be seen, the fraction of molecules that were selected erroneously is about 15% under the experimental conditions that were chosen for the 4D3CP experiment. To first order, a linear contribution of the erroneously selected molecules can be assumed: $15\% \cdot 0.5$ nm $+ 85\% \cdot \xi_{\text{het,real}} = \xi_{\text{het,apparent}}$. This results in a ca. 10% higher value of ξ_{het}, which is within the reported error margins.

5.6 Summary and Conclusion

The length scale for dynamic heterogeneity in glycerol is significantly shorter than the value of 3.7 nm obtained for poly(vinyl acetate) (PVAc) using the 4D3CP technique. The results obtained for *o*-terphenyl (2.9 nm for a comparable level of selection, p), though smaller, are comparable to the value obtained for PVAc. One should point out that

heterogeneities for glycerol and PVAc have previously been reported using an analysis method that yielded values differing slightly from re-analysed data (3 ± 1 nm for PVAc [Tracht et al., 1998] instead of the above 3.7 nm and 1.0 ± 0.5 nm for glycerol [Reinsberg et al., 2001] instead of 1.1 nm). As these values are still within the margins of error, earlier conclusions drawn from the result are not affected in any way.

Having found the heterogeneity length scale for the two additional glass formers glycerol and OTP, it is interesting to speculate on the reason for differences and similarities in ξ_{het} for the three studied substances.

Glycerol and *o*-terphenyl are low molecular weight glass formers whereas PVAc is a polymeric system. One might anticipate that ξ_{het} depends in some manner on the size of the moving unit. While a single molecule would be a reasonable guess for glycerol or OTP, it is not obvious how to determine this size for PVAc. Supposing a rearranging entity has the size of a repeat unit of PVAc, 420 rearranging entities would be found in a box of the size of $\xi_{\text{het}} = 3.7$ nm. It is, however, equally possible to envisage a rearranging entity larger than a monomeric unit due to the topological constraints of the linear polymer chain. The characteristic ratio introduced by Flory [1969] is viewed as a measure for the number of monomer units that comprise a stiff polymer-chain element (Kuhn length):

$$C_\infty = \frac{\langle R^2 \rangle}{N a_{\text{b}}^2}, \tag{5.3}$$

where $\langle R^2 \rangle$ is the end-to-end vector length of a polymer chain, N the degree of polymerisation, and $a_{\text{b}}^2 = \sum_i a_{\text{i}}^2$ the sum of the squares of the lengths of the backbone bonds of one monomer unit. Using the viscosity-molecular weight relationship in a theta solvent, a C_∞ of 7.9 was found[Ueda and Kajitani, 1967]. This leaves us with roughly 55 'stiff' and rearranging units per box of side length ξ_{het}. The number of molecules per immobile domain for the low molecular weight glass formers is found to be 76 and 10 for *o*-terphenyl and glycerol, respectively. In other words, PVAc and OTP have a similar number of units per domain, whereas glycerol shows significantly fewer molecules per slow nanoregion.

There might be an interplay of length scale and width of distribution of relaxation rates, τ. Given a system with a small length scale, particles might move with a lesser

range of mobility than particles in a system with large domains. Thus, a smaller length scale could be associated with a smaller distribution of relaxation rates. Indeed, for glycerol one finds a fairly narrow distribution of relaxation rates, $\sigma_\tau = 1.3$ decades, consistent with a large KWW exponent, $\beta_{\mathrm{KWW}} = 0.55$ at $T = T_\mathrm{g} + 14$ K. However, for PVAc the distribution of rates is wider ($\sigma_\tau = 1.7$ decades, $\beta_{\mathrm{KWW}} = 0.45$ at $T = T_\mathrm{g} + 10$ K). The rate distribution is even wider for OTP ($\sigma_\tau = 1.8$ decades, $\beta_{\mathrm{KWW}} = 0.41$ at $T = T_\mathrm{g} + 9$ K). In summary, larger domains (larger ξ_{het}'s) can tentatively be associated with wider relaxation-rate distributions (smaller β's). In this context, it is worth pointing out that attempts have been made to correlate fragility and spectral width, which, is, in turn, directly related to the KWW exponent β. Böhmer et al. [1993] studied over 60 glass formers at approximately T_g and found that β is strongly and positively correlated with fragility, m.

It is interesting to compare the temperature-dependent measurement of ξ_{het}(glycerol) with experimental and theoretical estimates of the size of cooperatively rearranging regions (CRR's) in glycerol. First of all, it is not clear how to relate the length scale of dynamic heterogeneity to the size of cooperatively rearranging regions. These two length scales could be identical, but consistent with ref. Tracht et al. [1998], ξ_{het} could also be an upper bound for the length scale of the CRR's. This reflects the view that molecules which relax on widely different times scales cannot do so in a highly cooperative manner. It is noteworthy that some researchers, e.g. Donth et al. [2001], believe that the ξ_{het} obtained by NMR is actually smaller than the cooperativity length scale measured using among other techniques heat-capacity spectroscopy (HCS). They base this on the statement that the NMR-ξ_{het} measures the size of only a *slow* subensemble whereas the characteristics length by HCS probes the CRR in its entirety. Whether one can reconcile Donth's larger characteristic length with our smaller ξ_{het} based on this comparison is questionable given a rather large selection level of ca. 70% for the NMR experiments.

In the discussion below, it will be assumed that the shortest dimension of a heterogeneity, ξ_{het}, places an upper bound on the size of the CRR's, ξ_{CRR}.

Arndt et al. [1996] confined glycerol in pores and measured the relaxation rate using broad-band dielectric spectroscopy. The average relaxation rate of glycerol was found

not to depend on pore sizes down to 2.5 nm. By allowing for a surface-bound layer of molecules, the authors concluded that the dynamic glass transition takes place in a sub-volume with a diameter of about 0.7 nm. This is considerably smaller than what has been deduced for other hydrogen-bonding glass formers and is consistent with our results. Korus et al. [1997] calculated the number of molecules per CRR for glycerol using heat capacity spectroscopy data. Using the temperature dependence specified by their model, one calculates 100 molecules per CRR at 207 K, to be compared with the finding from NMR of 8 molecules in a box with sides equal to ξ_{het}. Korus et al. [1997] reconciled this discrepancy based on the assumption $\xi_{\text{het}} < \xi_{\text{CRR}}$. Based on the reasons mentioned in the preceding paragraph, however, the author is reluctant to agree.

A number of researchers have used the Adam-Gibbs model to determine the number of glycerol molecules in a CRR at T_{g}. As described by Johari [2000], these treatments yield 3 molecules or less, and are thus also consistent with the results reported here if $\xi_{\text{het}} > \xi_{\text{CRR}}$. Colby [2000] recently presented a dynamic scaling model of the glass transition which supposes a power-law relationship between the relaxation time and size of the CRRs: $\tau \propto \xi^6$. This predicts that the size of the CRRs will change over the temperature range of our measurements by a factor of 1.8, a ratio which is consistent with our results given the error bars. Matching Colby's ξ with our measured ξ_{het}, one can suppose that a CRR contains 23 molecules at 199 K. However, for higher temperatures, one calculates numbers which can only be considered unphysical, a CRR of 1 molecule at $T_{\text{g}} + 30$ K and less than 0.1 molecule at $T_{\text{g}} + 50$ K.

The temperature dependence aside, the trend of Colby's prediction of the cooperative size depending on the fragility index is corroborated by the findings from the NMR experiments. Starting from the dynamic scaling approach, Erwin and Colby [2001] found a linear relationship between $\xi(T_{\text{g}})$ and fragility m. Table 5.1 lists fragilities, m, as compiled by Beiner et al. [2001] and Böhmer et al. [1993] and compares them to heterogeneity length scales, ξ_{het}, as obtained from 4D3CP NMR experiments.

In the model of Kivelson and Tarjus that is based on frustration-limited domains [Viot et al., 2000], the domains with different relaxation times grow slowly as T_{g} is approached, i.e. 5% over the temperature range of our experiments. This model's predictions are also

[3] according to Böhmer

[4] according to Beiner

consistent with our results.

The selection-level dependent measurement of ξ_{het} for OTP proves that, in principle and in analogy to computer experiments on hard-sphere systems, one could try to quantitatively investigate the shape of heterogeneous regions. In fact, for the computer experiment as well as the NMR experiment, the length scale remains more or less constant for increasing selection levels above a certain minimum of about 30%. This hints at a picture of domains that have nanoregions of constant size ξ_{het} at their fringes.

	PVAc	*o*-terphenyl	Glycerol
fragility[3]	95	81	53
fragility[4]	96	74	49
ξ_{het}	3.7 nm	2.7 nm	1.1 nm
β	0.45	0.41	0.55
$T - T_{\text{g}}$	10 K	9 K	14 K

Table 5.1: Summary of heterogeneity length scale from NMR

Chapter 6

Dipolar-Correlation Experiments

One of the unique advantages of NMR spectroscopy is its proven ability to separate different contributions to the spin Hamiltonian and, thereby, obtain information[Haeberlen, 1976]. The present chapter shows how such selective manipulation of the Hamiltonian can be applied to separate the dominating single-spin chemical shift, which probes orientational motion, from weak two- or multiple-spin ^{13}C-^{13}C dipole-dipole coupling which monitors rotational *and* translational motions. The chapter outlines the theoretical basis of the developed dipolar-correlation experiment. All the presented experimental data was obtained for ^{13}C-enriched glycerol.

In the past, a number of experiments proved the apparent decoupling of translational and rotational motion, most notably, the static magnetic field gradient technique used by Chang et al. [1994] and the holographic fluorescence recovery after photobleaching as employed by Cicerone et al. [1995a]. The reason for this enhancement is spatial heterogeneity and the way of averaging over rotational and translational motion is affected differently by these spatial heterogeneities.

6.1 Motivation and Pulse Sequence

The critical components of a 2D echo experiment (see Section 1.3.2) are the evolution period, t_{p}, the mixing time, t_{m}, and the acquisition period. By measuring echo heights at constant evolution times and various mixing times the correlation function

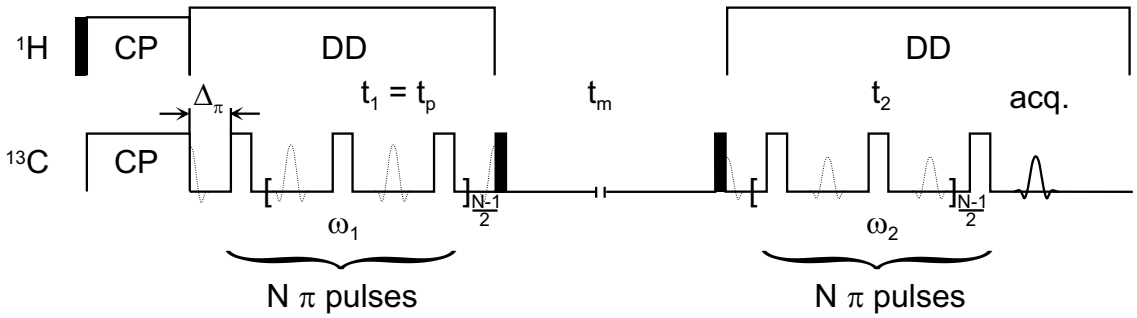

Figure 6.1: Pulse sequence of the dipolar-correlation experiment. N π pulses during the evolution period and prior to acquisition eliminate the influence of the CSA Hamiltonian. A π pulse inverts the evolution under CSA but, in contrast, leaves the evolution under dipolar coupling invariant.

$\langle \cos\omega(0)t_{\mathrm{p}} \cos\omega(t_{\mathrm{m}})t_{\mathrm{p}} \rangle$ is examined. In the conventional 2D echo experiments, the evolution period is dominated by the chemical-shift Hamiltonian, i.e. $\omega = \frac{\delta}{2}(\cos^2\theta - 1)$ where δ is the chemical-shift anisotropy.

In an experiment that aims to eliminate the evolution under chemical-shift anisotropy (CSA), other interactions should dominate the evolution period. If the contributions to the total Hamiltonian consists of a CSA ($\mathscr{H}_{\mathrm{CSA}}$) and a dipolar component ($\mathscr{H}_{\mathrm{D}}$), one might hope for a separate treatment of these contributions. As CSA and dipolar coupling transform according to tensors of *different* rank under rotations in spin space [Spiess, 1978], they are easily separated. A single π pulse in the centre of the evolution time, however, is not sufficient to effectively invert the evolution under CSA. A train of π pulses (as shown in Fig. 6.2) with a short spacing, Δ_π, will, even for imperfect pulses, be more effective in reducing the contributing parts of the Hamiltonian to only the leading terms in a series expansion[Carr and Purcell, 1954].

The pulse sequence shown in Fig. 6.1 was used to study ^{13}C-labelled glycerol in different concentrations. This experiment will be referred to from here onwards as the *dipolar-correlation experiment* and the resulting correlation functions shall be denoted by F_2^{DC}. In order to understand and later exploit the mechanisms governing the decay of the measured dipolar-correlation function, the features of this decay will be described in detail below.

Fig. 6.2 shows F_2^{DC} decay curves for a number of evolution times of glycerol. The sample was studied at $T = 206$ K. The decays exhibit features comparable to the 2D echo decays. Both the 2D echo decays and the dipolar-correlation experiment can be conve-

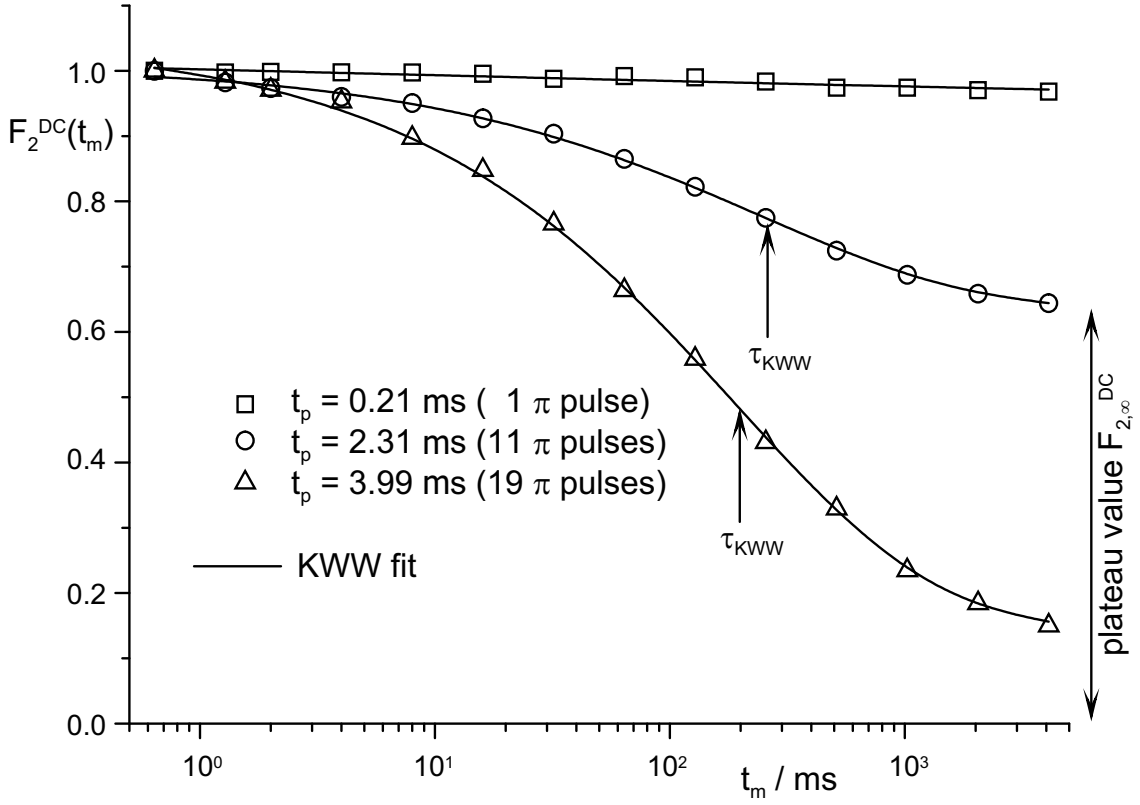

Figure 6.2: Decay of dipolar-correlation curves as a function of mixing time, t_{m}, for glycerol. The π-pulse spacing is 100 μs. An increase of the evolution time, t_{p}, leads to a decrease in the plateau value (see discussion in Section 6.2) but to no significant change in the decay time of F_2^{DC}, τ_{KWW} (see discussion in Section 6.3).

niently fitted with KWW functions. However, the obtained stretching parameter for the former is slightly larger ($\beta = 0.51 \ldots 0.62$) than for the latter ($\beta = 0.42 \ldots 0.5$). A more important difference is that the decay curves $F_2^{\mathrm{DC}}(t_{\mathrm{m}})$ reach a plateau value considerably higher than the one observed in $F_2(t_{\mathrm{m}})$ (standard 2D echo) for a given value of t_{p}.

A loss of correlation, i.e. the change of dipolar coupling, observed in the two-time correlation function could potentially be ascribed to the following: Either, the dipolar coupling changes as a result of motion (translation, rotation), or the spin state of the involved nuclei changes. Since we are interested in the motional dynamics, it is essential to identify which of these two reasons is the main source of correlation loss and under what circumstances. At this point, a general remark about the contributing factors to the resonance frequency ω is in order. Given that the pulse sequence eliminates evolution under chemical shift anisotropy, only dipolar coupling to neighbouring spins remains as

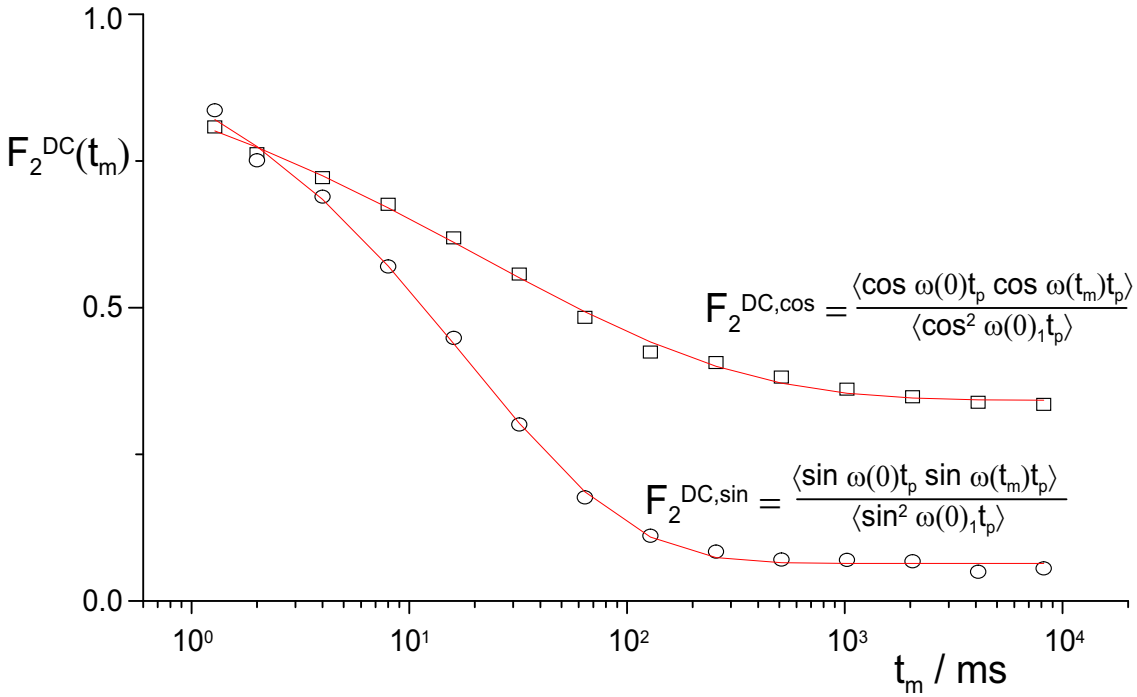

Figure 6.3: Comparison of the sine and the cosine dipolar-correlation function of glycerol above the glass transition temperature ($T = 210$ K). Both decay functions can be fitted with KWW function with similar decay time: $\tau_{\sin} = 18$ ms and $\tau_{\cos} = 21$ ms. The plateau value vanishes for the sine correlation while it is finite for the cosine correlation function (see discussion in the Section 6.2). The small detectable offset in $F_2^{\mathrm{DC,sin}}$ can be explained by a not perfectly on-resonance acquisition. The contributions to $\omega(t_{\mathrm{m}})$ are discussed in the text.

influencing factor. The *size* of this contribution depends on the dipolar couplign constant ($\frac{3\cos^2\Theta_{ij}-1}{r_{ij}^3}$). The *sign* of the contribution depends on the spin state of the neighbouring spin (+ or for *spin up* and − for *spin down*). Assuming that the dipolar coupling is dominated by the coupling to the next neighbouring spin, a flip of this spin would result in an inversion of the resonance frequency.

A comparison of the two-time sine and cosine correlation functions shown in Fig. 6.3 reveals that no one flip of the spin dominating the dipolar coupling is the reason for the decay in the absence of motion. A single spin flip would lead to an inversion of the frequency, $\omega_1 \rightarrow \omega_2 = -\omega_1$, which does not lead to a correlation loss in the even cosine correlation function. The effect of a spin inversion on the odd sine correlation function, on the other hand, would be a dramatic loss of correlation, manifesting itself in a much shorter decay time. Decay times of both types of correlation functions are similar in size and we can hence conclude that at the temperature studied either molecular motion or a

collective change of the spin state is responsible for the loss of correlation. The latter reason will be excluded as the main contribution in the interesting temperature regime above T_{g} on grounds of its temperature dependence (see also Section 6.4). The former reason is assumed to be the principal contribution to the correlation loss at $T > T_{\mathrm{g}}$.

6.2 Plateau Values of $F_2^{\mathbf{DC}}$

Explaining the plateau values by starting from reasonable assumptions provides us with an important cross-check for testing the concept used to understand the dipolar-correlation experiment. To do this, we will first investigate how the plateau value arises for general two-time correlation functions. Then we will turn to the specific case at hand, where a spread in frequency due to dipolar coupling exists. Equipped with this knowledge, we will qualitatively interpret data obtained from dipolar-correlation experiments on glycerol.

In general, the plateau value to which the two-time correlation functions decay is a measure of the cosine- (or sine-) argument distribution, ωt_{p}. Given a certain distribution (often described by the width, δ, and the shape of the distribution), one can calculate how this plateau value depends on the parameter t_{p}. To make this dependence $F_{2,\infty}$ independent of width and only dependent on distribution type, one often considers the relationship of $F_{2,\infty}$ on the generalised parameter $t_{\mathrm{p}}\delta$.

Fig. 6.4 summarises how different distribution functions for the resonance frequency affect the plateau-value dependence on the selectivity parameter, $t_{\mathrm{p}}\delta$. The calculation of the plateau values,

$$\lim_{t_{\mathrm{m}}\to\infty} F_2(t_{\mathrm{m}}) =: F_{2,\infty} \tag{6.1}$$

can be done by calculating

$$F_{2,\infty}^{\cos} = \frac{\langle \cos\omega_1 t_{\mathrm{p}} \cos\omega_2 t_{\mathrm{p}} \rangle}{\langle \cos^2 \omega_1 t_{\mathrm{p}} \rangle}, \quad \text{or,} \quad F_{2,\infty}^{\sin} = \frac{\langle \sin\omega_1 t_{\mathrm{p}} \sin\omega_2 t_{\mathrm{p}} \rangle}{\langle \sin^2 \omega_1 t_{\mathrm{p}} \rangle}. \tag{6.2}$$

Most often cosine correlation functions are observed and we therefore centre our efforts around $F_{2,\infty}^{\cos}$ although $F_{2,\infty}^{\sin}$ will be considered briefly. Eq. 6.2 is the normalised two-time

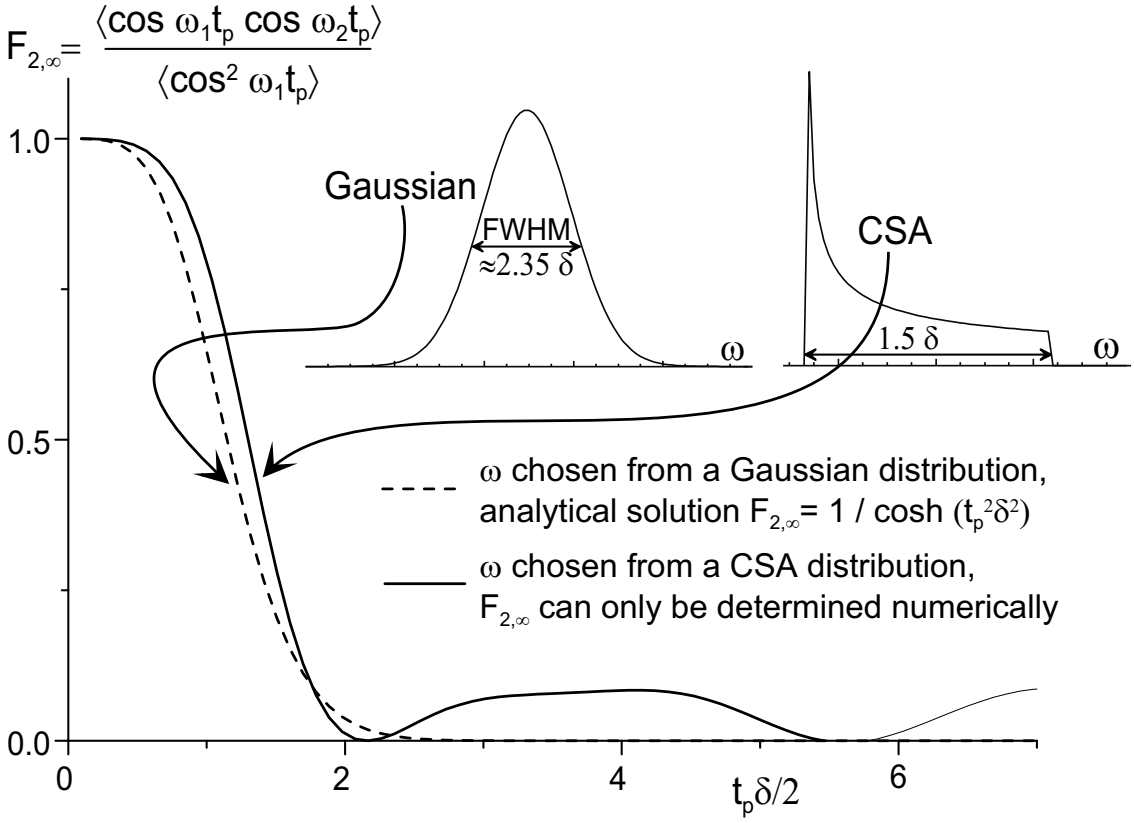

Figure 6.4: The finite value of a two-time correlation function reflects the range of possible choices of ω given a certain distribution of resonance frequencies. A Gaussian distribution (left inset) leads to a $F_{2,\infty}(t_\mathrm{p}\delta)$ that can be described by a closed analytical expression whereas a powder pattern resulting from CSA interaction (right inset) leads to a $t_\mathrm{p}\delta$ dependence of $F_{2,\infty}$ that can be numerically calculated from Fresnel-integral evaluation. Note that the full width at half maximum (FWHM) of the Gaussian frequency distribution is given by the distribution spread δ.

correlation function for two uncorrelated frequencies ω_1 and ω_2. The resonance frequencies are uncorrelated because the orientation of a molecule (or whichever configurational parameter that determines the value of the resonance frequency $\omega_{1/2}$) will be totally uncorrelated to its starting orientation after an infinitely long (for the purpose of experiment, sufficiently long) mixing time.

Let us review how the finite value of the two-time correlation function F_2 for the case of exclusive evolution under the CSA Hamiltonian arises. For an ω that depends solely on the molecular orientation according to the second Legendre polynomial, $\omega = \frac{\delta}{2}(3\cos^2\theta - 1)$, the dependence of $F_{2,\infty}$ on the parameter $t_\mathrm{p}\delta$ can be calculated numerically. For the numerical integration, Fresnel integrals have to be evaluated. One can alternatively and more conveniently choose a number of random molecular orientations, calculate

the resulting resonance frequency, and determine $F_{2,\infty}^{\cos}$ and $F_{2,\infty}^{\sin}$ as given in Eq. 6.2. The results are displayed in Fig. 6.4 (solid line). While the probability of a particular resonance frequency occuring is given by

$$p(\omega) = \begin{cases} \frac{1}{\sqrt{6\delta}\sqrt{\omega+\frac{1}{2}\delta}} & -\frac{\delta}{2} < \omega < \delta \\ 0 & \text{otherwise} \end{cases} . \tag{6.3}$$

The above considerations are equally applicable to the case of non-zero asymmetry. An $\omega = \frac{1}{2}\delta(3\cos^2\theta - 1 - \eta\sin^2\theta\cos 2\phi)$ changes the probability distribution for the resonance frequency but leaves the procedure of (numerically) calculating the plateau values unchanged.

Fig. 6.4 also shows how a Gaussian frequency distribution is reflected in the dependence of $F_{2,\infty}$ on $t_{\mathrm{p}}\delta$. In fact, $F_{2,\infty}(t_{\mathrm{p}}\delta)$ can be calculated analytically under the assumption of a particular distribution, δ, of resonance frequency (an estimate for the frequency spread δ of the distribution is given further below).

$$F_{2,\infty}^{\mathrm{DC}} = \frac{\langle \cos\omega_1 t_{\mathrm{p}} \cos\omega_2 t_{\mathrm{p}} \rangle}{\langle \cos^2\omega_1 t_{\mathrm{p}} \rangle} = \frac{\langle \cos\omega t_{\mathrm{p}} \rangle^2}{\langle \cos^2\omega t_{\mathrm{p}} \rangle} \tag{6.4}$$

$$= \frac{\left(\int_{-\infty}^{\infty} \cos\omega \ \exp\left(-\omega/(2\delta^2)\right) \mathrm{d}\omega \right)^2}{\int_{-\infty}^{\infty} \cos^2\omega \ \exp\left(-\omega/(2\delta^2)\right) \mathrm{d}\omega} \tag{6.5}$$

$$= \frac{\left(\exp(-t_{\mathrm{p}}^2\delta^2)/2\right)^2}{\frac{1}{2}\left(1-\exp(-2t_{\mathrm{p}}^2\delta^2)\right)} \tag{6.6}$$

$$= \frac{1}{\cosh t_{\mathrm{p}}^2\delta^2} \tag{6.7}$$

The resulting t_{p} dependence is displayed in Fig. 6.4 (dashed line). The corresponding

sine two-time correlation function exhibits a vanishing plateau value since:

$$F_{2,\infty}^{\mathrm{DC,sin}} = \frac{\langle \sin\omega_1 t_\mathrm{p} \sin\omega_2 t_\mathrm{p}\rangle}{\langle \sin^2\omega_1 t_\mathrm{p}\rangle} = \frac{\langle \sin\omega t_\mathrm{p}\rangle^2}{\langle \sin^2\omega t_\mathrm{p}\rangle} \tag{6.8}$$

$$= \frac{\left(\int\limits_{-\infty}^{\infty} \sin\omega \ \exp\left(-\omega/(2\delta^2)\right) \mathrm{d}\omega\right)^2}{\int\limits_{-\infty}^{\infty} \sin^2\omega \ \exp\left(-\omega/(2\delta^2)\right) \mathrm{d}\omega} \tag{6.9}$$

$$= 0. \tag{6.10}$$

The plateau value vanishes for any even ω distribution since the sine itself is an odd function. In Fig. 6.3 we can observe how the plateau value vanishes for the sine correlation. The small detectable offset (< 5 %)can be attributed to an acquisition scheme that was not perfectly on resonance.

The frequency distribution for exclusive CSA interactions (the case of the 2D echo experiment) can be calculated in a fairly straightforward manner. The bilinear CSA Hamiltonian (cf. Eq. 1.16) only depends on the orientation of a CSA tensor with respect to the external magnetic field and on two parameters, δ and η, which characterise anisotropy and asymmetry of this interaction, respectively. Even though the dipolar interaction Hamiltonian is also a bilinear form, matters are complicated by the following two effects: Firstly, we cannot assume an interaction between isolated pairs of spins; generally, we have a number of spins within a given range. Secondly, the interaction is also spin-distance dependent. In general, we have to write the resonance frequency as follows:

$$\omega_\mathrm{d} = \frac{\mu_0 \gamma_{^{13}C}^2 \hbar}{4\pi} \sum_i \frac{3\cos^2\theta_\mathrm{i} - 1}{|\mathbf{r}_\mathrm{i}|^3} = 2\pi \ 7.6 \text{ kHz Å}^3 \sum_i \frac{3\cos^2\theta_\mathrm{i} - 1}{|\mathbf{r}_\mathrm{i}|^3} \tag{6.11}$$

As shown by Abragam [1961], the dipolar interaction of a uniform distribution of like spins leads to an absorption line with a Lorentz shape (i.e. Lorentz distribution of ω_d). A uniform distribution also includes spins that come arbitrarily close, leading to resonances over the whole frequency range. The introduction of a closest-approach distance cuts off frequencies farther away from the centre frequency. The overall absorptive resonance function approaches a Gaussian shape.

Considering the strong r^{-3} dependence of the dipolar coupling, it seems plausible to subdivide the influence of all the dipoles of the sample into a hierarchy of couplings as

suggested by Gottwald [1996]. Fig. 6.5a shows the pair-correlation function for carbons of intermolecular pairs of glycerol molecules. To a first approximation, one could envisage a strong dipolar coupling to a carbon in the first-neighbour shell. The resulting Pake spectrum will be convoluted with a Gaussian line that stems from the 'background' of the other spins. Admittedly, especially for a sample with 50 % enrichment of ^{13}C spins there is a likelihood of finding more than one dipolar coupled spin in the first-neighbour shell. The lineshape of a few dipolar coupled spins will certainly be more complicated than the well-known Pake pattern. The width of it will be on the same order of magnitude as for a spin pair, see Schnell and Spiess [2001]. The following convolution with a Gauss-like distribution will smear out all the sharp details and only retain the width as principal parameter. The assumptions in Fig. 6.5 about the distance to a nearest neighbour and the size of the cutoff are, to some degree, arbitrary. Nevertheless, this rough calculation shows how varying the ^{13}C spin density influences the resulting linewidth to

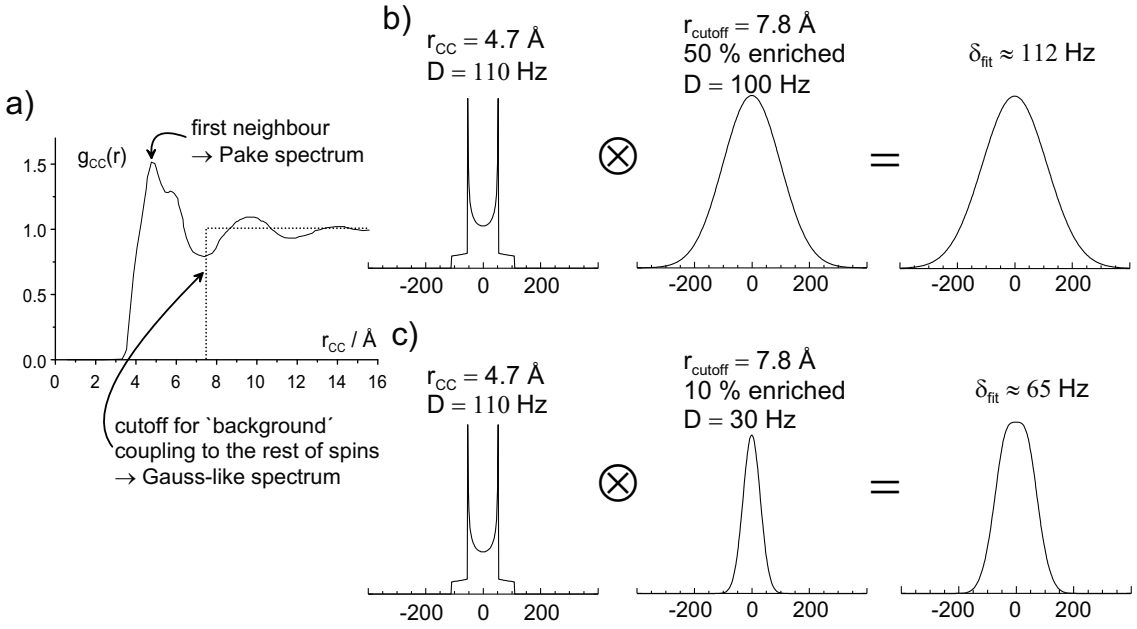

Figure 6.5: Diagrams illustrating the hierarchy of couplings resulting in the approximately Gaussian spectrum. Results of an MD study by Root and Berne [1997] (a) can be used to estimate the involved distance parameters. The nearest carbon at approximately 4.7 Å results in a Pake pattern of $D = 110$ Hz width. If the sample is 50 % enriched (b), a cutoff at 7.8 Å results in a Gauss-like distribution of 100 Hz spread (FWHM 235 Hz). However, the width is only 30 Hz (FWHM 70 Hz) for 10 % labelling (c). A frequency spread (or width) can be assigned to the convoluted spectra: 112 Hz (FWHM 264 Hz) for the 50 % sample and 65 Hz (FWHM 153 Hz) for the 10 % sample.

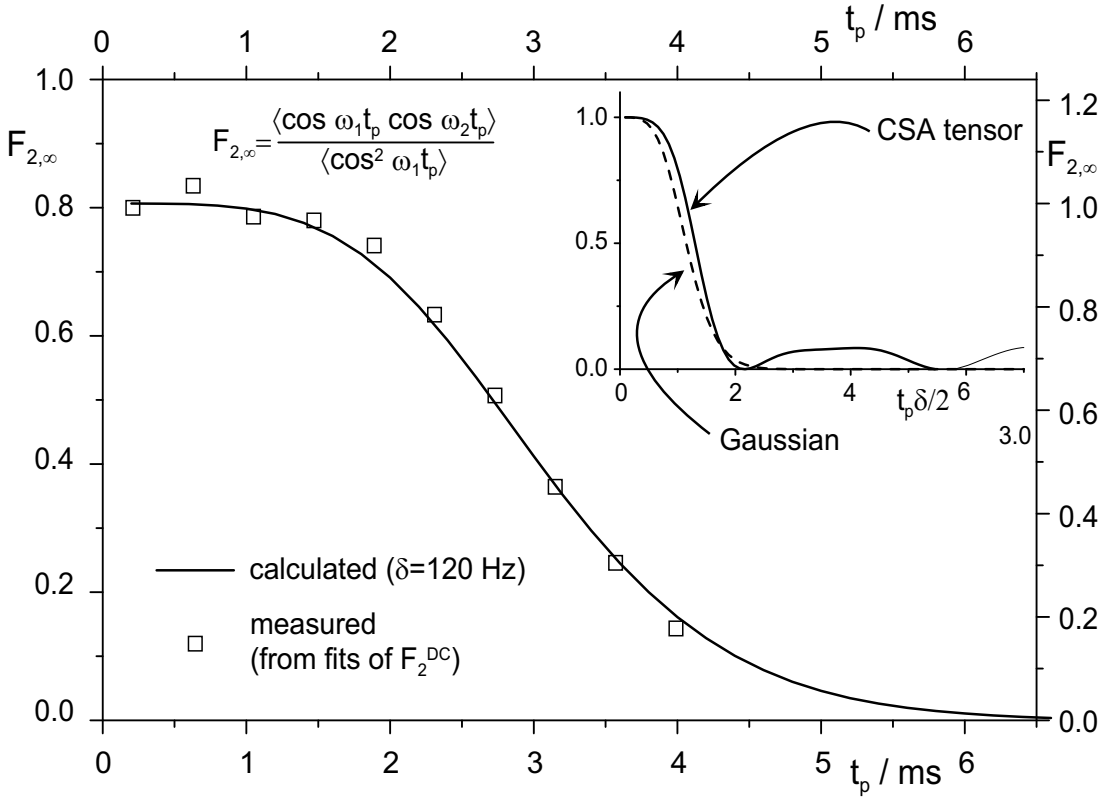

Figure 6.6: Plateau values, $F_{2,\infty}^{\mathrm{DC}}$, of the dipolar-correlation function F_2^{DC} as a function of evolution time, t_p, for glycerol at $T = 206$ K. The inset shows a calculated dependence of $F_{2,\infty}$ on a generalised geometric-sensitivity parameter $t_\mathrm{p}\delta$ for two scenarios. In the case of pure CSA interaction (anisotropy δ), the frequency distribution follows a CSA tensor. For dipolar multi-spin interactions, the frequency distribution is well approximated by a Gaussian distribution.

a non-trivial degree. A linear scaling of $D \propto \frac{1}{r^3} \propto \rho$ is not at all justified if carbons are not permitted to come within the minimum approach distance. If the first-neighbour shell contains, say, 6 molecules, it is very likely that at least one of them will contain a labelled ^{13}C spin. For this reason the short-distance contribution to the coupling constant is not strongly sensitive to spin density. The far-spin contribution will change by a factor slightly lower than the ratio of densities due to a minimum cutoff. In the given example, the coupling constant is tripled for a fivefold increase in density.

Let us now turn to the results obtained from dipolar-coupling experiments. The measured plateau values can be described by the general $F_{2,\infty}^{\mathrm{DC}}(t_\mathrm{p}\delta)$ curve if a dipolar-frequency spread of $\delta \approx 120$ Hz is assumed for the glycerol with 50 % labelled molecules as shown in Fig. 6.6. This is a remarkably good fit, which, however, should not be mistaken as a proof of a Gaussian distribution of the carbon resonance frequency, $p(\omega)$.

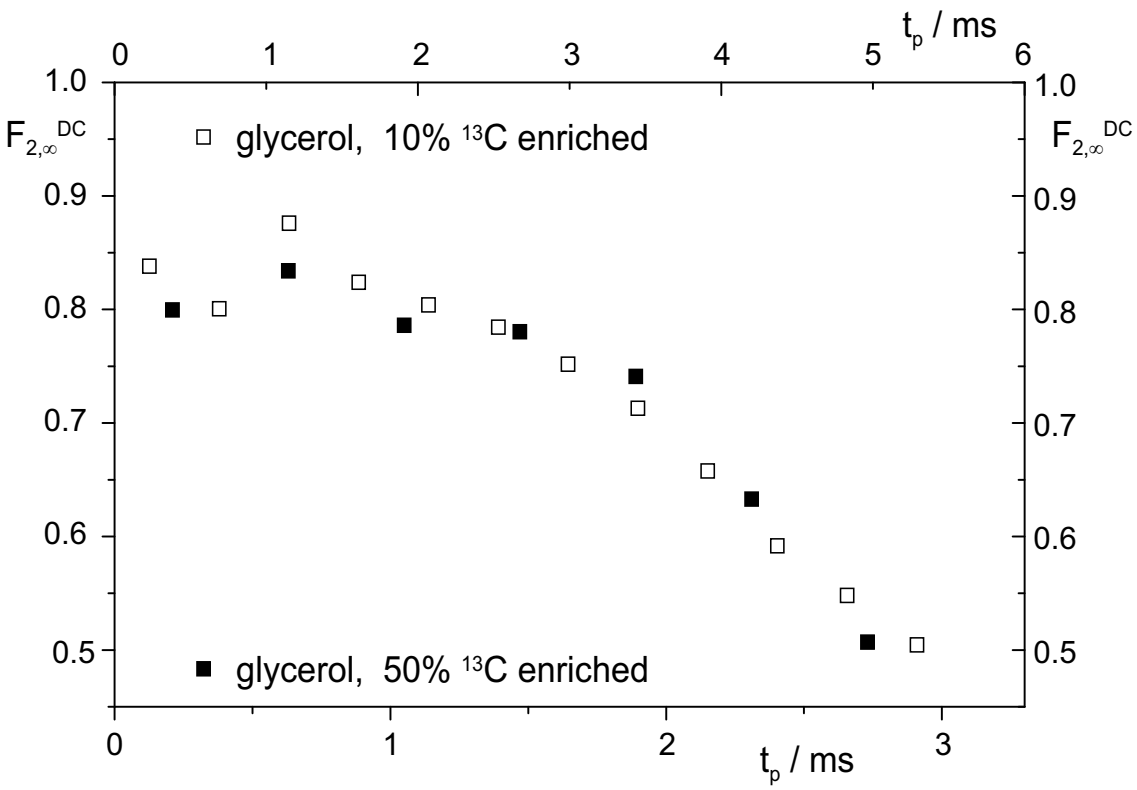

Figure 6.7: Plateau values, $F_{2,\infty}^{\mathrm{DC}}$, of the dipolar-correlation function F_2^{DC} as a function of evolution time, t_{p}, for glycerol. The data for 50 % enrichment (solid squares) as shown in Fig. 6.6 is plotted together with data for 10 % ^{13}C enrichment (open squares) vs. differently scaled t_{p} axis.

While the dependence of $F_{2,\infty}^{\mathrm{DC}}$ on t_{p} is fairly insensitive to the exact shape of the distribution, its width is of critical importance for the quality of the obtained fit. It is to be noted that we use the fit to extract the distribution width, δ, which is well-defined given the data we have. The direction of deduction could be inverted, i.e. deducing $p(\omega)$ from $F_{2,\infty}^{\mathrm{DC}}(t_{\mathrm{p}}\delta)$, provided we had plateau values at much better signal-to-noise ratios.

In Fig. 6.7 the t_{p} dependence of the plateau value for glycerol with two different levels of enrichment are compared. By scaling of t_{p} for the 50 % sample by a factor of 1.8, a match between the two curves was achieved. The sample with 10 % labelling has a dipolar-frequency spread reduced to $\delta \approx 65$ Hz as can be seen in Fig. 6.7 from the relative scaling of the abscissa by a factor of 1.8. This concentration dependence indicates that the 'anisotropy parameter' δ is dependent on the ^{13}C spin density. Thus, decays are essentially identical when plotted versus $t_{\mathrm{p}}\delta$. In Fig. 6.5 a rational is given of how this non-trivial scaling could arise. It is to be noted that the effective coupling is not

a result of a fit but rather obtained from known characteristics of the spin system, such as ^{13}C density, ^{13}C-^{13}C pair correlation function etc.

6.3 Decay Times and Their Dependence on Geometrical Sensitivity

The relationship between the measured decay time, τ, and the parameter of angular sensitivity, $t_\mathrm{p}\delta$, was extensively investigated in the study of rotational motional geometry for PVAc by Tracht et al. [1999b]. For diffusional, rotational motion it was found that the determined τ decreases with $(t_\mathrm{p}\delta)^{-2}$. For a finite jump-angle model, τ levels off at a certain value of $t_\mathrm{p}\delta$ and remains constant as t_p increases further. The measured correlation time τ is independent of t_p for a random-jump model. In a careful 2D deuteron NMR study by Böhmer and Hinze [1998], various jump models and the superposition of diffusion and moderately large-angle reorientation were studied. The rotational motion in glycerol was found to consist of small angle ($2 \ldots 3^\circ$) jumps plus a 2 % fraction of 30° jumps. The dependence of measured reorientation time, τ, on $t_\mathrm{p}\delta$ in glycerol can be approximated by a $(t_\mathrm{p}\delta)^{-1}$ dependence above $t_\mathrm{p}\delta \approx 7$. The rotational reorientation time τ decreases only marginally below $t_\mathrm{p}\delta \approx 7$.

Fig. 3.3 on page 46 demonstrates the general behaviour of $\tau(t_\mathrm{p}\delta)$ for diffusional and rotational motion about a fixed angle.

Fig. 6.8 shows the dependence of the correlation time extracted from the decay of F_2^DC curves on evolution time. Decay times could not be reliably fit for very short evolution times since the plateau values were too high to yield a well-defined decay. Fig. 6.8 starts at evolution times $t_\mathrm{p} = 1.8$ ms, a value beyond which decay times τ are well defined. As shown, the decay times remain constant over the investigated range of t_p. In analogy to the rotational motion investigated using the 2D echo experiment, this hints at a 'random-jump' motion. However, one should point out that the range of $t_\mathrm{p}\delta$ is not wide enough to positively assert this statement. As the dipolar coupling is dominated by the coupling to the carbon of a neighbouring glycerol molecule (strong r^{-3} dependence), the experiment essentially monitors the elemental diffusional step. A molecule leaving

the first-neighbour shell leads to a drastic change of the coupling; first-neighbour shell $\omega_{\mathrm{dip}}(4.7\,\text{Å}) = 110\,\mathrm{Hz}$ and second-neighbour shell $\omega_{\mathrm{dip}}(10\,\text{Å}) = 11\,\mathrm{Hz}$. Alternatively, one could consider the consequences for the 'dipolar environment' of the carbon in a glycerol molecule when this molecule moves into its neighbour shell. Not only will the ^{13}C spin 'see' a new spatial environment (angles and distances to the coupling spins will have changed) but also the spin state (up or down) of the new, most strongly coupled spin will be completely uncorrelated (ca. 50 % of the spins are in the up state). This effectively means that relaxation in the dipolar-correlation experiment occurs because the resonance frequency assumes randomly chosen values ω_{i} from a Gaussian distribution as presented above.

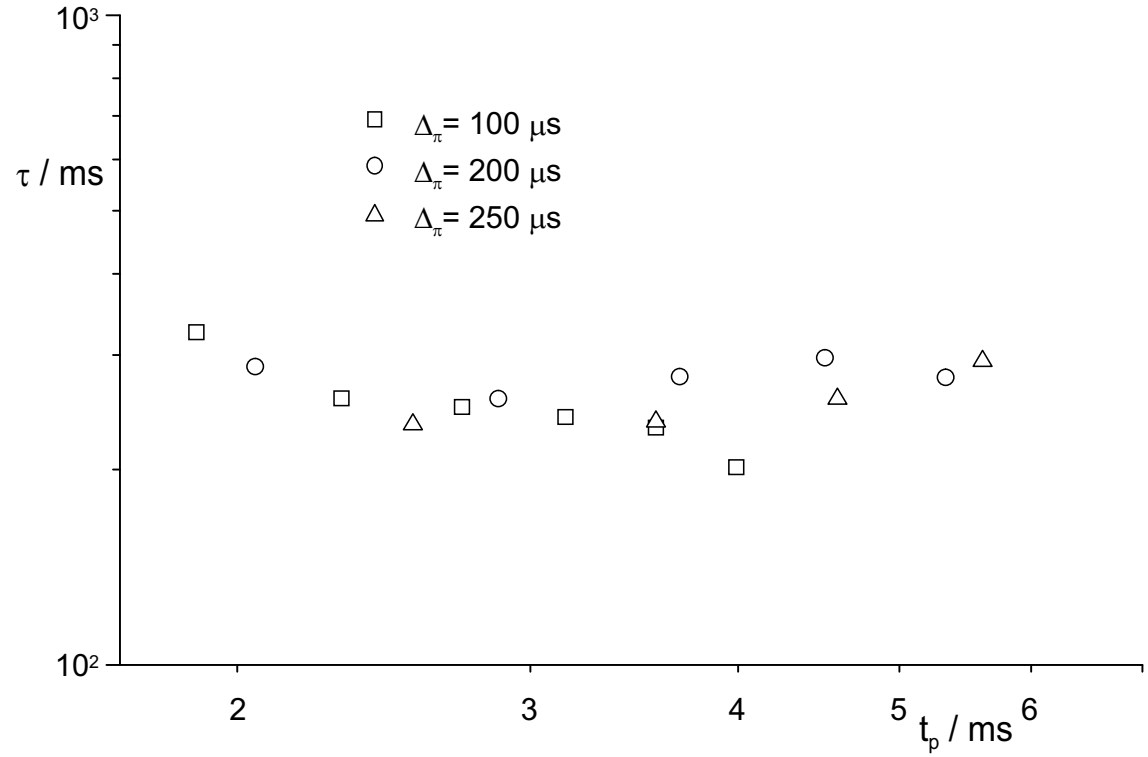

Figure 6.8: Decay times of dipolar-correlation functions F_2^{DC} as a function of evolution time, t_{p}, for 50 %-enriched glycerol. The symbols relate to three different π-pulse spacings, Δ_π.

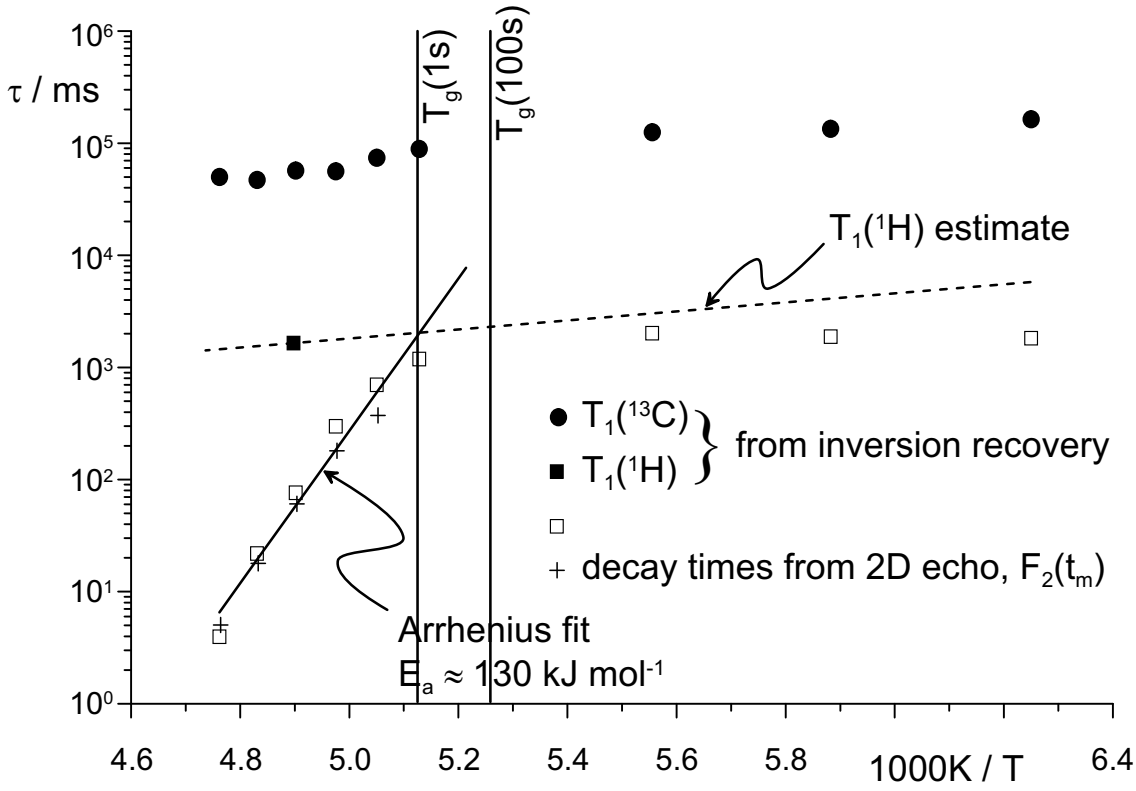

Figure 6.9: Decay times of dipolar-correlation functions F_2^{DC} as a function of temperature in an Arrhenius plot (□). The solid line indicates a fit to correlation times at higher temperatures yielding an activation energy of ca. 130 kJ/mol. The dashed line is an estimate of ^{1}H spin-lattice relaxation times. Correlation times of rotational relaxation by means of 2D-echo experiment (+) are shown for an evolution time $t_{\mathrm{p}} = 500\ \mu$s (discussion see text).

6.4 Temperature Dependence of Correlation Times

If the the rates of translational and rotational motion in a glass former are reflected in the decay times measured in the dipolar-correlation experiment, then the temperature dependence of these decay times will show a strong temperature dependence. If, on the other hand, a change in the spin state, e.g. spin diffusion or flip-flops of the spins that dominate the local dipolar coupling, dominate the decay of dipolar correlation, then the observed temperature dependence will be rather insignificant. To determine under what conditions which of the two reasons dominates the decay of F_2^{DC}, temperature-dependent studies of the decay times have been carried out.

Fig. 6.9 reveals that correlation times strongly depend on temperature above the glass transition $T_{\mathrm{g}} = 189$ K. Before discussing the temperature dependence of the transla-

tional dynamics we will look more closely at the interplay of spin-lattice relaxation and spin-state fluctuations. Fig. 6.9 also shows the spin-lattice relaxation times of ^{13}C as measured by inversion recovery after an initial ^{1}H$\rightarrow^{13}$C CP. These spin-lattice relaxation times are on the order of several tens to a hundred seconds with an insignificant temperature dependence. Proton spin-lattice relaxation times are much shorter at roughly 2 seconds. Recall that the samples contain paramagnetic relaxation agents (Cu^{2+}), which reduce $T_1(^1\mathrm{H})$ from minutes to seconds. Even though $T_1(^1\mathrm{H})$ was not measured, an estimate for its upper limit can be given based on the fact that the acquired NMR signal did not reduce when a transient delay of 2 s was used at all temperatures. The fast proton spin-lattice relaxation can be understood given the fast relaxation near the paramagnetic centres combined with an efficient ^{1}H spin diffusion owing to strong homonuclear ^{1}H dipolar coupling. Carbon spin-lattice relaxation, on the other hand, is likely to be slower. Carbons relax via the heteronuclear coupling to the much more abundant protons (dilution of 1:16 for the 50 % sample). This heteronuclear coupling is the bottleneck for ^{13}C spin-lattice relaxation rate.

Despite the rather long $T_1(^{13}\mathrm{C})$, we observe a considerably earlier decay of the dipolar-correlation function than carbon spin-lattice relaxation at temperatures below the glass transition. Clearly, motional relaxation can be ruled out at $T < T_\mathrm{g}$. Instead, spin-state fluctuations in the ^{13}C spin network dominate the decay rate of the dipolar-correlation function. To explain quicker loss of dipolar correlations compared to ^{13}C spin magnetisation M_z, we have to bear in mind the mechanisms leading to the two different relaxation processes. In the dipolar-correlation experiment, a spin state that evolved under influence of homonuclear dipolar coupling (protons are decoupled during this period) is saved by the application of a $\frac{\pi}{2}$ pulse. This 'dipolar-coded' spin state is fragile in that it is destroyed immediately if ^{13}C spin flips occur. These spin flips do not contribute to spin-lattice relaxation if they occur in a magnetisation-conserving manner (^{13}C flip-flops). The net ^{13}C magnetisation decay will only decay after a sufficient occurrence of non-conserving spin flips. The factor by which spin-lattice relaxation is slower can be estimated from the following facts. Carbon spin-lattice relaxation will be slower by a factor that describes the reduction in dipolar coupling of carbons to protons as compared to

protons coupling among themselves. This reduction factor is on the order of the relative dilution of ^{13}C with respect to ^{1}H, which is 1:16 in our 50 % enriched glycerol sample. On the other hand, to destroy the dipolar order associated with one carbon one only has to flip one member of a coupling entity to completely change the 'dipolar environment' experienced by the spin under scrutiny. For our sample we can assume that the first- and second-neighbour shells contain ^{13}C spins that form the dipolar coupling entity. Roughly 20 ^{13}C spins are part of such a two-shell coupling network. Since a correlation-destroying event is a single flip of any one spin in a two-shell coupling network, such an event will occur 20 times as often as a flipping event of a particular spin. Correspondingly, the time required to destroy the fragile dipolar state will be reduced by this factor as compared to the magnetisation-relaxation time which requires, on average, all spins to have flipped. The above-presented estimate shows: Firstly, carbon spin-lattice relaxation is slower by roughly one order of magnitude than proton spin-lattice relaxation. Secondly, carbon spin-state fluctuations are faster by an order of magnitude than carbon spin-lattice relaxation and hence happen on the same time scale as proton spin-lattice relaxation.

The Arrhenius fit to the data points leads to an activation energy of $E_{\mathrm{a}} \approx 130$ kJ/mol. Activation energies of this size for organic molecules are a strong indication of cooperative motion since bond energies in single, small, organic molecule are lower. It is interesting to compare this activation energy with an activation energy derived from viscosity measurements. Fig. 1.3 on page 8 shows the temperature dependence of the viscosity of glycerol. This data has been compiled by Ediger [1996]. From the slope of the viscosity one can estimate:

$$\frac{\mathrm{d}\log\eta}{\mathrm{d}\log\dfrac{T_{\mathrm{g}}}{T}} \approx 40 \tag{6.12}$$

and hence

$$\Delta\mathrm{E} \approx 40 \cdot \ln 10 \cdot RT_{\mathrm{g}} = 145 \text{ kJ/mol}. \tag{6.13}$$

This shows remarkable agreement of the two vastly different approaches to measuring diffusion. While viscosity represents an entirely macroscopic observable, dipolar-correlation decay times are a measure of local diffusivity.

Of course, one would expect correlation times to further increase beyond the glass transition and quickly diverge. However, ^{13}C spin-state fluctuations render experiments for these long relaxation times impossible.

Fig. 6.9 additionally shows correlation times obtained from 2D-echo experiments. These correlation times are signatures of rotational motion and depend strongly on the chosen evolution time t_p. Since the jump process is a superposition of diffusional motion and a few large-angle jumps as found by Böhmer and Hinze [1998] using deuteron NMR, it is not possible to ascribe a single characteristic time constant to the rotational process. The choice of $t_\mathrm{p} = 500\ \mu$s is arbitrary and a different evolution time would result in the rotational correlation times being scaled accordingly.

6.5 Summary

This chapter presents a new method of examining molecular dynamics. Many existing NMR techniques focus on measuring the rotational dynamics of single molecules or (for polymers) repeat units. The reason for this preference lies in the dominance of the chemical shift anisotropy over other interactions determining the resonance frequency. The dipolar-correlation experiment successfully eliminates the number-one interaction from the evolution period of a two-dimensional experiment. The remaining, dipolar interaction predominantly monitors distances and orientations *between* particles rather than the orientation of just *one* particle.

It is shown how the different features of the dipolar-correlation function F_2^DC arise. Its plateau value is successfully linked to spin density by invoking a model that considers a hierarchy of couplings. Strong nearest-neighbour couplings dominate the width of the coupling. The associated coupling strength does not, to a first approximation, scale linearly with density. The coupling to spins of the background scales in a non-trivial manner with density. The estimate for the effective dipolar coupling constant for the 10 % and 50 % ^{13}C-enriched sample nicely reproduces the values that can be extracted from dipolar-correlation experiments by comparing the decay of the plateau values with increasing $t_\mathrm{p}\delta$ to a decay calculated under the assumption of a Gaussian frequency dis-

tribution. As shown in the text, Gaussian distributions are an excellent assumption for the frequency distribution of ω with the most important feature being the width. The dependence of the plateau values on t_{p}, $F_{2,\infty}(t_{\mathrm{p}})$, scales linearly with the spread of the Gaussian distribution.

Since molecular motion as well as changes in the spin state can contribute to the decay in F_2^{DC}, special attention is paid to the importance of these two relaxation mechanisms at any given temperature. Below T_{g} spin-state fluctuations are faster than the frozen-in molecular motion. They occur at a rate faster than ^{13}C spin-lattice relaxation and are comparable to ^{1}H spin-lattice relaxation. An experiment comparing the sine to the cosine correlation function excludes single spin flips as a reason for the decay in F_2^{DC} (see Fig. 6.3). Rather, a collective change in the spin state of a coupling entity governs the decay. At temperatures above T_{g}, a strong temperature dependence of the decay times of the dipolar-correlation experiment is observed. It is faster than any spin-lattice relaxation or spin-state fluctuation. The activation energy of this motional process, 130 kJ/mol, is comparable to the value obtained for the activation energy of viscosity data.

In summary, we see the detected translational motion as a highly cooperative effect as witnessed by the high activation energies. As the dipolar coupling is dominated by the coupling to the neighbouring spin, the experiment monitors the elemental diffusion step.

It is tempting to make a comparison of the obtained result with the multitude of experimental evidence for the decoupling of translational and rotational motion. A variety of theoretical work corroborates these findings such as conclusions drawn from an environmental fluctuation model by Chang and Sillescu [1997] or the simulation of translational diffusion on a heterogeneous lattice by Cicerone et al. [1997]. However, one has to realise that it is not at all straightforward to derive a translational diffusion constant, D_{trans}, from the measured dipolar-correlation decay times. The translational diffusion constant measured by previous techniques reflects an average over a spatial range of up to 100 nm[Chang and Sillescu, 1997]. Dipolar correlation, on the other hand, as measured by the dipolar-correlation experiment is already lost after spins have separated by a very small distance (in the order of several Å).

Conclusion

The aim of the present thesis is to investigate spatial and temporal aspects of heterogeneous dynamics in model glass formers. Hereby, the emphasis is on the investigation of the slow, α relaxation dynamics above the glass transition T_{g}. Nuclear magnetic resonance reveals its unique versatility in the investigation of dynamics if the applied techniques and experiments are supported with simulations. This approach is adopted throughout this thesis.

A temporal aspect of the heterogeneous dynamics in glass formers, namely the concept denoted by rate memory, can be studied using multi-time correlation functions. Such four-time correlation functions were previously recorded for PVAc. These results are interpreted in conjunction with MC simulations of a variety of motional scenarios. For the rotational dynamics, it is shown that a superposition of large-angle jump motion and diffusional rotation best describe the observed results.

The spatial aspect of dynamic heterogeneities is investigated using a four-dimensional spin-diffusion technique (4D3CP) – an experiment that spatially correlates relaxation rates. This 4D3CP experiment has been used in a previous study of PVAc. A simulation of this experiment on a hard-sphere system establishes the following facts. The data-analysis procedure can be validated and further refined. In particular, the granularity effect of magnetisation-carrying spins that becomes relevant on the length scale of heterogeneities can be incorporated into the analysis scheme. This is done by the introduction of a gap, which reflects a nearest approach for carbon spins. Furthermore, slow domains as defined by a maximum nearest-neighbour change are visualised in the simulation. Their length scale from computer 4D3CP experiments is comparable to the one obtained from a different measure that analyses the pair-correlation function. The slow-

domain length scale is fairly insensitive to changes in the selection-level, a fact which allows a qualitative statement about the shape of domains to be made. We expect the domains to have a dendritic-like structure, or more generally, a high surface-to-volume ratio.

Glycerol and *o*-terphenyl are investigated by the 4D3CP experiment. These findings are compared to results previously published on the polymeric glass former PVAc. While PVAc and *o*-terphenyl exhibit a length scale of 3.7 nm and 2.9 nm, respectively, glycerol shows a significantly shorter length scale of only 1.1 nm. This coincides with a smaller stretching exponent β of the KWW relaxation function, i.e. wider relaxation-rate distribution, for both PVAc and *o*-terphenyl as compared to glycerol. The number of rearranging units (molecules for OTP and glycerol, and stiff polymer-chain elements for PVAc) in a box of the size of ξ_{het} is comparable for the two fragile glass formers while the intermediate glass former glycerol shows fewer molecules per ξ_{het}^3.

The temperature dependence of the length scale is studied for glycerol. Given the small accessible temperature window of 8 K and the relatively large experimental error, the power to prove certain temperature-dependence theories of cooperativity, e.g. the frustration-limited domain model or the dynamic scaling approach, is limited. Nevertheless, theories that predict a strong temperature dependence of ξ_{het} can be rejected on the grounds of a moderate variation in the length scale parameter for the three studied temperatures. In analogy to the simulations performed on hard-sphere systems, a selection-level dependence of the length-scale parameter in OTP is investigated for *o*-terphenyl. To establish the shape of the slow nanoregions, more data points at a higher signal-to-noise ratio would be desirable than are collected for this study. With the present amount of experimental and simulation data there is support, but no proof, for a conceptual depiction of slow domains as nanoregions of fractal-like shape.

Finally, a new experiment is proposed that is sensitive to translational motion in a glass former. By using a π-pulse train, a separation of evolution under the influence of chemical shift anisotropy and homonuclear dipolar coupling can be accomplished. Thus, it is possible to achieve the correlation of dipolar couplings before and after a mixing-time period (on the order of milliseconds to seconds). All the main features of the ob-

served dipolar-correlation decay are explained. The hierarchy of couplings is a successful concept for determining an efficient coupling constant and for explaining how this coupling constant scales with ^{13}C spin density, i.e. level of enrichment. The temperature dependence plays a key role in understanding the contributions to the loss of dipolar-correlation. At $T < T_{\mathrm{g}}$, spin-state fluctuations dominate the decay. At temperatures above the glass transition ($T > T_{\mathrm{g}}$), the detected correlation times clearly reflect translational motion. The observation of these correlation times is not obstructed by the much slower spin-state fluctuations. The activation energy found in the dipolar-correlation experiment ($\Delta E_{\mathrm{a}} \approx 130$ kJ/mol) agrees remarkably well with the activation energy former temperature-dependent studies of viscosity. The translational motion is not yet as quantitatively well defined as the much-studied geometry of rotational motion. With this new experiment at our disposal, further studies could reveal more information of the motional process.

Bibliography

A. Abragam. *The Principles of Nuclear Magnetism*. Oxford University Press, Oxford, 1^{st} edition, 1961.

G. Adam and J. H. Gibbs. On Temperature Dependence of Cooperative Relaxation Properties in Glass-Forming Liquids. *J. Chem. Phys.*, 43(1):139–143, 1965.

C. A. Angell. In K. L. Ngai and G. B. Wright, editors, *Relaxation in Complex Systems*, pages 3–11. Naval Res. Lab., 1984.

M. Arndt, R. Stannarius, W. Gorbatschow, and F. Kremer. Dielectric Investigations of the Dynamic Glass Transition in Nanopores. *Phys. Rev. E*, 54(5):5377–5390, 1996.

A. P. Bartko and R. M. Dickson. Three-Dimensional Orientations of Polymer-Bound Single Molecules. *J. Phys. Chem. B*, 103(16):3053–3056, 1999.

G. Barut, P. Pissis, R. Pelster, and G. Nimtz. Glass Transition in Liquids: Two Versus Three-Dimensional Confinement. *Phys. Rev. Lett.*, 80(16):3543–3546, 1998.

A. D. Becke. Density-Functional Exchange-Energy Approximation with Correct Asymptotic-Behavior. *Phys. Rev. A*, 38(6):3098–3100, 1988.

M. Beiner, H. Huth, and K. Schröter. Crossover Region of Dynamic Glass Transition: General Trends and Individual Aspects. *J. Non-Cryst. Solids*, 279(2-3):126–135, 2001.

U. Bengtzelius, W. Götze, and A. Sjölander. Dynamics of Supercooled Liquids and the Glass-Transition. *J. Phys. C*, 17(33):5915–5934, 1984.

R. Böhmer, R. V. Chamberlin, G. Diezemann, B. Geil, A. Heuer, G. Hinze, S. C. Kuebler, R. Richert, B. Schiener, H. Sillescu H. W. Spiess, U. Tracht, and M. Wilhelm. Nature of the Non-Exponential Primary Relaxation in Structural Glass-Formers Probed by Dynamically Selective Experiments. *J. Non-Cryst. Solids*, 235(13):1–9, 1998a.

R. Böhmer, G. Diezemann, G. Hinze, and H. Sillescu. A Nuclear Magnetic Resonance Study of Higher-Order Correlation Functions in Supercooled Ortho-Terphenyl. *J. Chem. Phys.*, 108(3):890–899, 1998b.

R. Böhmer and G. Hinze. Reorientations in Supercooled Glycerol Studied by Two Dimensional Time-Domain Deuteron Nuclear Magnetic Resonance Spectroscopy. *J. Chem. Phys.*, 109(1):241–248, 1998.

R. Böhmer, G. Hinze, G. Diezemann, B. Geil, and H. Sillescu. Dynamic Heterogeneity in Supercooled Ortho-Terphenyl Studied by Multidimensional Deuteron NMR. *Europhys. Lett.*, 36(1):55–60, 1996.

R. Böhmer, K. L. Ngai, C. A. Angell, and D. J. Plazek. Nonexponential Relaxations in Strong and Fragile Glass Formers. *J. Chem. Phys.*, 99(5):4201–4209, 1993.

U. Buchenau, Y. M. Galperin, V. L. Gurevich, D. A. Parshin, M. A. Ramos, and H. R. Schober. Interaction of Soft Modes and Sound-Waves in Glasses. *Phys. Rev. B*, 46(5): 2798–2808, 1992.

I. Campbell, P.-O. Mari, A. Alegría, and J. Colmenero. A Random Walk in Search of the Glass Transition. *Europhysics News*, (5206):46–50, 1998.

H. Y. Carr and E. M. Purcell. Effects of Diffusion on Free Precession in Nuclear Magnetic Resonance Experiments. *Phys. Rev.*, 94(3):630–638, 1954.

R. V. Chamberlin and R. Richert. Comment on "Hole-Burning Experiments Within Glassy Models with Infinite Range Interactions". *Phys. Rev. Lett.*, 87(12):9601, 2001.

D. Champion, H. Hervet, G. Blond, M. Lemeste, and D. Simatos. Translational Diffusion in Sucrose Solutions in the Vicinity of Their Glass Transition Temperature. *J. Phys. Chem. B*, 101(50):10674–10679, 1997.

I. Chang, F. Fujara, B. Geil, G. Heuberger, T. Mangel, and H. Sillescu. Translational and Rotational Molecular-Motion in Supercooled Liquids Studied by NMR and Forced Rayleigh-Scattering. *J. Non-Cryst. Solids*, 172:248–255, 1994.

I. Chang and H. Sillescu. Heterogeneity at the Glass Transition: Translational and Rotational Self-Diffusion. *J. Phys. Chem. B*, 101(43):8794–8801, 1997.

M. T. Cicerone, F. R. Blackburn, and M. D. Ediger. Anomalous Diffusion of Probe Molecules in Polystyrene Evidence for Spatially Heterogeneous Segmental Dynamics. *Macromolecules*, 28(24):8224–8232, 1995a.

M. T. Cicerone, F. R. Blackburn, and M. D. Ediger. How Do Molecules Move near T_g? Molecular Rotation of 6 Probes in O-Terphenyl Across 14 Decades in Time. *J. Chem. Phys.*, 102(1):471–479, 1995b.

M. T. Cicerone and M. D. Ediger. Photobleaching Technique for Measuring Ultraslow Reorientation near and Below the Glass-Transition Tetracene in O-Terphenyl. *J. Phys. Chem.*, 97(40):10489–10497, 1993.

M. T. Cicerone and M. D. Ediger. Relaxation of Spatially Heterogeneous Dynamic Domains in Supercooled Ortho-Terphenyl. *J. Chem. Phys.*, 103(13):5684–5692, 1995.

M. T. Cicerone, P. A. Wagner, and M. D. Ediger. Translational Diffusion on Heterogeneous Lattices: A Model for Dynamics in Glass Forming Materials. *J. Phys. Chem. B*, 101(43):8727–8734, 1997.

R. H. Colby. Dynamic Scaling Approach to Glass Formation. *Phys. Rev. E*, 61(2):1783–1792, 2000.

L. F. Cugliandolo and J. L. Iguain. Hole-Burning Experiments Within Glassy Models with Infinite Range Interactions. *Phys. Rev. Lett.*, 85(16):3448–3451, 2000.

E. R. deAzevedo, W. G. Hu, T. J. Bonagamba, and K. Schmidt-Rohr. Centerband-Only Detection of Exchange: Efficient Analysis of Dynamics in Solids by NMR. *J. Am. Chem. Soc.*, 121(36):8411–8412, 1999.

D. E. Demco, J. Tegenfeldt, and J. S. Waugh. Dynamics of Cross relaxation in Nuclear Magnetic Double Resonance. *Physical Review B*, 11(11):4133–4151, 1975.

G. Diezemann and R. Böhmer. Comment on "Hole-Burning Experiments Within Glassy Models with Infinite Range Interactions". *Phys. Rev. Lett.*, 87(12):9602, 2001.

G. Diezemann, H. Sillescu, G. Hinze, and R. Böhmer. Rotational Correlation Functions and Apparently Enhanced Translational Diffusion in a Free-Energy Landscape Model for the Alpha Relaxation in Glass-Forming Liquids. *Phys. Rev. E*, 57(4):4398–4410, 1998.

B. Doliwa and A. Heuer. Cooperativity and Spatial Correlations near the Glass Transition: Computer Simulation Results for Hard Spheres and Disks. *Phys. Rev. E*, 61(6): 6898–6908, 2000.

C. Donati, S. C. Glotzer, and P. H. Poole. Growing Spatial Correlations of Particle Displacements in a Simulated Liquid on Cooling Toward the Glass Transition. *Phys. Rev. Lett.*, 82(25):5064–5067, 1999.

E. Donth. The Size of Cooperatively Rearranging Regions at the Glass Transition. *J. Non-Cryst. Solids*, 53(3):325–330, 1982.

E. Donth, H. Huth, and M. Beiner. Characteristic Length of the Glass Transition. *J. Phys.-Condes. Matter*, 13(22):L451–L462, 2001.

T. Dries, F. Fujara, M. Kiebel, E. Rossler, and H. Sillescu. H-2-NMR Study of the Glass-Transition in Supercooled Ortho Terphenyl. *J. Chem. Phys.*, 88(4):2139–2147, 1988.

M. D. Ediger. Supercooled Liquids and Glasses. *J. Phys. Chem.*, 100(31):13200–13212, 1996.

M. D. Ediger. Materials Science Movies of the Glass Transition. *Science*, 287(5453): 604–605, 2000a.

M. D. Ediger. Spatially Heterogeneous Dynamics in Supercooled Liquids. *Annu. Rev. Phys. Chem.*, 51:99–128, 2000b.

B. M. Erwin and R. H. Colby. Temperature Dependences of Viscosity and the Length Scale of Cooperative Motion for Glass-Forming Liquids. *submitted to J. Non-Cryst. Solids*, 1(1):1, 2001.

H. Eyring. *J. Chem. Phys.*, 4:283, 1936.

M. Feike, D. E. Demco, R. Graf, J. Gottwald, S. Hafner, and H. W. Spiess. Broadband Multiple-Quantum NMR Spectroscopy. *J. Magn. Reson. Ser. A*, 122(2):214–221, 1996.

J. P. Flory. *Statistical Mechanics of Chain Molecules*. Interscience Publishers, John Wiley & Sons, New York, 1^{st} edition, 1969.

K. C. Fox. Biopreservation Putting Proteins Under Glass. *Science*, 267(5206):1922–1923, 1995.

T. Franosch, W. Gotze, M. R. Mayr, and A. P. Singh. Evolution of Structural Relaxation Spectra of Glycerol Within the Gigahertz Band. *Phys. Rev. E*, 55(3):3183–3190, 1997.

B. Frick and D. Richter. The Microscopic Basis of the Glass-Transition in Polymers from Neutron-Scattering Studies. *Science*, 267(5206):1939–1945, 1995.

F. Fujara, B. Geil, H. Sillescu, and G. Fleischer. Translational and Rotational Diffusion in Supercooled Orthoterphenyl Close to the Glass-Transition. *Z. Phys. B-Condens. Mat.*, 88(2):195–204, 1992.

G. Fytas, C. H. Wang, D. Lilge, and T. Dorfmuller. Homodyne Light Beating Spectroscopy of Ortho-Terphenyl in the Supercooled Liquid-State. *J. Chem. Phys.*, 75(9): 4247–4255, 1981.

Gaussian 98, Revision A.7, M. J. Frisch, G. W. Trucks, H. B. Schlegel, G. E. Scuseria, M. A. Robb, J. R. Cheeseman, V. G. Zakrzewski, J. A. Montgomery, Jr., R. E. Stratmann, J. C. Burant, S. Dapprich, J. M. Millam, A. D. Daniels, K. N. Kudin, M. C. Strain, O. Farkas, J. Tomasi, V. Barone, M. Cossi, R. Cammi, B. Mennucci, C. Pomelli, C. Adamo, S. Clifford, J. Ochterski, G. A. Petersson, P. Y. Ayala, Q. Cui, K. Morokuma, D. K. Malick, A. D. Rabuck, K. Raghavachari, J. B. Foresman, J. Cioslowski, J. V. Ortiz, A. G. Baboul, B. B. Stefanov, G. Liu, A. Liashenko, P. Piskorz, I. Komaromi, R. Gomperts, R. L. Martin, D. J. Fox, T. Keith, M. A. Al-Laham, C. Y. Peng, A. Nanayakkara, C. Gonzalez, M. Challacombe, P. M. W. Gill, B. Johnson, W. Chen, M. W. Wong, J. L. Andres, C. Gonzalez, M. Head-Gordon, E. S. Replogle, and J. A. Pople, Gaussian, Inc., Pittsburgh PA, 1998.

H. Geen, J. J. Titman, J. Gottwald, and H. W. Spiess. Spinning Side-Band in the Fast-Mas Multiple-Quantum Spectra of Protons in Solids. *J. Magn. Reson. Ser. A*, 114(2): 264–267, 1995.

B. Geil, F. Fujara, and H. Sillescu. H-2 NMR Time Domain Analysis of Ultraslow Reorientations in Supercooled Liquids. *J. Magn. Reson.*, 130(1):18–26, 1998.

J. Gottwald. *Hochaufgelöste Multiquanten-NMR-Spektroskopie von Festkörpern*. PhD thesis, Johannes Gutenberg-Universität Mainz, 1996.

R. Graf, D. E. Demco, J. Gottwald, S. Hafner, and H. W. Spiess. Dipolar Couplings and Internuclear Distances by Double-Quantum Nuclear Magnetic Resonance Spectroscopy of Solids. *J. Chem. Phys.*, 106(3):885–895, 1997.

D. M. Grant and R. K. Harris. *Encyclopedia of Nuclear Magnetic Resonance*, volume I to VIII. John Wiley & Sons, 1^{st} edition, 1996.

T. Gullion and J. Schaefer. Rotational-Echo Double-Resonance NMR. *J. Magn. Reson. Ser. A*, 81(1):196–200, 1989.

T. Ha, T. A. Laurence, D. S. Chemla, and S. Weiss. Polarization Spectroscopy of Single Fluorescent Molecules. *J. Phys. Chem. B*, 103(33):6839–6850, 1999.

U. Haeberlen. High Resolution NMR in Solids. In J.S. Waugh, editor, *Advances in Magnetic Resonance*, volume 1, page 85. Academic Press, New York, San Francisco, London, 1^{st} edition, 1976.

A. Hagemeyer, K. Schmidt-Rohr, and H. W. Spiess. Two-Dimensional Nuclear Magnetic Resonance Experiments for Studying Molecular Order and Dynamics in Static and Rotating Solids. In *Advances in Magnetic Resonance*, volume 13. Academic Press, 1^{st} edition, 1998.

S.R. Hartmann and E.L. Hahn. Nuclear Double Resonance in the Rotating Frame. *Physical Review*, 128(5):2042–2053, 1962.

P. Hazendonk, R. K. Harris, G. Galli, and S. Pizzanelli. Cross-Polarization for a Fluoropolymer Involving Multiple Spin Baths of Abundant Nuclei. *submitted to Physical Chemistry Chemical Physics*, 2001.

E. Hempel, G. Hempel, A. Hensel, C. Schick, and E. Donth. Characteristic Length of Dynamic Glass Transition near T_g for a Wide Assortment of Glass-Forming Substances. *J. Phys. Chem. B*, 104(11):2460–2466, 2000.

A. Heuer. Information Content of Multitime Correlation Functions for the Interpretation of Structural Relaxation in Glass-Forming Systems. *Phys. Rev. E*, 56(1):730–740, 1997.

A. Heuer, J. Leisen, S. C. Kuebler, and H. W. Spiess. Geometry and Time Scale of the Complex Rotational Dynamics of Amorphous Polymers at the Glass Transition by Multidimensional Nuclear Magnetic Resonance. *J. Chem. Phys.*, 105(16):7088–7096, 1996.

A. Heuer, M. Wilhelm, H. Zimmermann, and H. W. Spiess. Rate Memory of Structural Relaxation in Glasses and Its Detection by Multidimensional NMR. *Phys. Rev. Lett.*, 75(15):2851–2854, 1995.

G. Hinze, G. Diezemann, and H. Sillescu. Four-Time Rotational Correlation Functions. *Europhys. Lett.*, 44(5):565–570, 1998.

P. J. Hore, J. A. Jones, and S. Wimperis. *NMR: The Toolkit*. Oxford University Press, 1^{st} edition, 2000.

J. Jeener and P. Broekaer. Nuclear Magnetic Resonance in Solids Thermodynamic Effects of a Pair of RF Pulses. *Phys. Rev.*, 157(2):232, 1967.

G. P. Johari. A Resolution for the Enigma of a Liquid's Configurational Entropy-Molecular Kinetics Relation. *J. Chem. Phys.*, 112(20):8958–8969, 2000.

G. P. Johari and M. Goldstein. Molecular Mobility in Simple Glasses. *J. Phys. Chem.*, 74(9):2034, 1970.

J. L. Keddie, R. A. L. Jones, and R. A. Cory. Size-Dependent Depression of the Glass-Transition Temperature in Polymer-Films. *Europhys. Lett.*, 27(1):59–64, 1994.

T. A. Keith and R. F. W. Bader. Calculation of Magnetic Response Properties Using a Continuous Set of Gauge Transformations. *Chem. Phys. Lett.*, 210(1-3):223–231, 1993.

S. A. Kivelson, X. L. Zhao, D. Kivelson, T. M. Fischer, and C. M. Knobler. Frustration-Limited Clusters in Liquids. *J. Chem. Phys.*, 101(3):2391–2397, 1994.

J. Korus, E. Hempel, M. Beiner, S. Kahle, and E. Donth. Temperature Dependence of Alpha Glass Transition Cooperativity. *Acta Polym.*, 48(9):369–378, 1997.

F. Kremer, A. Huwe, M. Arndt, P. Behrens, and W. Schwieger. How Many Molecules Form a Liquid? *J. Phys.-Condes. Matter*, 11(10A):A175–A188, 1999.

C. T. Lee, W. T. Yang, and R. G. Parr. Development of the Colle-Salvetti Correlation-Energy Formula into a Functional of the Electron-Density. *Phys. Rev. B*, 37(2):785–789, 1988.

R. L. Leheny, N. Menon, S. R. Nagel, D. L. Price, K. Suzuya, and P. Thiyagarajan. Structural Studies of an Organic Liquid Through the Glass Transition. *J. Chem. Phys.*, 105(17):7783–7794, 1996.

E. Leutheusser. Dynamical Model of the Liquid-Glass Transition. *Phys. Rev. A*, 29(5): 2765–2773, 1984.

K. L. Li, A. A. Jones, P. T. Inglefield, and A. D. English. Domain Size of Dynamic Heterogeneities just Above the Glass Transition in an Amorphous Polycarbonate. *Macromolecules*, 22(11):4198–4204, 1989.

I. J. Lowe and S. Gade. Density-Matrix Derivation of Spin-Diffusion Equation. *Phys. Rev.*, 156(3):817, 1967.

J.V. McBrierty and J.P. Packer. In E.A. Davies and I.M. Ward, editors, *Nuclear Magnetic Resonance in Solid Polymers*. Cambridge University Press, 1^{st} edition, 1993.

M. Mehring. *Principles of High Resolution NMR in Solids*. Springer-Verlag, 2^{nd} edition, 1983.

H. Mori and K. Kawasaki. Theory of Dynamical Behaviors of Ferromagnetic Spins. *Prog. Theor. Phys.*, 27(3):529–570, 1962.

S. Mossa, R. di Leonardo, G. Ruocco, and M. Sampoli. Molecular Dynamics Simulation of the Fragile Glass-Former Orthoterphenyl: A Flexible Molecule Model. *Phys. Rev. E*, 62(1):612–630, 2000.

H. M. Pastawski, P. R. Levstein, and G. Usaj. Quantum Dynamical Echoes in the Spin-Diffusion in Mesoscopic Systems. *Phys. Rev. Lett.*, 75(23):4310–4313, 1995.

D. J. Plazek. Temperature Dependence of Viscoelastic Behavior of Polystyrene. *J. Phys. Chem.*, 69(10):3480, 1965.

W. H. Press, S. A. Teukolsky, W. T. Vetterling, and B.P. Flannery. *Numerical Recipes in C: The Art of Scientific Computing*. Academic Press, London, 2^{nd} edition, 1992.

A. G. Redfield and S. D. Kunz. Quadrature Fourier NMR Detection Simple Multiplex for Dual Detection and Discussion. *J. Magn. Reson.*, 19(2):250–254, 1975.

S. A. Reinsberg. Density-Matrix Formalism. MS PowerPoint© presentation, 2000.

S. A. Reinsberg, S. Ando, and R. K. Harris. Fluorine-19 NMR Investigation of Poly(trifluoroethylene). *Polymer*, 41(10):3729–3736, 2000.

S. A. Reinsberg, A. Heuer, B. Doliwa, H. Zimmermann, and H. W. Spiess. Comparative Study of the Length Scale of Dynamic Heterogeneity of Three Different Glass Formers. *J. Non.-Cryst. Solids*, in press, 2002.

S. A. Reinsberg, X. H. Qiu, M. Wilhelm, H. W. Spiess, and M. D. Ediger. Length Scale of Dynamic Heterogeneity in Supercooled Glycerol near T_g. *J. Chem. Phys.*, 114(17): 7299–7302, 2001.

S.A. Reinsberg. NMR Studies of Fluoropolymers and of Polyaniline. Master's thesis, University of Durham, 1998.

R. Richert. Evidence for Dynamic Heterogeneity near T_g from the Time Resolved Inhomogeneous Broadening of Optical Line Shapes. *J. Phys. Chem. B*, 101(33):6323–6326, 1997.

R. Richert. Scaling vs. Vogel-Fulcher-Type Structural Relaxation in Deeply Supercooled Materials. *Physica A*, 287(1-2):26–36, 2000.

A. K. Rizos and K. L. Ngai. Experimental Determination of the Cooperative Length Scale of a Glass-Forming Liquid near the Glass Transition Temperature. *Phys. Rev. E*, 59(1):612–617, 1999.

L. J. Root and B. J. Berne. Effect of Pressure on Hydrogen Bonding in Glycerol: a Molecular Dynamics Investigation. *J. Chem. Phys.*, 107(11):4350–4357, 1997.

L. J. Root and F. H. Stillinger. Short-Range Order in Glycerol a Molecular-Dynamics Study. *J. Chem. Phys.*, 90(2):1200–1208, 1989.

E. V. Russell, N. E. Israeloff, L. E. Walther, and H. A. Gomariz. Nanometer Scale Dielectric Fluctuations at the Glass Transition. *Phys. Rev. Lett.*, 81(7):1461–1464, 1998.

K. Saalwächter. *Heteronuclear Recoupling Methods in Solid-State NMR*. PhD thesis, Johannes Gutenberg-Universität Mainz, 2000.

B. Schiener, R. Böhmer, A. Loidl, and R. V. Chamberlin. Nonresonant Spectral Hole Burning in the Slow Dielectric Response of Supercooled Liquids. *Science*, 274(5288): 752–754, 1996.

B. Schiener, R. V. Chamberlin, G. Diezemann, and R. Böhmer. Nonresonant Dielectric Hole Burning Spectroscopy of Supercooled Liquids. *J. Chem. Phys.*, 107(19):7746–7761, 1997.

W. Schirmacher, G. Diezemann, and C. Ganter. Harmonic Vibrational Excitations in Disordered Solids and the "Boson Peak". *Phys. Rev. Lett.*, 81(1):136–139, 1998.

C. Schmidt, B. Blümich, and H. W. Spiess. Deuteron Two-Dimensional Exchange NMR in Solids. *J. Magn. Reson.*, 79(2):269–290, 1988.

C. Schmidt, S. Wefing, B. Blumich, and H. W. Spiess. Dynamics of Molecular Reorientations Direct Determination of Rotational Angles from Two-Dimensional NMR of Powders. *Chem. Phys. Lett.*, 130(1-2):84–90, 1986.

K. Schmidt-Rohr and H. W. Spiess. Nature of Nonexponential Loss of Correlation Above the Glass Transition Investigated by Multidimensional NMR. *Phys. Rev. Lett.*, 66(23): 3020–3023, 1991.

K. Schmidt-Rohr and H. W. Spiess. *Multidimensional Solid-State NMR and Polymers*. Academic Press, London, 1^{st} edition, 1994.

W. Schnauss, F. Fujara, K. Hartmann, and H. Sillescu. Nonexponential H-2 Spin-Lattice Relaxation as a Signature of the Glassy State. *Chem. Phys. Lett.*, 166(4):381–384, 1990.

I. Schnell and H. W. Spiess. High-Resolution H-1 NMR Spectroscopy in the Solid State: Very Fast Sample Rotation and Multiple-Quantum Coherences. *J. Magn. Reson.*, 151 (2):153–227, 2001.

H. Sillescu. Multidimensional Nuclear Magnetic Resonance in Complex Liquids Analyzed by a Simple Model for Non-Markovian Molecular Reorientation. *J. Chem. Phys.*, 104(13):4877–4886, 1996.

H. Sillescu. Heterogeneity at the Glass Transition: A Review. *J. Non-Cryst. Solids*, 243 (2-3):81–108, 1999.

C.P. Slichter. *Principles of Magnetic Resonance*. Springer-Verlag, Berlin, Heidelberg, New York, 3^{rd} edition, 1990.

A. P. Sokolov, A. Kisliuk, M. Soltwisch, and D. Quitmann. Medium-Range Order in Glasses Comparison of Raman and Diffraction Measurements. *Phys. Rev. Lett.*, 69 (10):1540–1543, 1992.

H. W. Spiess. Rotation of Molecules and Nuclear Spin Relaxation. In P. Diehl, E. Fluck, and R. Kosfeld, editors, *NMR – Basic Principles and Progress*, volume 15. Springer, 1^{st} edition, 1978.

H. W. Spiess. Deuteron Spin Alignment a Probe for Studying Ultraslow Motions in Solids and Solid Polymers. *J. Chem. Phys.*, 72(12):6755–6762, 1980.

D. J. States, R. A. Haberkorn, and D. J. Ruben. A Two-Dimensional Nuclear Overhauser Experiment with Pure Absorption Phase in 4 Quadrants. *J. Magn. Reson.*, 48(2):286–292, 1982.

E.O. Stejskal and J.D. Memory. *High Resolution NMR in the Solid State*. Oxford University Press, 1^{st} edition, 1994.

F. H. Stillinger. Relaxation and Flow Mechanisms in Fragile Glass-Forming Liquids. *J. Chem. Phys.*, 89(10):6461–6469, 1988.

M. Stumber, H. Zimmermann, H. Schmitt, and U. Haeberlen. O-Terphenyl: Flips of the End Rings in the Crystal Phase. *Mol. Phys.*, 99(13):1091–1098, 2001.

M. Tomaselli, S. Hediger, D. Suter, and R. R. Ernst. Nuclear Magnetic Resonance Polarization and Coherence Echoes in Static and Rotating Solids. *J. Chem. Phys.*, 105(24): 10672–10681, 1996.

U. Tracht. *Dynamische Heterogenitäten am Glasübergang: Mehrdimensionale Festkörper-NMR-Spektroskopie an Polymeren*. PhD thesis, Johannes Gutenberg-Universität Mainz, 1998.

U. Tracht, A. Heuer, S. A. Reinsberg, and H. W. Spiess. The Rate Memory of a Polymer Close to T_g as Elucidated by Reduced 4-D NMR Echo Experiments. *Appl. Magn. Reson.*, 17(2-3):227–241, 1999a.

U. Tracht, A. Heuer, and H. W. Spiess. Geometry of Reorientational Dynamics in Supercooled Poly(vinyl Acetate) Studied by C-13 Two-Dimensional Nuclear Magnetic Resonance Echo Experiments. *J. Chem. Phys.*, 111(8):3720–3727, 1999b.

U. Tracht, H. Wilhelm, A. Heuer, and H. W. Spiess. Combined Reduced 4D C-13 Exchange and H-1 Spin Diffusion Experiment for Determining the Length Scale of Dynamic Heterogeneities. *J. Magn. Reson.*, 140(2):460–470, 1999c.

U. Tracht, M. Wilhelm, A. Heuer, H. Feng, K. Schmidt-Rohr, and H. W. Spiess. Length Scale of Dynamic Heterogeneities at the Glass Transition Determined by Multidimensional Nuclear Magnetic Resonance. *Phys. Rev. Lett.*, 81(13):2727–2730, 1998.

M. Ueda and K. Kajitani. Dilute Solution Properties of Poly(vinyl acetate) .i. Molecular Weitht Dependence of Limiting Viscosity Number in a Few Solvents. *Makromolekul. Chem.*, 108(OCT):138, 1967.

P. Viot, G. Tarjus, and D. Kivelson. A Heterogeneous Picture of Alpha Relaxation for Fragile Supercooled Liquids. *J. Chem. Phys.*, 112(23):10368–10378, 2000.

C. Y. Wang and M. D. Ediger. Lifetime of Spatially Heterogeneous Dynamic Domains in Polystyrene Melts. *J. Chem. Phys.*, 112(15):6933–6937, 2000.

R. Yamamoto and A. Onuki. Dynamics of Highly Supercooled Liquids: Heterogeneity, Rheology, and Diffusion. *Phys. Rev. E*, 58(3):3515–3529, 1998.

O. Yamamuro, I. Tsukushi, A. Lindqvist, S. Takahara, M. Ishikawa, and T. Matsuo. Calorimetric Study of Glassy and Liquid Toluene and Ethylbenzene: Thermodynamic Approach to Spatial Heterogeneity in Glass-Forming Molecular Liquids. *J. Phys. Chem. B*, 102(9):1605–1609, 1998.

Y. Yang, A. Hagemeyer, and H. W. Spiess. Order-Exchange Correlated Two-Dimensional NMR-Study of Slow Molecular-Motion in Highly Oriented Crystalline Poly(oxymethylene). *Macromolecules*, 22(2):1004–1006, 1989.

S. Zhang, B. H. Meier, and R. R. Ernst. Polarization Echoes in NMR. *Phys. Rev. Lett.*, 69(14):2149–2151, 1992.

Appendix A

Technicalities of Simulations

A.1 Reorientation of a Tensor

In Chapter 3 and 4 simulations of rotational motion of molecules have been performed. Reorientation of molecular entities in NMR results in a change of orientation of a tensor. Frequently a jump process of the sketched kind (see Fig. A.1) is assumed. A jump about a given angle α is performed. This angle defines a circle on the surface of a sphere. The jump destination becomes unique if one further angle, γ, is introduced describing the azimuth of the jump destination. In Cartesian coordinates, the tensor undergoes the transformation $(x, y, z) \rightarrow (x', y', z')$. The relationship between Cartesian and of polar

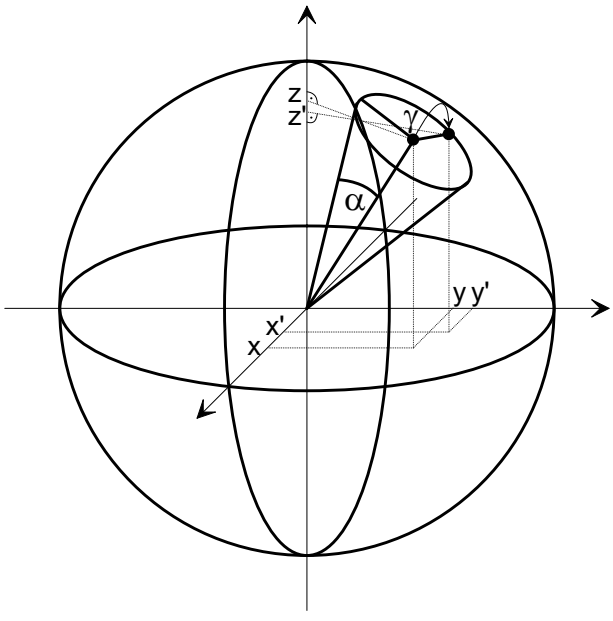

Figure A.1: Jump about an angle α in the direction γ.

coordinates is given by

$$\begin{pmatrix} x \\ y \\ z \end{pmatrix} = \sqrt{x^2+y^2+z^2} \begin{pmatrix} \sin\theta\cos\phi \\ \sin\theta\sin\phi \\ \cos\theta \end{pmatrix}. \tag{A.1}$$

Given a jump angle of, α, and an azimuthal angle, γ, new coordinates can be calculated using

$$u' = u\cos\alpha + \sqrt{1-u^2}\cdot\sin\alpha\cos\left(\gamma + \arccos\left(\frac{-x\cdot u}{\sqrt{1-u^2}\sqrt{1-x^2}}\right)\right), \tag{A.2}$$

where u denotes one of the three Cartesian coordinates x,y, or z.

A.2 Distribution of Relaxation Times

Nonexponential relaxation can be explained in the framework heterogeneous relaxation assuming an ensemble of relaxators relaxing *exponentially* with a distribution of time constants. Frequently, the Kohlrausch-Williams-Watts function (see Eq. 1.4) is used to fit nonexponential relaxation. The superposition of exponentials must be

$$\mathbf{e}^{-(t/\tau_{\mathrm{KWW}})^{\beta}} = \int_0^\infty \mathbf{e}^{-(t/\tau)}\rho_{\mathrm{KWW}}(\tau)\,\mathrm{d}\tau. \tag{A.3}$$

The distribution function, $\rho_{\mathrm{KWW}}(\tau)$, of relaxation rates can be obtained from inverse Laplace transformation. It is unfortunately not available in a closed analytical form except for cases of $\beta = \frac{1}{2}$.

Instead, a different distribution function frequently gets used: the log-Gauss distribution of the form

$$\rho_{\text{log-Gass}}(\tau) = \frac{1}{\sqrt{2\pi\sigma^2}}\mathbf{e}^{-\frac{(\log\tau-\log\tau_0)^2}{2\sigma^2}}. \tag{A.4}$$

For creating a log-Gauss distribution of relaxation rates, one creates a Gaussian distribution which serves as exponents for the relaxation rate. Calculating a Gaussian distribution from a uniform distribution, such as provided by standard random-number generators, relies on determining the inverse of the cumulative probability. While this is not

possible in a closed analytical form in one dimension, one makes use of the fact that in two dimensions this is easily done.

$$\int\int \mathbf{e}^{-(x^2+y^2)/2\sigma^2}\mathrm{d}x\mathrm{d}y = \int_0^R r\mathbf{e}^{-r^2/2\sigma^2}\mathrm{d}r = \sigma^2(1-\mathbf{e}^{-R^2/2\sigma^2}). \qquad \text{(A.5)}$$

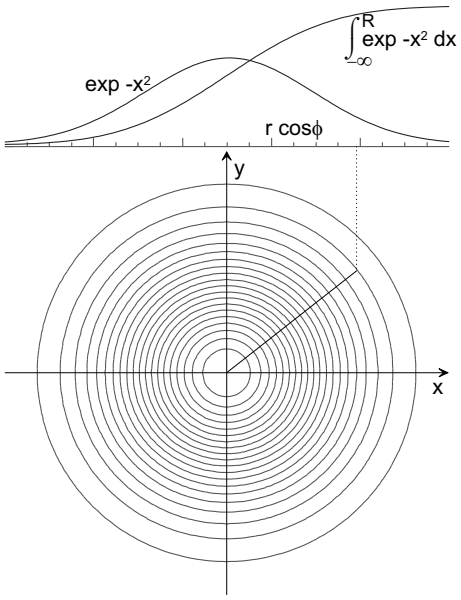

Figure A.2: Obtaining a random value that is Gauss distributed

Fig. A.2 visualises the process of obtaining random deviates with a normal (Gaussian) distribution after the Box-Muller [see Numerical Recipes by Press et al., 1992, Chap. 7]. By choosing two random numbers, $\phi = 0\ldots 2\pi$ and $x = 0\ldots 1$, one can obtain the variable t, that is distributed in a log-Gauss fashion

$$t = \sigma\sqrt{-2\log x}\cos\phi + t_0 \qquad \text{(A.6)}$$

around the centre value, t_0, with a logarithmic width, σ.

Appendix B

Synthesis of *o*-terphenyl

The synthesis of this substance was performed by H. Zimmermann, Max Planck Institute for Medical Research, Heidelberg, and proved extremely difficult. Since the procedure that finally lead to the desired *o*-terphenyl has not been published in its details in the literature, the sequence of steps and the reaction scheme (Fig. B.1) is provided here.

2[^{13}C]sodiumacetate (I) was prepared by carboxylation of the Grignard of ^{13}C-methyliode (Isotec Inc.) in ether at $-30°$C, followed by neutralisation with NaOH. 2[^{13}C]acetophenone (II) was obtained by acylation of benzene with (I) and $AlCl_3$ under reflux. After distillation, a chloromethylation with paraformaldehyde and conc. HCl was carried out at 90°C for 6 hours, resulting in 2[^{13}C]-3-chloropropiophenone (III). Substance (III) was then purified by column chromatography (silica, benzene). 2,3-diphenyl-1,3-butadiene (VI) was prepared in a conventional manner starting from diacetyl (IV) via 2,3-diphenyl-2,3-butanediol (V), followed by dehydration with $KHSO_4$ at 170°C. The diene was allowed to react with (III) and CH_3COOK in boiling xylene. After column chromatography (Silica, CH_2Cl_2/n-hexane, 8:2), a colourless oil was obtained which crystallised upon standing: 4[^{13}C]-1,2-diphenyl-4-benzoyl-cyclohexane (VII). Aromatisation of (VII) to 1[^{13}C]-1-benzoyl-3,4-diphenylbenzene (VIII) was accomplished using bromine in 80% yield in chloroform at ambient temperature (Silica, CH_2Cl_2/n-hexane, 7:3). Reflux of (VIII) in isopropylbenzene with sodiumamide (180°C, 2 hours) resulted in the desired ^{13}C-*o*-terphenyl, 1,1':2',1"-4'[^{13}C]terphenyl (IX). Substance (IX) was purified by chromatography (silica, CH_2Cl_2/n-hexane, 1:1) followed by distillation under

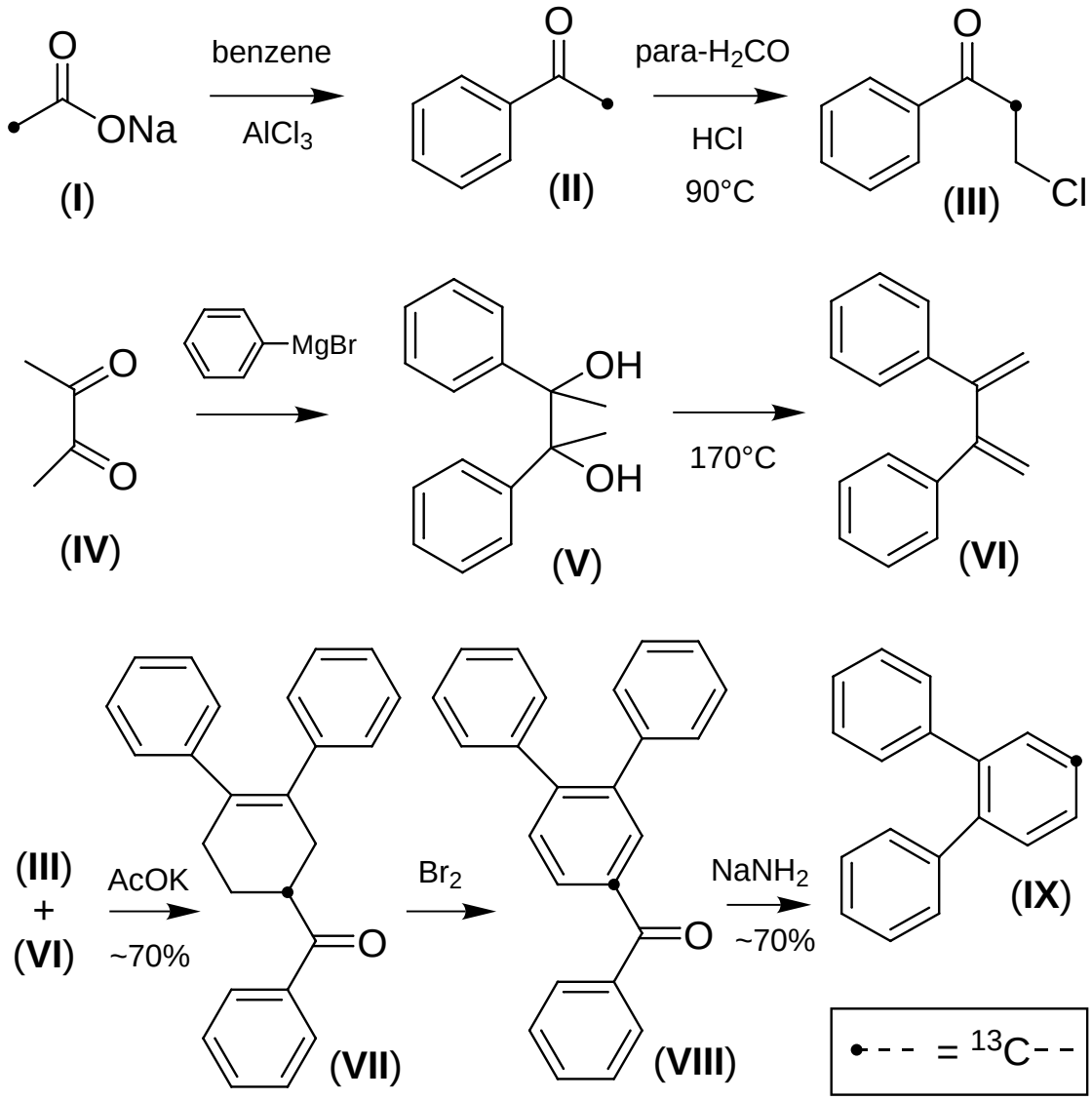

Figure B.1: Reaction Scheme for ^{13}C-labelled OTP

reduced pressure. The problem of spontaneous crystallisation was overcome by thoroughly cleaning the sample. The substance was dissolved in acetone and filtered with a hydrophobic, fluoropore membrane filter (PTFE, 0.2 μm pore size). The solvent was then removed under vacuum prior to glass sealing the sample. To avoid extensively long $T_1(^1\mathrm{H})$-relaxation times the relaxation agent Cr(acac)$_3$ was added at a low concentration of 0.06 wt.%. As previously checked for glycerol by means of a spatially selective 2D echo experiment, adding a relaxation agent at such a low concentration does not influence the dynamics [Reinsberg et al., 2001].

Index

Acknowledgement

- I would foremost like to thank my supervisor Hans Wolfgang for giving me the opportunity for working at the MPI, for his continued interest in the progress of my work, and for the freedom I enjoyed while working on my thesis.
- I am also indebted to Mark who invited me to work in his laboratory. Many fruitful discussions and exchanges of ideas, which decisively influenced my work, are greatly appreciated.
- My thanks are also extended to Andreas, who generously shared his expertise and knowledge.
- Burkhard's help made the computer experiments in Chapter 4 possible. Furthermore, he voluntary proof-read parts of this thesis. His benevolent advice immensely helped me professionally ("Und? Schon fertig?") as well as privately ("Beim Laufen, versuch' mal mehr mit den Beinen zu machen . . . ")
- I am thankful to Manfred, who was my first Mainz contact, who sent me to Wisconsin, and who proof-read part of the work.
- Ursula patiently introduced me to NMR of glass formers at the beginning of my thesis.
- Ulrich who shared his views on the world, some of his lunch, his passion for software that's free, and who stoically put up with my ignorance of chemical intricacies.
- I thank Robert and Ingo for their help in all matters of NMR and beyond,
- Daniel for the ab-initio calculations and the cappucini,
- Barbara – the good soul of the AK Spiess – who was continuously cheer- and helpful and always had a word of encouragement.
- I have been fortunate to depend on our 'Spectrometer Crew', Manfred and Hans-Peter, both of whose swift and professional actions at times of need allowed my experiments to smoothly continue. Beyond that, I could rely on their help with transformers and other weird projects of mine.
- The experimental work on OTP was possible due to Herbert who selectively and artfully labelled OTP at an impossible position.

- Thanks to our IT crew, namely Volker, Ulrich , Patrick, and Frank, computers and network were almost always working.

- I enjoyed the lively community of all the people from the Spiess group. I particularly thank: Michael for making office life more bearable, for his real-world touch scientists are supposedly lacking so often, for enlightening me about the superiority of a handball team in a little town called Lemgo ['lɛmgo:] and for "die schönsten Kleinodien Lemgoer Mundart"; Almut for the multifarious encouragements, for the bike rental, and for taking me out to the rocks even without any hope of rope-gun abilities on my part; Achim for offering his skills in repeatedly producing flashy pictures of chemical structures; Gillian for being such a proud Canadian, her help with English and her sweet Canadian goodies.

- I would like to thank my family. My parents' endless patience, understanding and unconditional support helped me throughout all of my studies. I thank Lisa for her moral support, for the time I was given to fully concentrate on this work, and for proof-reading a certainly less than captivating piece of prose.